QUANTIFICATION AND ANALYSIS OF THE GEOMETRIC PARAMETERS OF THE TOTAL CAVO PULMONARY CONNECTION USING A SKELETONIZATION APPROACH

A Thesis
Presented to
The Academic Faculty

By

Resmi KrishnankuttyRema

In Partial Fulfillment
Of the Requirements for the Degree
Master of Science in Bioengineering

Georgia Institute of Technology

December 2007

QUANTIFICATION AND ANALYSIS OF THE GEOMETRIC PARAMETERS OF THE TOTAL CAVO PULMONARY CONNECTION USING A SKELETONIZATION APPROACH

Approved by:

Ajit P. Yoganathan, PhD (Advisor)

Department of Biomedical Engineering

Georgia Institute of Technology and Emory

University

John Oshinski, PhD

Department of Biomedical Engineering

Georgia Institute of Technology and Emory

University

Shiva Sharma, MD

Pediatric Cardiology Services

Georgia

Date Approved: August 23, 2007

ACKNOWLEDGEMENTS

THANK YOU!!! THANK YOU!!! THANK YOU!!!

Though I will not be able to list out all the people who helped me and encouraged me in the past two years, I would like to mention few of them to whom I am deeply in debt.

First and foremost, thank God and my beloved guru Amma for being with me all the time.

I would like to thank my advisor, Dr. Ajit P. Yoganathan, for giving me an opportunity to work in this lab, for his support and guidance as I worked through the research for this Master Thesis. Without his help and advice, this thesis could not have been completed.

Also I would like to express my gratitude to Dr.Oshinski and Dr.Sharma for all their suggestions, comments and inputs in this research and for being on my thesis committee.

Special thanks to Dr. Lakshmi Prasad Dasi for being a mentor to me and helping me whenever I came across obstacles in research and also for his moral support. Thanks for answering to all my silly questions. I am forever indebted to you. Also special thanks to Diane for helping me with writing this thesis. Thanks for being so patient and

TABLE OF CONTENTS

LIST OF TABLES

LIST OF FIGURES

xv

SUMMARY

The Fontan repair for single ventricle congenital heart diseases is a three-stage palliative surgical procedure, ultimately resulting in the bypass of the right side of the heart. This is accomplished by routing the systemic venous return directly to the lungs. Although this procedure reduces the mortality rate, its long-term outcome is considered far from optimal. Hence, over the years lots of modifications have been suggested on the initial form of Fontan surgery proposed by Fontan in 1971 [Fontan, 1971]. Total Cavo-pulmonary connection (TCPC) is the current form of Fontan surgery commonly used these days.

Understanding the hemodynamics of the TCPC may lead to further optimization of the connection design and surgical planning, which in turn may lead to improved surgical outcome. Numerous experimental and numerical studies are focused on achieving this goal. How ever no studies have so far attempted to quantify the geometric characteristics of patient-specific TCPC anatomies and see how it correlates with their hemodynamic parameters.

This study develops a methodology to quantify the geometric characteristics of the complex TCPC anatomies using skeletonization approach. The centerline approximation of the TCPC geometry is used to extract geometric parameters like vessel area, curvature and offset. These parameters are used to quantify geometric characteristics of various TCPC templates that include extra-cardiac (EC) and intra-atrial (IA) TCPCs, TCPCs with bi-lateral SVCs and TCPC geometries before and after the Fontan surgery. Correlation between the geometric parameters and the TCPC hemodynamics, especially the power loss, are also analyzed in this study.

A semi automatic program has been developed to compute the geometric centerline using the method of iterative center of mass calculation. Using this program the skeleton of TCPC geometries can be computed irrespective of the number of participating vessels at the connection.

Since two types of TCPC anatomies, extra cardiac and intra atrial TCPCs, mainly dominate our database, these anatomies were analyzed in-depth. Comparison between these geometries showed that it is not the vessel cross-sectional area of the IVC baffle but the area variation across the vessel length is the significantly different parameter between the two groups. Also significant LPA narrowing was seen especially in patients with reconstructed aorta irrespective of their surgical preference.

Analysis of the TCPC geometric parameters with their power loss showed that, it is the vessel diameters of the outlet vessels, i.e. the pulmonary arteries, which significantly affect the TCPC efficiency. This analysis was observed using previously gathered experimental and CFD power loss data.

CHAPTER 1

INTRODUCTION

The incidence of single ventricle congenital heart problems in the USA is about 2 out of every 1000 live births [Statistics - www.americanheart.org]. In these cases, mixing of oxygenated and deoxygenated blood occurs in the heart causing severe cyanosis. The Fontan repair for single ventricle correction is a three stage repair; ultimately resulting in the bypass of the right side of the heart .This is accomplished by routing the systemic venous return directly to the lungs [Fontan, 1971].

Although this procedure reduces the mortality rate, its long-term outcome is considered far from optimal. Patients typically suffer from numerous long-term complications such as: ventricular dysfunction, protein losing enteropathy, arrhythmias and thromboembolism. To minimize these complications and improve long-term patient quality of life, it is necessary to improve the hemodynamic efficiency of this complex vascular connection, clinically known as the total cavo-pulmonary connection (TCPC) [de Leval, 1988]. Numerous studies have focused on optimizing the Fontan hemodynamics for over a decade. How ever none of them have attempted to quantify the geometric characteristics of patient-specific TCPC anatomies and see how it correlates with the hemodynamic parameters. . Many studies have shown that certain geometric characteristics of the TCPC and the associated vessels, mainly the pulmonary arteries (PA), play an important role in determining short-term and long-term patient outcomes [Hosein, 2007; Pekkan, 2005]. Factors such as PA stenosis degrade the flow efficiency and increase the risk factor for Fontan failure. Several i*n-vitro* studies have highlighted the importance of curvature of the inferior vena cava (IVC), its offset relative

1

to the superior vena cava (SVC), flaring of the VC anastomosis sites or enlarging the IVC anastomosis, in minimizing the energy dissipation at idealized TCPC junctions.

To our knowledge, despite the above-mentioned studies, no quantitative data exists that characterizes the complex TCPC geometries of patients and correlates their hemodynamic efficiency/inefficiency with geometrical parameters. Furthermore, no studies exist that correlate anatomic or hemodynamic characteristics of the TCPC to patient cardiac performance (cardiac index (CI) or ventricular power output). Setting power losses across the TCPC connection in perspective to cardiac performance would test the fundamental premise behind the Fontan optimization study, which is that the TCPC resistance is indeed clinically significant.

In this study, patient-specific Fontan anatomies are analyzed from both geometrical and hemodynamic stand points. Important geometric parameters are identified that differentiate: (1) the two main surgical protocols used to implement the TCPC, namely extra-cardiac (EC) and intra-atrial (IA) procedures; and (2) the two dominant pathologies of single ventricle heart defects, namely hypoplastic left heart syndrome (HLHS) and non-hypoplastic left heart syndrome (non-HLHS). Geometrical characteristics of bi-lateral SVCs, a subset of the TCPC anatomies with two superior venae cavae, are also quantified in this study. Lastly, the geometric features of TCPC models before and after the Fontan surgery are also analyzed.

This thesis is organized as follows: Chapter 2 reviews of all relevant studies previously published and provides all necessary background information; Chapter 3 outlines the overall hypothesis and specific aims of the present study; Chapter 4 details the methods developed to conduct this work; Chapter 5 presents the results with a quantitative geometric evaluation of 34 patient-specific Fontan anatomies (13 intra atrials, 13 extra cardiacs, 5 bi-lateral SVCs, and 3 pre Fontans); Chapter 6 discusses the differences between the various Fontan templates and relates these geometric findings

to the hemodynamic data. Finally, Chapters 7, 8 and 9 are conclusions, limitations and future work, respectively.

CHAPTER 2

BACKGROUND

Prior to going into the details of methods developed for this thesis, this chapter first familiarizes the reader with the issue we are trying to tackle by providing all necessary background information on the physiology of the heart as well as on the different technical methodologies that will come into play. For clarity, this chapter is divided into three sections: First, the physiology of normal and single ventricle hearts is explained, then, a review on the previous efforts to understand the geometric features of Fontan anatomies is provided. And finally, the different skeletonization approaches available in literature, which is the heart f this study is discussed.

2.1 The Cardiovascular System

The cardiovascular system is composed of heart and blood vessels. The blood vessels constitute a closed delivery system, which transports blood around the body, circulating substances such as oxygen, carbon dioxide, nutrients, hormones and waste products. There are three main types of blood vessels:

• Veins - the efferent blood vessels that return blood to the heart;

• Arteries - the afferent blood vessels that carry blood away from the heart;

• Capillaries - narrow, thin-walled blood vessels that form networks within the tissues and where all nutrient and waste exchanges take place.
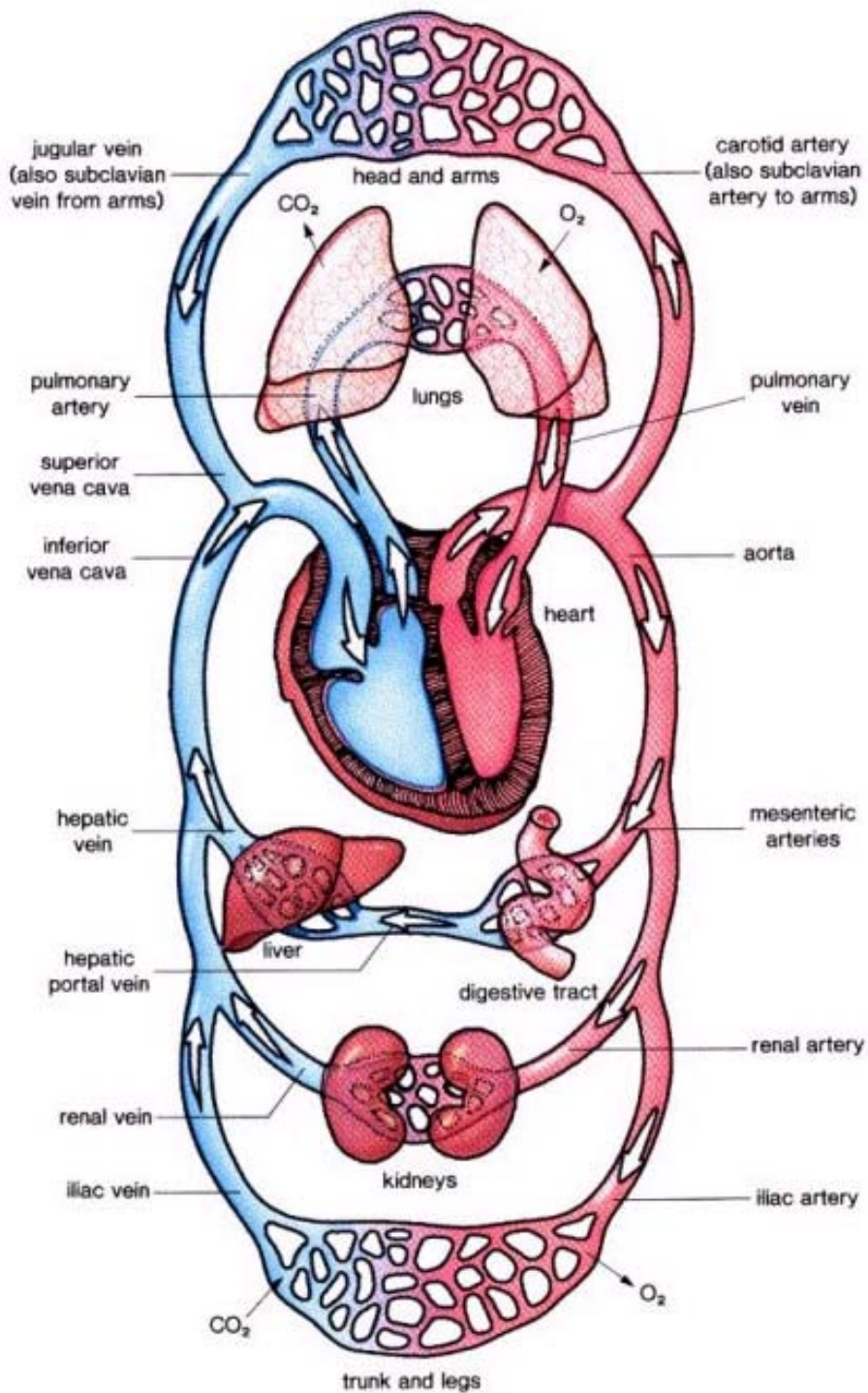
Figure 2.1: Schematic of the cardiovascular system of human body. The impure blood going into the heart is shown in blue and the pure blood returning from the heart is shown in red.

The principal function of the heart is to continuously pump blood around the

cardiovascular system. The cardiovascular circulation can be subdivided into two

primary circuits: the pulmonary and systemic circulations The pulmonary circuit describes the path going from the heart to the lungs and back, and the systemic circulation transports the blood between the heart and the remainder of the body. A picture of the cardiovascular system showing the blood vessels going from the heart to various parts of the body is shown in Figure 2.1

2.2 Normal Heart Physiology

The physiology of a normal heart is shown in Figure 2.2. Basically, the heart is composed of four chambers– the right and left atria and the right and left ventricles (Figure 2.2). A wall, called the septum, separates the right and left sides of the heart, which drive the blood through the pulmonary and systemic circuits, respectively. While it is convenient to describe the heart as two independent pumps (the left and the right), it is important to realize that they work in concert: both atria contract at the same time and both ventricles contract at the same time.

De-oxygenated blood from the body comes into the right atrium through the venae cavae. The superior vena cava (SVC), which drains blood from the upper extremities of the body and inferior vena cava (IVC), which drains blood from the lower extremities are the major blood vessels connected to the right atrium. During atrial contraction this blood is emptied from the right atrium into the right ventricle. The tricuspid valve, one of the two atrioventricular valves of the heart regulates this blood flow. During ventricular contraction, the blood is then pumped to the right and left lungs through the left and right pulmonary arteries (LPA and RPA, respectively) in order to be oxygenated. The pulmonary valve also known as the semi lunar valve, controls this part of the blood circulation. Oxygenated blood from the lungs flows back to the left atrium

6

through pulmonary veins. From there, the blood flows into the left ventricle and the atrioventricular valve that regulates the blood flow on this side of the heart chamber is the mitral valve (also known as bicuspid valve). From the left ventricle, the blood is pumped to the systemic circulation through the aorta. The valve between the left ventricle and the aorta is the aortic valve.
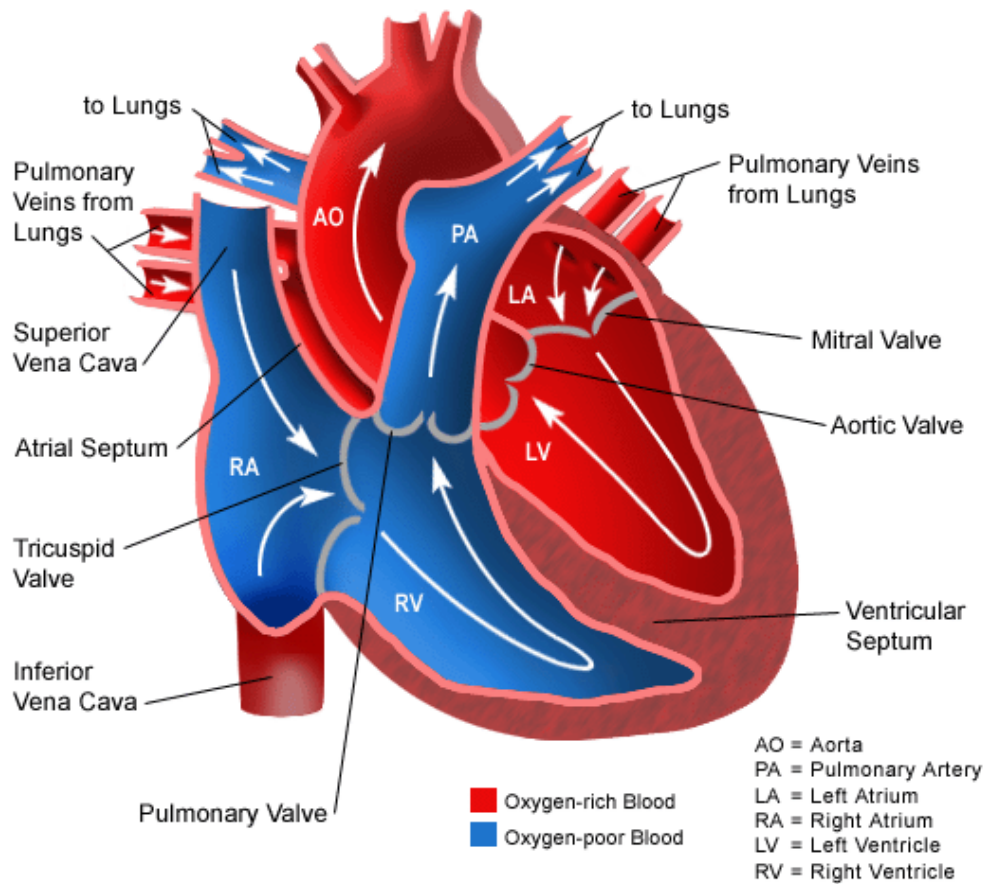
[www.daviddarling.info]

Figure 2.2: Schematic of a normal heart. White arrow indicates the direction of blood flow to and from the heart chambers .

2.3 Congenital Heart Defects

Congenital heart defect (CHD) describe heart defects that formed as the baby's heart was developing during pregnancy, before the baby is born. They are the leading cause of infant mortality in the western world accounting for about 20% of all infant death [Anderson, 2003; Rosano, 2000]. In US alone, one in every 100 babies is born with one or several CHDs [American Heart Association].

CHDs can be broadly classified into two categories. 1) Problems that cause too much blood to pass through the lungs. These defects allow oxygen-rich blood that should be traveling to the body to re-circulate through the lungs, causing increased pressure and stress in the lungs. 2) Problems that cause too little blood to pass through the lungs. These defects allow oxygen-poor blood to travel to the body. In the latter scenario, the body does not receive enough oxygen and the baby will be cyanotic, or have a blue coloring. In some cases there will be a combination of several heart defects, making the problem even more complex.

2.3.1 Single Ventricle Congenital Heart Defects

Single ventricle (SV) heart problems fall into the second category of the above mentioned CHDs. In these cases, there is only one functioning ventricle that supplies blood to both the systemic and pulmonary circulation and the oxygenated blood coming back from the lungs mixes with the deoxygenated blood coming back from the systemic circulation in that only effective chamber. As a result, the blood that redistributed to the body lacks oxygen causing acute cyanosis in the new-borns. The major differences between the cardiovascular circulation associated with normal hearts and single ventricle hearts is illustrated in Figure 2.3.
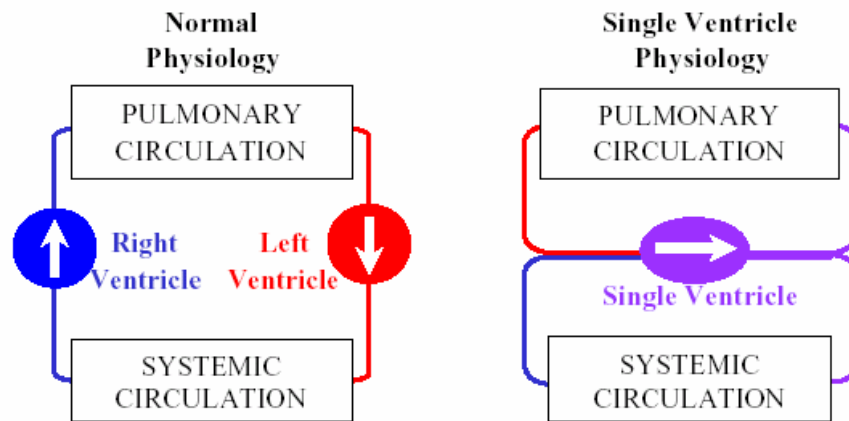
Figure 2.3: Schematic showing a normal and single ventricle heart physiology. In normal heart both ventricles work in parallel while there is a serial connection in single ventricle hearts.

The following sections (2.3.1.1 to 2.3.1.5) detail some of the most common pathologies that lead to a single ventricle heart anatomy:

2.3.1.1 Ventricular septal defect (VSD)

In this condition, there is a hole in the ventricular septum, which normally separates the right and left ventricles (Figure 2.4). Because of this opening, the higher pressure in the left ventricle pushes blood from the left ventricle into the right ventricle, thus retrieving blood from the systemic circulation and increasing the blood volume to be pumped by the right ventricle into the lungs. This condition results not only in poor oxygen saturation levels but also in increased right ventricular loading and potentially to congestion in the lungs.
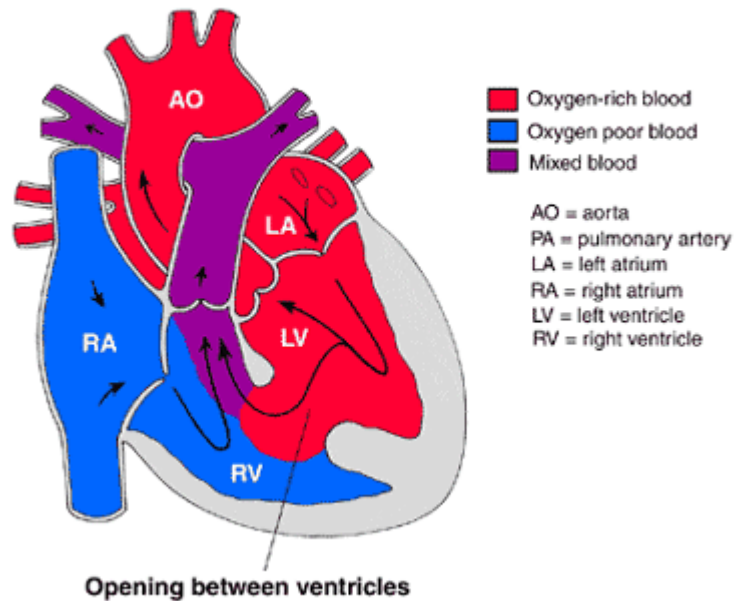
Figure 2.4: Ventricular Septal Defect (VSD). The opening is shown using the black line.

2.3.1.2 Tricuspid atresia

In tricuspid atresia, there is no tricuspid valve and hence no blood flows from the right atrium to the right ventricle (Figure 2.5). As a result, the right ventricle is small and under-developed. Survival depends on the presence of an opening in the wall between the atria (atrial septal defect) and/or the ventricles (ventricular septal defect). As a result, the venous blood that returns to the right atrium flows through the atrial septal defect into the left atrium. There, it mixes with the oxygen-rich blood coming from the lungs. Most of this mixed blood goes from the left ventricle into the aorta and to the body. The rest flows through the ventricular septal defect into the small right ventricle, and then through the pulmonary artery back to the lungs.

10

Figure 2.5: Tricuspid Atresia. The closed tricuspid valve, the atrial septal defect and associated under developed right ventricle is labeled in the figure.

2.3.1.3 Transposition of the great arteries

With this congenital heart defect, the positions of the pulmonary artery and the aorta are reversed, thus: a) the aorta originates from the right ventricle, so that most of the blood returning to the heart from the body is pumped back to the body without going through the lungs b) the pulmonary artery originates from the left ventricle, so that most of the blood returning to the heart from the lungs goes back to the lungs (Figure 2.6). Similar to tricuspid atresia, this defect is only viable when combined with other defects such as atrial septal defect or ventricular septal defect

Trans

Connecting blood vessel

AO

PA **LA**

Opening between atria

RA

LV

RV

Vessels switched

🟥	Oxygen-rich blood
🟦	Oxygen poor blood
🟪	Mixed blood

AO = aorta
PA = pulmonary artery
LA = left atrium
RA = right atrium
LV = left ventricle
RV = right ventricle
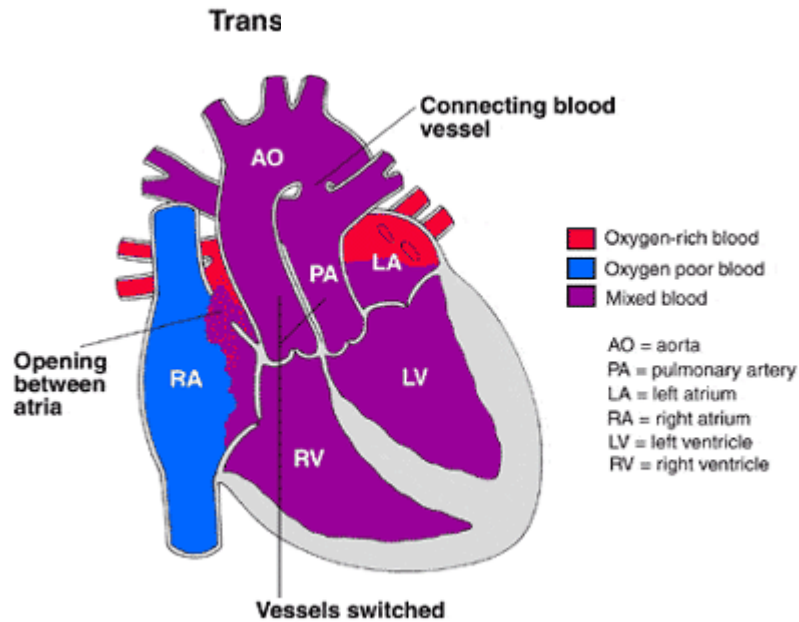
[www.childrens.com/cardiology]

Figure 2.6: Transposition of great arteries. The switched aorta (Ao) and pulmonary artery (PA) can be observed in the figure.

2.3.1.4 Tetralogy of Fallot

The tetralogy of Fallot (Figure 2.7) designates a combination of four congenital heart defects, namely:

- A ventricular septal defect (VSD), that allows blood to pass from the right ventricle to the left ventricle without going through the lungs

- A narrowing (stenosis) at or just beneath the pulmonary valve that partially blocks the flow of blood from the right side of the heart to the lungs

- A right ventricle that is more muscular than normal

- An aorta that lies directly over the ventricular septal defect

Figure 2.7: Tetralogy of Fallot (TOF or "Tet"). The VSD and obstruction of the right ventricle are labeled in the figure along with the aorta sitting above the VSD.

2.3.1.5 Hypoplastic left heart syndrome

In hypoplastic left heart syndrome, the left side of the heart is underdeveloped – including the aorta, aortic valve, left ventricle and mitral valve (Figure 2.8). Survival depends on the presence of two other concurrent defects: (1) an atrial septal defect (ASD), so that part of the blood returning from the lungs into the left atrium can be redirected to the right side of the heart, and (2) a patent ductus arteriosus (PDA), so that the blood pumped by the right ventricle into the pulmonary arteries may reach the aorta and from there perfuse the rest of the body

Very Small Aorta

Vessel Connecting Aorta and Pulmonary Artery

AO

PA

LA

Opening Between Atria

LV

Underdeveloped Left Ventricle

RA

RV

Oxygen-rich Blood
Oxygen-poor Blood
Mixed Blood

AO = Aorta
PA = Pulmonary Artery
LA = Left Atrium
RA = Right Atrium
LV = Left Ventricle
RV = Right Ventricle
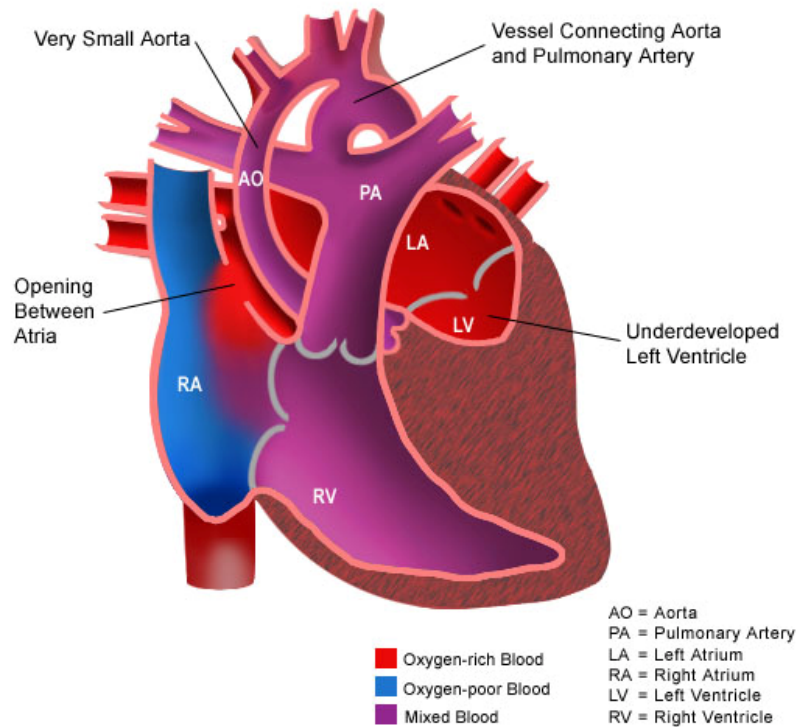
[www.childrenshospital.org]

Figure 2.8: Hypoplastic Left Heart Syndrome (HLHS). Note the hypoplastic left ventricle and the narrowed aorta. ASD connecting right and left atria and the PDA connecting the aorta and pulmonary artery are also marked in the figure.

2.4 Single Ventricle Correction Techniques

2.4.1 Evolution of Fontan Repairs

2.4.1.1 Historical Perspective

Until the middle of 20th century, children born with SV heart problems had no hope of survival unless they had any other coexisting defects such as a septal defect or a patent ductus arteriosus to link the systemic and pulmonary circulation. Heart surgery

was not even a choice in those days. During mid 1940's, by connecting pulmonary arteries (PA) and systemic arteries, a palliative correction procedure was developed [Blalock, 1945, Potts, 1946]. This started the beginning of a number of experimental procedures, which sought to develop better surgical solutions for single ventricle heart problems.

In 1949, Rodbarg and Wagner performed the first right ventricular bypass in dogs [Rodbard, 1949]. In 1958 Glenn reported the clinical success of a cavopulmonary shunt that connected the SVC and the RPA so as to try and augment the pulmonary blood flow [Glenn, 1958]. However, these shunts enabled only short-term survival. Patients had to suffer many complications like ventricular dysfunction, pulmonary vascular diseases, and thrombosis of the shunt, which in turn affected their long-term survival [Kyger, 1975].

2.4.1.2 The Fontan Repair

In 1971, Fontan and Baudet [Fontan, 1971] successfully implemented an atrio-pulmonary connection in a patient with tricuspid atresia, and the "Fontan" procedure or one of its many modifications became the major repair option in patients with single ventricle (SV) heart defect. The original Fontan procedure shown in Figure 2.9 comprised 5 main steps: (1) end-to-side anastomosis of the distal end of the RPA to the SVC; (2) end-to-end anastomosis of the right atrial appendage to the proximal end of the RPA by means of an aortic homograft; (3) closure of the atrial septal defect; (4) insertion of a pulmonary valve homograft into the IVC; and (5) ligation of the main pulmonary artery (MPA). After this procedure there was separation between the systemic and pulmonary circuits, which improved the arterial oxygen saturation.

However, placing a valve in the caval conduits resulted in many complications, including valvular stenosis and conduit failure [Shemin, 1979]. Also, the separation of the

IVC and SVC flows to only LPA and RPA respectively caused several complications when one of the pulmonary tracks became obstructed. Additionally, such a configuration directed the hepatic blood to flow only to the LPA, which was demonstrated to be strongly correlated with pulmonary venous malformation in SV patients [Justino, 2001; Pike, 2004; Srivastava, 1995].
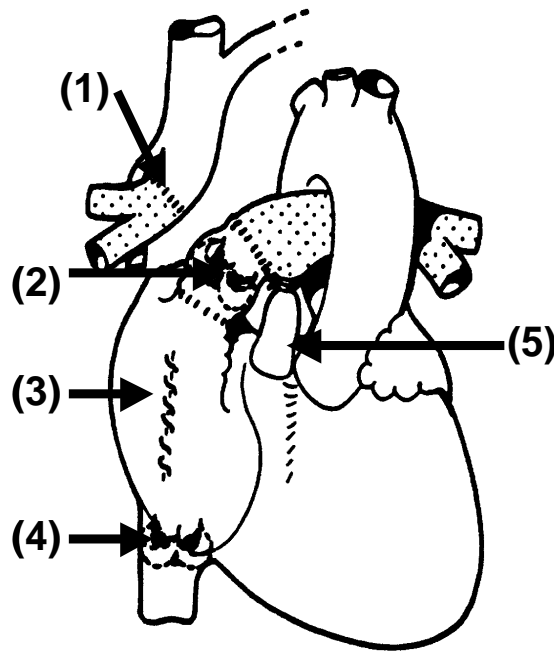
[Fontan and Baudet, 1971]

Figure 2.9: Schematic of the original Fontan repair for tricuspid atresia. The 5 steps in the surgical repair were marked using black arrows: (1) end-to-side anastomosis of the distal end of the RPA to the SVC; (2) end-to-end anastomosis of the right atrial appendage to the proximal end of the RPA by means of an aortic homograft; (3) closure of the atrial septal defect; (4) insertion of a pulmonary valve homograft into the IVC; and (5) ligation of the MPA.

Shortly after the first successful Fontan repair in 1971, Kreutzer et al. [Kreutzer, 1973] described a modified Fontan procedure without using a valve in the IVC. This was an atrio-pulmonary (AP) connection in which the right atrial appendage was sutured

directly to the pulmonary arteries (Figure 2.10). The tricuspid valve was also sutured to separate the pulmonary and systemic circulation. This procedure had the advantages of providing the pulsatile action of the atrium and redistributing the hepatic fluid to both lungs. Though the valve-less AP connection proved as a reliable technique patients had to suffer from complications like supra-ventricular arrhythmias, right atrial thrombus, exercise intolerance and other symptoms of low cardiac output [Dobell, 1986; Driscoll, 1992; Fontan, 1990; Mair, 1992]. These complications were usually related to a markedly dilated right atrium appendage, which was suspected to be due to the increased pressure load imposed on the atrium [Lardo, 1997].
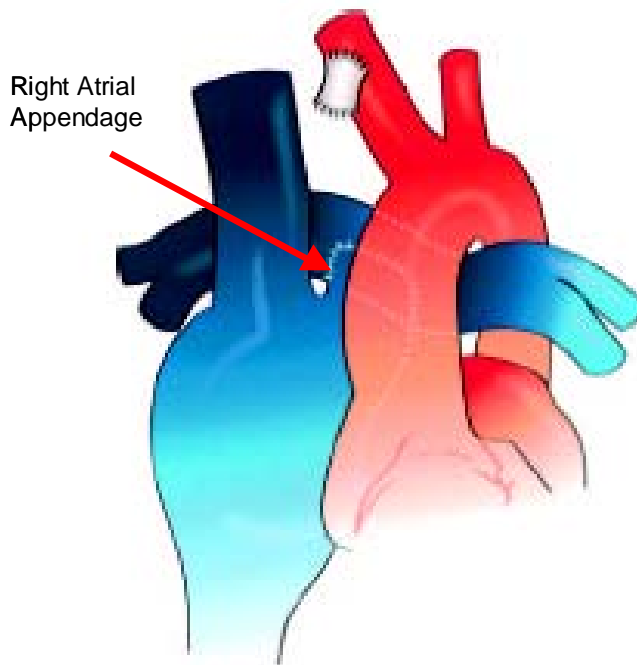
[Khairy, 2007]

Figure 2.10: Schematic of an atrio-pulmonary connection with the right atrial appendage shown using the red arrow.

2.4.1.3 The Total Cavo-pulmonary Connection (TCPC)

The atrio-pulmonary connection mentioned above was one of the many surgical improvements suggested for the classic Fontan operation. Though it was a commonly

used method, the benefits of the AP connection were questionable as the associated complications significantly affected the long-term outcome. In 1988, De Leval et al. proposed the total cavopulmonary connection (TCPC) as a logical alternative to the Fontan procedure [de Leval, 1988]. The TCPC was characterized as an anastomosis of the SVC directly (end-to-side) to the superior wall of the RPA, followed by creation of an intra-atrial channel through the right atrium to connect the IVC to the inferior wall of the RPA (Figure 2.13). De Leval hypothesized that such geometry would lead to more streamlined flow patterns with less turbulence and fluid energy loss. Several studies have showed that the TCPC is accompanied by a lower mortality rate, improved outcomes and a more favorable course during the postoperative period when compared to AP connection [Pearl, 1991; Podzolkov, 1997; Be'eri, 1998; Marcelletti, 2000].

2.4.2 Different Stages of Fontan

Fontan operation is usually performed in three stages during the earlier ages of childhood. This staging has significantly improved the success of the Fontan procedure. The objectives of the stage I procedure (Norwood), which is performed normally within the first 2 weeks of life, are to provide an unobstructed pulmonary venous return, a permanent systemic outflow from the right ventricle, and a temporary pulmonary blood supply to allow the pulmonary vasculature to develop and mature. The stage II procedureis usually performed by 6 months of age [Khairy, 2007] and consists of a bi-directional Glenn shunt or hemi-Fontan connection. Between around 18 months and 3 years of age [Khairy, 2007], the stage III procedure completes the total cavo-pulmonary connection of the inferior vena cava to the pulmonary artery.

18

2.4.2.1 Stage I: Norwood Procedure

The goals of the Norwood procedure [Norwood, 1993] are to allow the right ventricle to provide systemic circulation and to create a stable, balanced systemic and pulmonary circulation. The main pulmonary artery is opened and a homograft patch is placed in the area where the MPA branches into the RPA and LPA (Figure 2.11). In case of infants with a stenosed aorta, the narrowed aorta is opened, and a homograft patch is used to enlarge the aorta. The MPA is sutured to the aorta to allow the right ventricle to provide systemic circulation. A Blalock-Taussig shunt (BT shunt) is used to connect the right subclavian artery and the right pulmonary artery. At the completion of the stage I procedure the patient will have a mixture of oxygenated and de-oxygenated blood in the atria and right ventricle, providing blood both to the lungs (via the modified BT shunt|) and to the body (via the newly constructed aorta). During the next 6 months, the patient will grow out of the BT shunt and will be scheduled for the stage II surgery.

2.4.2.2 Stage II: Bi directional Glenn (Glenn) or Hemi-Fontan Procedure

Within a few months after the stage I, treated infants outgrow their shunts and become increasingly cyanotic. The second stage of the surgery, which consists of either a hemi-Fontan procedure [Norwood, 1993] or a bi-directional Glenn [Tanoue, 2001], is performed at this time. The principles in both are similar and involve an SVC to pulmonary artery anastomosis (Figure 2.12). The hemi-Fontan consists of an end-to-side anastomosis between the SVC and the RPA near the bifurcation. These results in blood flow from the SVC into both the pulmonary arteries. The cardiac end of the SVC is ligated. In the hemi-Fontan, both the cranial and cardiac ends of the SVC are sutured to the superior and inferior surfaces of the RPA.
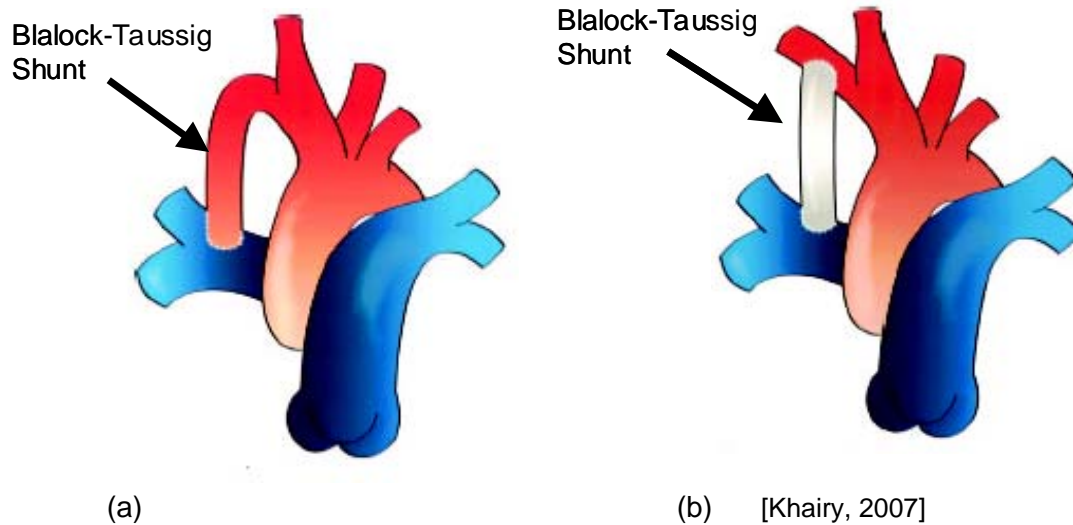
Figure 2.11: The Norwood Stage 1 procedure (a) The classic Blalock-Taussig shunt consists of an end-to-side anastomosis of the subclavian and pulmonary artery (b) The modified Blalock-Taussig shunt consists of an interposition tube graft that connects the subclavian artery to the ipsilateral pulmonary artery.

. The purpose of the second stage surgery is to begin the separation of the pulmonary and systemic circulation. Once the anastomosis is complete, the BT shunt can be removed. At the completion of the stage II, blood flows from the IVC into the right atrium and blood from the SVC flows into the pulmonary artery. As a result, there is a reduction of blood flow from the right atrium to the right ventricle.

SVC RPA anastomosis

BT shunt is removed
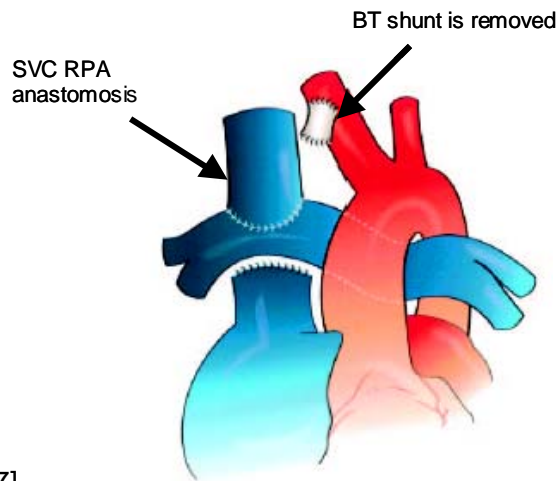
[Khairy, 2007]

Figure 2.12: The bi-directional Glenn procedure showing the SVC-RPA anastomosis. The modified BT shunt, shown in white, was taken down and over sewn

2.4.2.3 Stage III: Total Cavo-Pulmonary Connection (TCPC)

The third stage operation completes the separation of pulmonary and systemic circulation. The venous blood goes directly into the pulmonary arteries and then to the lungs. The oxygenated blood returns to the heart from the pulmonary veins and is pumped out to the body by the single right ventricle. The two widely used TCPC procedures are the lateral intra-atrial tunnel and the extra-cardiac conduit connection.

2.4.2.3.1   Intra atrial TCPC

De Leval *et al* [de leval, 1988] performed the first intra atrial TCPC operation in 1988. In that procedure, the right atrium is first connected to the RPA using the right atrial appendage. Then, a baffle of synthetic graft is placed inside the right atrium to

21

allow the systemic venous blood to flow along the right side of the baffle towards the pulmonary arteries without mixing with the pulmonary blood (Figure 2.13).

Baffle inside
right atrium
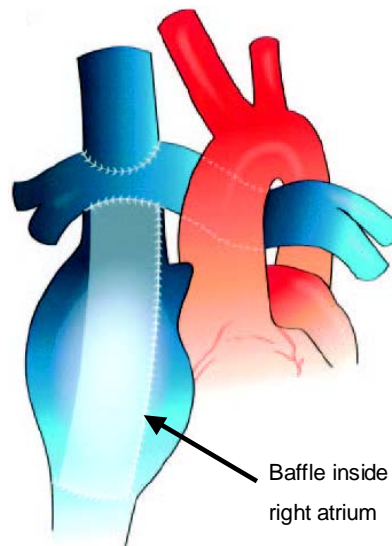
[Khairy, 2007]

Figure 2.13: Schematic of an intra atrial TCPC. The baffle connecting the IVC and pulmonary artery is marked using a black arrow.

2.4.2.3.2   Extra cardiac TCPC

Marcelleti [Marcelleti, 1990] and Laschinger et al [Laschinger, 1993] described the extra-cardiac conduit modification in the early 1990's. Here, rather than going through the right atrium, the systemic venous return from the IVC is routed around the heart (Figure 2.14). The IVC is disconnected from the right atrium and anastomosed to a synthetic graft. The other end of the graft is then sutured to the RPA.
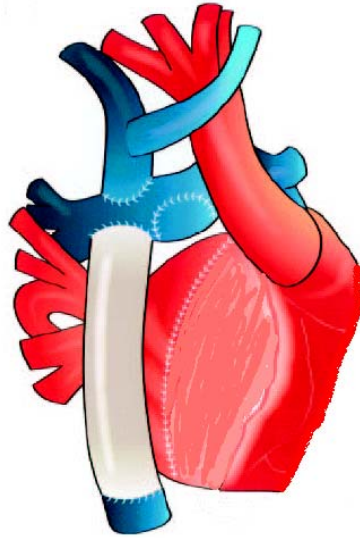
Figure 2.14: Schematic of an extra cardiac TCPC. The baffle connecting the IVC and pulmonary artery is shown as white colored conduit.

2.4.2.3.3   Choice of the TCPC Procedure

The choice of connection type at every stage seems to be dictated by surgeon preference. Numerous studies have focused on finding out which method is the optimum choice, mainly focusing on the 3rd and last stage of the procedure and leading to balanced pros and cons for both intra-atrial and extra-cardiac connections. The pumping action of the right atrium, which provides limited pulsatility to the IVC flow, is pointed as an advantage of the intra atrial option. However, this involves the risk of sinus-node damage and resulting arrhythmias. Extra-cardiac conduits, on the other hand, provide numerous advantages including smoother geometries, less atrial damage, and less or no time on the heart-lung machine. On the other hand they provide no growth potential and may lead to conduit stenosis and throboembolism [Haas, 2000; Petrossian, 1999; Tam, 1999]. Although long-term follow-ups are not yet available, early- and mid-term results for extra-cardiac conduits are favorable [Laschinger, 1996; Amodeo, 1997; Mavroudis, 1992; Quinones, 1997].

2.5 Previous Studies on TCPC

After the first Fontan surgery in 1971, numerous modifications have been suggested and implemented, aiming at improving long-term surgical outcomes and patients' quality of life. In addition to the major surgical suggestions discussed in the previous sections, which resulted in the current form of Fontan operation the TCPC procedure, studies have been going on to further improve the TCPC design with the hope of further minimizing post operative complications.

2.5.1 In vivo studies

Understanding the TCPC hemodynamics and geometrical features using in vivo modalities like echocardiography and MRI has become more and more common with the new innovations in medical industry. To name a few, Shiota *et al* reported the use of high-resolution echocardiography for studies the intra cardiac structures of CHD patients [Shiota, 1999]. In 1995 Fogel et al. [Fogel, 1996] performed a detailed study on SV patients after the Fontan operation using MRI tagging to understand the effect of this surgery on the myocardial functioning of the patients. They found significant differences in the myocardial strain of the patients between the three Fontan stages. In another study, Fogel *et al.* [Fogel, 1999] were able to characterize the contribution of each vena cava to each one of the pulmonary arteries in 10 Fontan patients with intra-atrial tunnels. In agreement with previous findings [Salim, 1995], they found that at an average age of 1.8$\pm$0.3 year-old most of the caval flow from the SVC, 60±6% went to the RPA, and 67±12% of the IVC blood went to the LPA. Be'eri *et al* [Be'eri 1998] used phase-contrast MRI to demonstrate the advantages of TCPC over an AP connection. Sharma *et al* [Sharma, 2001] analyzed the flow characteristics seen in intra atrial TCPC using MRI. They reported the flow structures within twelve different patients, 7 with an intra-atrial

lateral tunnel and 5 five with an extra-cardiac conduit. MRI velocity mapping combined with the use of adequate interpolation methods is capable of producing three-dimensional in vivo velocity data [Frakes, 2004], which can in turn be used to compute energy dissipation [Healy, 2001] or other parameters to characterize the efficiency of a given TCPC geometry.

2.5.2 In vitro studies

Since the first *in vitro* experiment done by de Leval *et al.* that demonstrated the superiority of the TCPC over AP connection [de Leval, 1988], researchers use *in vitro* studies to better understand the TCPC hemodynamics and come up with optimized TCPC designs. Sharma *et al.* [Sharma, 1996] studied the effects of varying caval offsets at various RPA/LPA flow ratios to determine the optimal combination for minimizing energy losses across the TCPC using glass models. They showed that offsetting the IVC and SVC by 1.0 or 1.5 caval diameters could significantly reduce the power dissipated across the connection. DeGroff *et al* [DeGroff, 2002] supported these findings by comparing the results obtained using two different sets of models with the typical vessel dimensions of 3-year old and 15- year-old patients, respectively. They demonstrated that the improvement in the efficiency produced by a caval offset decreased with larger vessels. More importantly they pointed out that the improvement brought in by a caval offset was not comparable to that of bigger vessels and thus questioned the trend of performing the Fontan on increasingly younger patients.

Caval offset decreases the fluid energy dissipation by avoiding direct collision of the caval flows. Another option is to curve the venae cavae and direct the caval flows such that they do not collide. Gerdes *et al* [Gerdes, 1999] demonstrated that this option leads to improved hemodynamics, but may impair caval blood mixing. Ensley *et al*

[Ensley, 1999] further demonstrated that curving the venae cavae was only optimal under specific flow conditions and instead recommended flaring the vessels towards the connection site. This method was shown to lower the power loss as well as allow for caval blood mixing. Using digital particle image velocimetry (DPIV) Grigioni *et al* [Grigioni, 2000] confirmed the observations made by Ensley *et al* [Ensley, 1999]. They identified a vortex at the confluence of the venae cavae and demonstrated its role in the regulation of pulmonary blood flow. Walker *et al* [Walker, 2001] proposed another modification suggesting that there will be poor hepatic fluid distribution in a zero offset flared model. They suggested that the optimal geometry would be the zero offset "cowl" geometry whereby an enlargement was made on one side of the IVC and of the SVC. As long as the cowl was directed toward the pulmonary artery of lowest flow rate, low power loss and relatively good distribution of hepatic flow could be obtained. De Zelicourt *et al* [De Zelicourt, 2005] created intra-atrial models reconstructed from patient MR images using transparent stereolithographic technique to look into the details of flow features of true anatomic configurations. They have reported complex, unsteady, and highly three-dimensional flow structures within the anatomic model, leading to high-pressure drops and power losses.

The latest among the series of optimum design for TCPC model is an optiflow model recommended by Soerensen *et al* [Soerensen, 2007]. This design featured a bifurcated vena cava, so as to lower the fluid mechanical power losses in the connection and to ensure proper hepatic blood perfusion to both lungs. They used rapid prototype modeling to investigate the flow patterns in the model, which were compared with those in the planar one-diameter offset TCPC with flared anastomosis sites.

2.5.3 Numerical simulations

Application of numerical simulations for the assessment of flow features in TCPC models has been popular in the Fontan research area for more than a decade now. Computational fluid dynamics (CFD) were used by de Leval *et al.* to investigate their intuition about the impact of caval diameter and IVC anastomosis size on the competition of IVC and SVC flows [de Leval, 1996] in intra-atrial model. This numerical study was the first of a series. The major advantages of CFD simulations include a full 3D representation of the flow field and a high degree of freedom regarding the geometry to be simulated. Knowledge of the whole flow field helps in the assessment of parameters such as flow distribution, pressure gradients and power losses that are otherwise more complex to quantify. Also the cost efficiency of the CFD simulations compared to the experimental set-ups attracts more people into this area.

Following the path of de Leval [de Leval, 1996], Migliavacca *et al* [Migliavacca, 1999] looked at the flow structures of extra-cardiac conduits. This design was shown to have superior hemodynamics [Hsia, 2004], which was in agreement with previous in vivo observations [Lardo, 1999]. Parametric studies have focused on the design of the IVC anastomosis site [Migliavacca, 2003]; the influence of varying caval flow ratios on dissipation, flow structures, and shear stress [Khunatorn, 2003], and the effect of pulmonary after-load [Guadagni, 2001]. The geometry of the TCPC has been modeled with increasing accuracy, from angular parametric models based on average anatomical measurements [de Leval, 1996] to realistic models directly reconstructed from patient MRI data [Guadagni, 2001; Ryu K, 2001; Migliavacca, 2003; Pekkan, 2004; De Zelicourt, 2006]. CFD also becomes an inevitable part in designing optimum TCPC geometries and surgical planning application. Soerensen *et al* [Soerensen, 2007] used CFD

modeling to compare the flow structures seen in their hemodynamically optimized TCPC configuration with other TCPC configurations.

For better understanding of the hemodynamics of complex physiological geometries such as Fontan, numerical simulation tools like CFD are becoming an essential part of the entire Bioengineering research area.

2.5.4 Summary of Fontan Geometrical Studies

Because the limited lung perfusion in the TCPC and increased central venous pressures impair the clinical outcome [Fontan, 1990], efforts have been made to evaluate optimized, surgically practicable TCPCs. In this context several modifications of the TCPC have been studied. As mentioned in section 2.5.2, the suggestion of adding an offset between the venae cavae [Sharma, 1996] received a lot of attention [DeGroff, 2002]. Including a curvature in the IVC and/or SVC at the TCPC junction was another popular suggestion [Gerdes, 1999; Ensley, 1999; Grigioni, 2000; Walker, 2001]. The latest among these studies is an optimized Fontan connection [Sorenson, 2007], which can provide good mixing of the hepatic blood and also can avoid the dissipative inflow collision.

In addition to the improvements suggested in TCPC design, certain studies pointed out that the geometrical parameters of the TCPC, especially the vessel dimensions also plays an important role in determining the overall efficiency of the TCPC [Hosein, 2007]. Among all the vessels that are part of the TCPC i.e, the IVC, SVC, LPA and RPA, it is the narrowing of the pulmonary arteries, which is commonly seen pre-operatively in Fontan patients, that is the major risk factor [Hosein, 2007]. Kerem *et al.* [Pekkan, 2005] conducted a CFD study on an LPA-stenosed TCPC model, in which they showed that the hydrodynamic power loss at the TCPC junction was significantly higher

in an LPA stenosed model compared to the same model after removing the stenosis. The power loss was increasing exponentially with the increase in LPA flow split. It has been reported by Morgan et al [Morgan, 1998] that a reduction in the pulmonary artery diameter causes a significant reduction in the pulmonary artery flow as well. This finding has been concreted by the latest studies published by Ordovas *et al.* [Ordovas, 2007], that showed an exponential relation between the ratios of the narrowest diameters of the right to left pulmonary arteries (RPA/LPA size) and right to left pulmonary arterial flow (RPA/LPA flow) in patients with pulmonary artery stenosis.

All these above mentioned studies points to the fact that the dimensions of the TCPC vessels may have a higher impact on the overall TCPC efficiency than other design parameters, but no strong conclusion has yet been established. Over the past decades, experimental and numerical models have incorporated increasing levels of geometrical complexity in an effort to more accurately model the in vivo conditions. However, these have failed to establish the general conclusions due to the complexity and number of the geometrical features that needs to be taken into account.There is now a need for systematic analysis methodology that will allow for the identification of crucial geometrical parameters (such as vessel diameter) and their correlation with the TCPC performances.

2.6 Centerline Approximations of 3D Geometries

Taking advantage of the techniques for 3D reconstruction of anatomies using MR images [Frakes, 2003], a method to obtain the geometrical parameters of TCPC models has been developed in this study. An approach of central line estimation of the 3D geometrical models has been used to achieve this goal. This technique of centerline approximation, generally known as skeletonization, is commonly used in shape analysis

applications in both computer and biomedical area. A description about the approach of centerline approximation has been detailed in this section.

2.6.1 The Skeletonization Technique – An Overview

Skeletonization is the method used to obtain the centerline representation of geometries, which provides information about the shape features of the geometry. In 1967 Blum [Blum, 1967] explained, a mathematical definition of the "skeleton" of a model. His definition was that, in the 3D Euclidean space (a plane that is defined using a set of points that can be defined in terms of angles and distance between the points is called a Euclidean plane), the skeleton or the centerline of geometry is the locus of the centers of all the maximal inscribed spheres.

There are several approaches to get centerline of geometry. A concept of boundary peeling is the frequently used technique for generating an approximation to the "true" Euclidean skeleton [Kong and Rosenfeld, 1989]. Also this is one of the intial approaches used to get geometry skeletons. In this technique border points of the object that satisfy certain topological and geometric constraints are deleted in iteration steps (figure 2.15). The entire process is repeated until only the "skeleton" of the geometry is left [Palagyi, 1998]. Different types of techniques have been developed over the time for skeletonization based on the efficiency of the process, ease of implementation and field of application of the technique. Some of these techniques are explained in detail in the section 2.5.2. The choice of a method depends on the application and also on the accuracy of the skeleton for the application. Combination of the two more techniques area also used depending on the application.

| (a) | (b) |
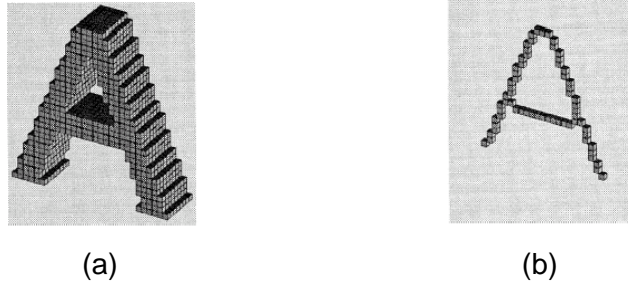
Figure 2.15: (a) A 3D picture containing the character "A" and (b) its central line obtained by the deletion of surface points are shown here. Each cube represents the surface points of the geometry that are deleted during the iterations.

2.6.3 Different approaches to the Skeletonization Technique

2.6.3.1 Iterative Thinning Algorithms

Among all the available algorithms for skeletonization, one of the first reported methods is the "Thinning Algorithm". This technique is based on the iterative deletion of geometric surfaces based on topological and geometric constraints. Rosenfield was first one to define a parallel thinning procedure (Rosenfield, 1975), in which different object elements in the object boundary are removed simultaneously. Later, in 1981 Morgenthaler [Morgenthaler, 1981] defined a deletion criterion for the thinning technique. His idea was to delete the "simple" or "deletable points" on the geometric surface and he defined a simple point as the point whose deletion does not change the topology of the geometry. Finally, Kong and Rosenfeld [Kong and Rosenfeld, 1989] put together a set of criteria that is now considered as the gold standard for topology preservations in the thinning algorithms.

Over the years a number of advancements have been suggested in parallel thinning algorithms, which improved the efficiency and processing time of the whole process [Palvidis, 1982; Hong 1995; Palagyi 1998]. The centerlines determined by this method are very centralized i.e., they avoid the walls of the geometry; however, the

31

determination of which points to be removed, known as simple point criteria, can be complex and computationally expensive [Paik, 1998].

2.6.3.2 Distance Mapping

Distance mapping, is a technique commonly used in robotics applications. Here a final point of the centerline is defined within the geometry and a distance to this goal point is computed for each point within the structure of interest [Kaufman, 1993; Lorensen, 1995]. The distance assigned is the shortest distance along a path to the goal point through the structure. Once the distance map is generated, a path from any starting point to final point can be determined by descending through the gradient of the distance map. An advantage of this technique is that it is computationally inexpensive [Paik, 1998]. For large structures, however, the distance map requires substantial computer memory. Additionally, the shortest distance approach has a tendency to produce paths that hug the wall of the organ rather than follow the central axis.

2.6.3.3 Iterative adjustment of the centerline

This technique divides the geometry into a number of frames. Then a starting frame is defined first and subsequent frames are determined based on the 2D center of mass calculation in the plane perpendicular to the center obtained at the previous point. This method is one of the simplest skeletonization techniques. Though this technique tends to keep the path centralized, since the center of mass in a 2D slice may not lie along the central axis of the 3D structure the centerline approximation may not be accurate all the time. Additionally, this method does not guarantee that the path will stay within the structure of the geometry.

In this study, we are using a modified form of this iterative approach. Here the accuracy of the centerline computed using the initial frames are substantially improved by further iterations, in which the frames are defined in directions perpendicular to the axis of the geometry. By doing so, all the disadvantages of the iterative method mentioned in the above paragraph will be corrected.

2.6.3.4 Harmonic Skeletonization

Yang and Zhu [Yang, 2005; Zhu, 2005] defined a different approach for skeletonization, in which they used the solution of a harmonic equation on the tubular geometric surface to evaluate the centerline. They called it a "harmonic skeleton." Solution of a Laplace equation defined based on the surface temperature distribution of the geometry is obtained by providing appropriate boundary conditions. This solution is then used to extract the centerline of the geometry. This technique guarantees smoothness and connectivity of the central line.

2.6.4 Applications of skeletonization in Bio Engineering

Even though the skeletonization technique was commonly used in computer animations and robotics for a long time, it started to get a lot of interest in the bio engineering area from the beginning of 1990 onwards. Some of the areas that use the skeletonization of geometries in large extent include endoscopy (mainly for the path planning applications in virtual endoscopy), stenosis evaluation of the tracheal tree, and modeling of the blood vessels.

It was for the development of virtual endoscopy that the skeletonization was first used in bio engineering area. The idea of virtual endoscopy was first published by Vining

et al [Vining, 1996], in which the organ of interest was reconstructed using CT images and these images were then used for non-invasive screening of the tubular structured organs like bronchial trees and colon in the body. Soon this concept became a popular screening technique because of its low cost and non-invasive approach. Also this method requires fewer user interactions and less computation time compared to the invasive screening techniques.

In order to guide the virtual camera through the lumen of the organ, it is necessary to define a centerline of the geometry. The boundary thinning method was the commonly used approach. Later, Paik et al [Paik, 1998] developed a modified thinning algorithm for virtual endoscopic application. They have used a combination of the thinning algorithm and the distance mapping method, which reduced the computation time substantially.

Later, Wang et al [Wang, 1999] used the modified thinning algorithm for another application, where they used this technique for modeling and segmentation of blood vessels. To develop a 1D model for the finite element modeling applications in cardiovascular area, Steele et al [Steele, 2003] also used the same algorithm of skeletonization. Yushkevich et al [Yushkevich, 2006] proposed a similar application of skeletonization called *inverse skeletonization*, where the skeleton of an object is defined first and the object's boundary is derived analytically from the skeleton. They suggest that is method is provides the boundaries of three-dimensional objects as continuous parametric manifolds, while maintaining the proper geometric relationship between these manifolds.

Another rapidly growing application of skeletonization techniques is the modeling of blood vessels and the evaluation of stenosis in blood vessels. Yang et al [Yang, 2005] used harmonic skeletonization for quantifying coronary artery stenosis. They showed that their method could quantify the stenosis of the coronary arteries quickly and

34

accurately. Another application for this harmonic skeletonization was proposed by Zhu et al [Zhu, 2005], in which they used this approach to obtain the flattened visualization of branched physiological structures like blood vessels. This method could also be used for accurate modeling of the vascular structure.

A different approach of skeletonization for modeling of the bifurcating vessels uses centroid estimation of the inscribed spheres of the blood vessel model, proposed by Antiga et al [Antiga, 2004]. They use this automatic technique for the objective comparison of distributions of geometric and hemodynamic quantities over the surface of bifurcating vessels. Kiesler et al [Kiesler, 2006] reported successful implementation of the thinning algorithm for quantifying the laryngo-tracheal stenosis in the larynx as another application of the skeletonization method.

2.6.5 Summary

Because of the tubular structure of the participating vessels, the method of skeletonization can be easily applied to the TCPC geometry to calculate the parameters associated with this anatomy. In this study, we have used the method of Iterative adjustment of the centerline for obtaining the TCPC skeleton. The simplicity of the algorithm was the main attraction. The disadvantageous associated with the approach was overcome using an additional iterative procedure which approximates the centerline towards the "true" skeleton after each iteration.

Following chapters of this thesis will give a detailed idea about the method development and its application in characterizing TCPC geometries.

CHAPTER 3

HYPOTHESIS AND SPECIFIC AIMS

As described in the previous chapter, previous studies have shown that certain geometric characteristics of the TCPC and the associated vessels, mainly the pulmonary arteries (PA), play an important role in determining short-term and long-term patient outcomes. Factors such as PA stenosis degrade flow efficiency and increase the risk factor for Fontan failure [Hosein, 2007; Pekkan, 2005]. *In-vitro* studies have highlighted the importance of curvature of the inferior vena cava (IVC) and its offset relative to the superior vena cava (SVC) in minimizing the energy dissipation at idealized TCPC junctions. Despite these studies, no quantitative data exists that characterizes the complex TCPC geometries of patients and correlate their hemodynamic efficiency/inefficiency with geometrical parameters. The lack of quantitative geometric characterization of these complex vascular anatomies hinders the analysis necessary to correlate the overall hemodynamic performance of the TCPC with certain surgical techniques and/or anatomical features. Such correlation would help design future surgeries so as to minimize power losses and, in doing so, improve long-term patient quality of life.

3.1 Hypothesis

The guiding hypothesis of this study is that:

The geometric characteristics of TCPC anatomies differ significantly and may be correlated with the different levels of hemodynamic efficiency.

Following are three specific aims of this study designed to test the hypothesis:

3.2 Specific Aim 1

Develop a methodology to obtain geometric characteristics of the TCPC.

In order to obtain the geometrical parameters associated with the TCPC anatomies, a centerline approximation of the 3D representation of the models named as the "skeletonization" approach will be used. Developing a technique for this purpose is a critical step that will then allow us to compute critical geometric parameters such as, vessel dimensions, caval offset and vessel curvature.

3.3 Specific Aim 2

- Use the above developed skeletalization approach to compute the geometric parameters associated with different TCPC anatomies and:
    - o Compare extra cardiac and intra atrial geometries
        - ▪ Impact on HLHS vs. Non HLHS patients
    - o Compare pre and post Fontan geometries
    - o Analyze bi-lateral SVC geometries

3.4 Specific Aim 3

- Correlate the TCPC geometric parameters with hemodynamic efficiency.

In this specific aim, the correlation between the computed geometric parameters and the hemodynamic efficiency of the TCPC geometries will be analyzed. Power loss, a commonly accepted measure of the overall efficiency of a given TCPC design will be used as the hemodynamic efficiency parameter in this study. Experimental power loss measurements across six different TCPC geometries obtained from previous *in vitro* experimental studies and CFD power loss measurements for nine TCPC geometries will be used for this purpose. In addition, these power losses will be contrasted to the ventricular power output calculated from *in vivo* PCMRI for each one of these fifteen patients.

CHAPTER 4

MATERIALS AND METHODS

4.1 Overview

The first six sections of this Chapter (4.2 through 4.6) detail the methodology developed to break down patient-specific Fontan anatomies into a series of quantifiable parameters. This is accomplished by skeletonizing the geometry and obtaining a centerline representation of the 3D geometry [Paik, 1998]. These data reduction steps allow for the easy extraction and quantification of geometrical characteristics, such as vessel cross sectional area, area variation across the vessel length, vessel curvature, caval offset etc. These parameters can also be used to find out if there is any correlation between the anatomic and hemodynamic data of the TCPC. The details of the study patient population are described in section 4.7 followed by the statistical analysis criteria in 4.8.
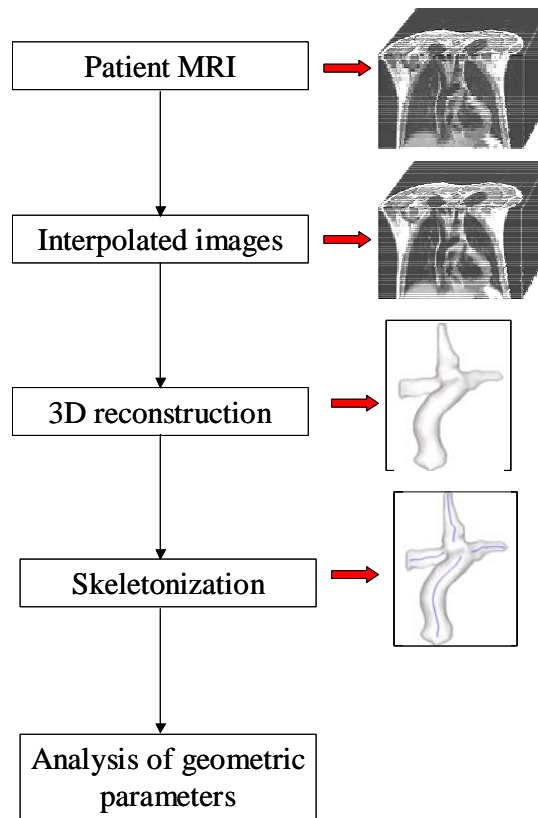
Figure 4.1: Flow chart representation of the overall procedure of TCPC geometric characterization starting with the patient MR Images.

4.2 Reconstruction of Patient-Specific 3D Anatomic Models

The methodology followed in our laboratory to generate patient specific 3D anatomical models from raw anatomic magnetic resonance (MR) images use a semi-automated in-house code [Frakes, 2003] and commercial software Mimics (Materialise Inc. Ann Arbor, MI). A stack of MR images of the thoracic region of the patient is acquired as the first step.

The MRI scanning protocol to obtain the stack of anatomic images is as follows. A steady state free precession (SSFP) sequence is used to obtain axial slices of 3-5 mm in thickness with approximately 1 x 1 mm in-plane resolution. This is achieved with a 256 x 256 matrix size and a 27 cm x 27 cm field of view. Patients are recruited for MRI

examination at the Children's Healthcare of Atlanta (CHOA), the Children's Hospital of Philadelphia (CHOP), and the University of North Carolina (UNC).

Data from CHOA are acquired on a Signa (General Electric Healthcare, Chalfont St. Giles, United Kingdom) 1.5 Tesla scanner, where a repetition time (TR) of 5-8 ms and an echo time (TE) of 1.5-3 ms are used. At CHOP, a Sonata or an Avanto (Siemens Medical Solutions, Erlangen, Germany) 1.5 Tesla scanner is used with a TR of 150-250 ms and a TE of 1.1-1.5 ms. Signals are averaged over two acquisitions and 25-45 slices are acquired, depending on the size of the patient. Magnetic resonance (MR) angiographic methods are not employed because younger patients are not systematically administered gadolinium contrast.

The pixel sizes of these images are typically anisotropic, with the through plane resolution being higher than the in plane resolution. Isotropic voxel sizes are obtained using an adaptive control grid interpolation technique, a method based on a hybrid technique of optical flow and block matching as described by Frakes et al [Frakes, 2003]. The vessels of interest, the superior vena cava (SVC), inferior vena cava (IVC), left pulmonary artery (LPA), and right pulmonary artery (RPA), are then segmented out from the interpolated stack of anatomic MR images using a previously developed inhouse semi-automatic methodology [Frakes, 2003]. Each image is thresholded by intensity and spherical element of voxels is randomly moved throughout a selected region for several iterations to segment the vasculature. Raw, thresholded, and segmented sample vessels in one axial slice are shown in Figure 4.2. Segmented results are saved as binary images, containing only pixels that define the vessels of interest.

The final step is to reconstruct the segmented vessel cross-section into a 3D representation of the TCPC blood-volume using the commercial software Mimics

41

(Materialise Inc. Ann Arbor, MI). This is a reverse engineering tool designed to interface between MR imaging and computer aided design (CAD), rapid prototyping, or finite element analysis.
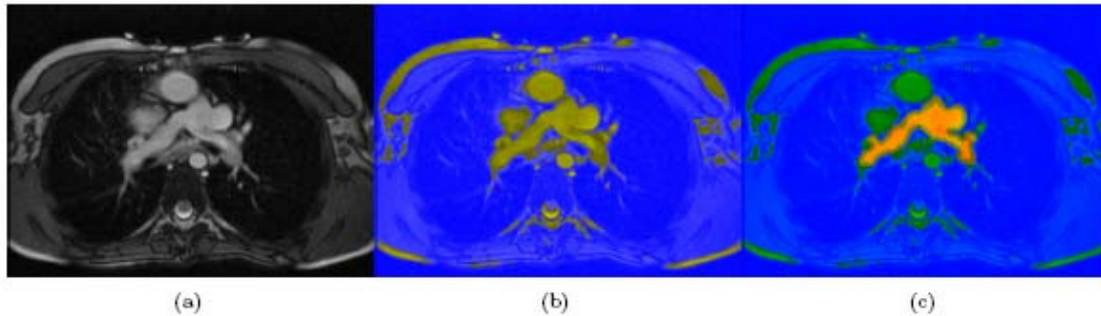
Figure 4.2: (a) Raw, (b) thresholded, and (c) segmented images of the pulmonary arteries shown from the axial perspective.

4.3 Skeletonization Method

4.3.1 Overview

To characterize the complex 3D geometries of the TCPCs, a skeletonization approach, which is commonly used for shape analysis applications, is employed. A modification of the commonly used skeletonization technique, iterative adjustment of the centerline method [Paik, 1998], is used in this study. The basic principle of this method is to "slice" the geometry of interest into a series of frames and then define the geometric centerline as the line that connects the center of mass of each frame.

As explained in section 4.2, 3D TCPC anatomies are reconstructed from patient MR images. These 3D reconstructions are represented as triangulated 3D surface geometries, from which a skeletalized representation will be obtained by reducing the geometry to its centerline approximation.

4.3.2 Geometry "Slicing" and Centroid Calculation

The first step of the skeletonization process is to "slice" the geometry so as to represent it as a series of cross-sections rather than a full 3D surface. Thus, the 3D TCPC surface is sliced at ~1 mm spacing along the direction of vessel length. These initial geometry slicing performed on a TCPC vessel can be seen in the flowchart representation of skeletonization shown in Figure 4.3. A macro written for the software Tecplot (Tecplot Inc., Bellevue, WA) is used to create the initial slices and this macro is provided in Appendix C.

The slice centroids, for building the geometric centerline, are then computed from these initial slices as follows. (1) A point that is approximately at the center of the slice is selected as shown in Figure 4.4 a. (2) Each slice cross sectional area is divided into triangles using the approximate center as the common vertex for all triangles. The triangulation starts from a point on the slice that is closest (shortest distance) to the slice center. The program then finds the next point on the slice that is closest to the initial one and forms a triangle. This process goes on until it comes back to the starting point. A schematic of this process is shown in Figure 4.4 b. (3) The area and centroid of each triangle is computed using the following basic geometric equations: let ABC be a triangle and *a*, *b* and *c* the distances BC,AC and AB, respectively (Figure 4.4 c).

Then, the area of the triangle ABC can be written as follows:

$$A = \sqrt{(s \times (s-a) \times (s-b) \times (s-c)} \quad \textbf{(4.1)}$$

where s = (a+b+c)/2; half the perimeter of the triangle.

INPUT:
3D Reconstructed
Anatomical Model

3D reconstructed model

Slice the model into ~ 1mm slices

Initial slicing

Calculate the slice centroid and initial centerline

Triangulate each slice with a common vertex at slice center

Calculate area and centroid of each triangle

Slice Center $= \dfrac{\sum(area \times centroid)}{\sum(area)}$

Re-slice the geometry perpendicular to the initial centerline

Final Slicing

Repeat iteration until two centerlines are the same

Centroid convergence after the second and third iterations are shown in pink and green colors

OUTPUT:
Obtain the centerline of the geometry

Geometry with centerline

Figure 4.3: Flow chart representation of the skeletonization procedure. Starting with the 3D reconstructed anatomical model, the flow chart shows pictures of initial and final slicing directions, converged centerlines and the final skeleton of the geometry

The centroid of the triangle ABC is given by

$$\left(\frac{1}{3}(x_a + x_b + x_c), \frac{1}{3}(y_a + y_b + y_c)\right) = \frac{1}{3}(x_a, y_a) + \frac{1}{3}(x_b, y_b) + \frac{1}{3}(x_c, y_c).$$

(4.2)

where, x_i and y_i are the triangle vertices.
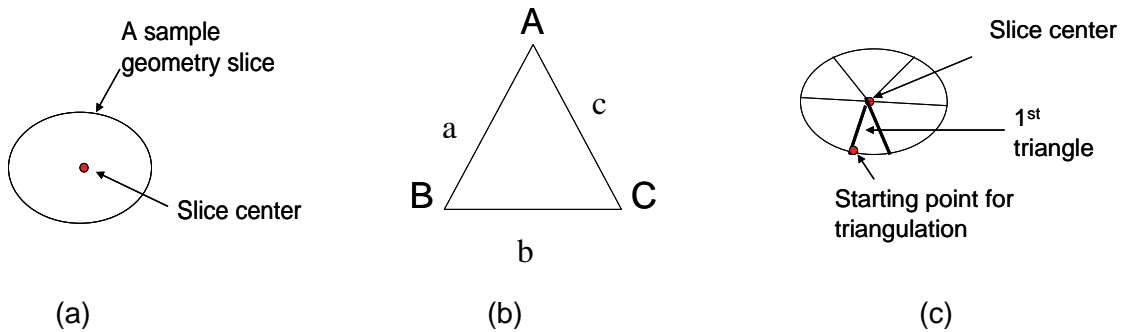
Figure 4.4: Schematic showing the centroid calculation of geometry slices (a) a sample geometry slice is shown along with the slice center (b) this sample slice is then divided into triangles with the slice center as their common vertex. The triangulation starts from the point that is of shortest distance from the slice center and completes a triangle using its immediate neighbor (c) one triangle from this slice is zoomed in to shown the triangle sides and vertices.

Once the area and centroid of the triangles have been computed, the center of each vessel cross-section can be obtained by the equation:

$$Slice\ Centroid = \frac{\sum (Area \times Centroid)}{\sum Area}$$

(4.3)

The vessel centerline is then built by connecting the centers of adjacent vessel cross-sections or slices.

4.3.3 Iteration Procedure

The accuracy with which the centerline is captured after the first iteration is highly dependent upon the initial slicing direction and the orientation of the slices. Figure 4.3 shows the flow chart representation of the skeletonization procedure and the differences

45

between the initial and final slicing directions. If the vessel slicing is not truly perpendicular to the centerline, the estimated skeleton will not be accurate. An iterative procedure is thus defined to correct simultaneously both the slicing direction and associated centerline (see figure 4.3). The iterative centerline refinement proceeds as follows: An initial guess is first made and the associated centerline S^0 is computed. Then, in each subsequent iteration N, the 3D vessel geometry is re-sliced in a direction perpendicular to the tangent of the centerline curve S^{N-1} computed in the previous iteration (i.e, in the N-1th iteration). The centroids are recomputed for the new set of slices and the curve through the newly computed centroids provides a better estimate S^N of the true centerline, S^0. The process is repeated until centerlines S^{N-1} and S^N from two consecutive iterations converge. An in- house code developed using 'C' language (Microsoft Visual studio 6.0, Microsoft Corporation) is used to perform the slice centroid computation and the skeletonization   process. A protocol for the entire skeletonization process is provided in Appendix A.

4.3.4 Application to the TCPC

In this study all four vessels of the TCPC – IVC, SVC, LPA and RPA were skeletonized separately so that the geometric characteristics of each vessel could be compared independently. The landmarks used to define the beginning and end of each of the four vessels are as follows: the region of confluence of the four vessels on one end, and the region of bifurcation on the other end (figure 4.5).

The first slicing direction is chosen to be in the left-right direction for the pulmonary arteries (LPA and RPA) and the superior-inferior direction for the inferior and superior venae cavae (IVC and SVC). This eases the skeletonization process. Using this

method, the centroid curve was found to converge to the true vessel centerline within four iterations.
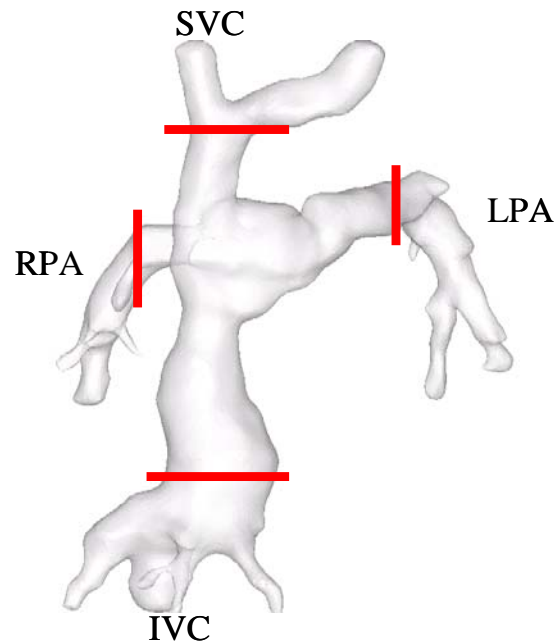
Figure 4.5: 3D reconstructed TCPC anatomy marked with the points of vessel bifurcation. The red line indicates the markings.

4.4 Validation

In order to validate the skeletonization method, the procedure explained in section 4.3 was applied to an idealized TCPC model, whose vessel dimensions are known *a-priori*. The geometry retained for this purpose was the zero-offset TCPC model. In order to assess the sensitivity of the developed approach to the initial slicing direction, the model was run twice through the skeletonization process. First, vessel axes were aligned with the coordinate axis (Figure 4.6a), so that the original slicing was actually performed normal to the vessel axis. In this orientation, it is expected to get slices normal to the vessel axes after the first iteration itself. Then, the model was rotated at

47

an angle (30^0) with respect to its original co-ordinates (Figure 4.6b), so that the initial slicing resulted in oblique slices of the model. Here also, all the four vessels of the TCPC are skeletalized separately for the ease of comparison.

(a)   (b)
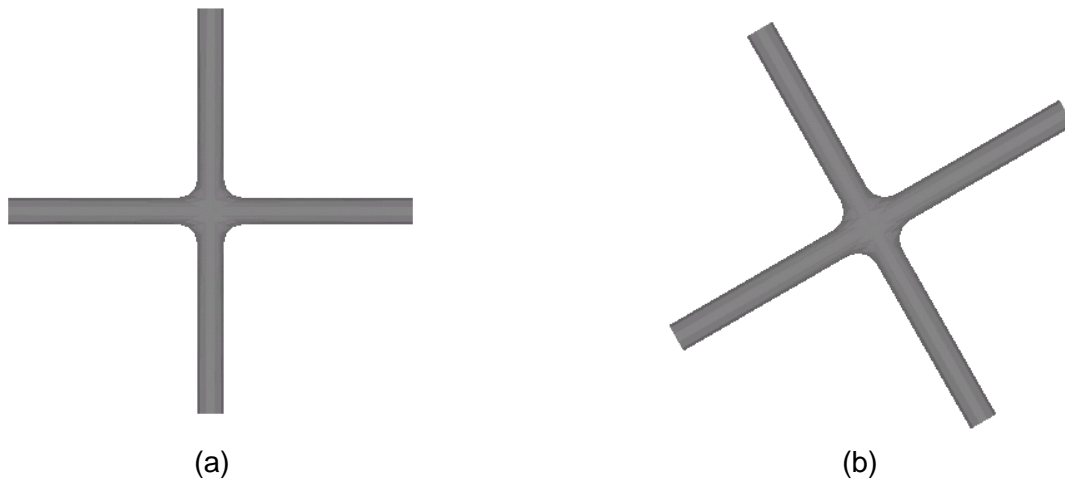
Figure 4.6:   Idealized zero offset TCPC model used for the validation studies with (a) vessel axes aligned to the coordinate axes (b) model rotated by 30^0 with respect to the original co-ordinate axes.

4.5 Computation of Geometric Characteristics

4.5.1 Overview

Once the skeletalized representation of the TCPC is obtained, geometric parameters such as vessel area, vessel orientation, vessel curvature and offset are computed using these data.

4.5.2 Vessel Area

The final iteration of the skeletonization provides the cross-sectional area along each vessel centerline at ~1mm intervals. Since different TCPC templates (intra atrial, extra cardiac, bi-lateral SVC and pre Fontan) are analyzed in this study, in order to quantify their vessel cross-sectional area, mean cross-sectional area across the vessel length and its standard deviation are computed. Narrowing of the vessel dimensions are quantified using minimum vessel cross-sectional area. For comparison purposes maximum cross-sectional area was also computed. The procedures used to compute each of these parameters are listed below.

Mean vessel area and standard deviation: The cross-sectional areas computed along the entire length of a vessel centerline are averaged yielding the mean vessel area and standard deviation. This standard deviation is used as a measure of the geometric in-homogeneities along the vessel length.

Minimum and maximum vessel area: Minimum and maximum vessel cross-sectional areas are computed from the area curve. The minimum vessel area can be used to quantify vessel stenosis especially in case of pulmonary arteries.

4.5.3 Vessel Orientation and Curvature

4.5.3.1 Vessel Curvature

Vessel curvature quantifies the curvature of the vessel (IVC, SVC, LPA and RPA) at the TCPC junction. To compute this parameter, the first step is to calculate the tangent of the vessel centerline, denoted as T , at the TCPC junction. Suppose s(t) is a curve in the Euclidean space (Figure 4.7), the tangent vector T of this curve is given by the equation

$$T = \frac{ds/dt}{|ds/dt|} \qquad (4.4)$$

Then the derivative $\dot{T}$ is numerically calculated with second order accuracy. The curvature of the vessel centerlines at the TCPC junction can then be calculated as:

$$\kappa = |T \times \dot{T}| \big/ |T|^3 \qquad (4.5)$$
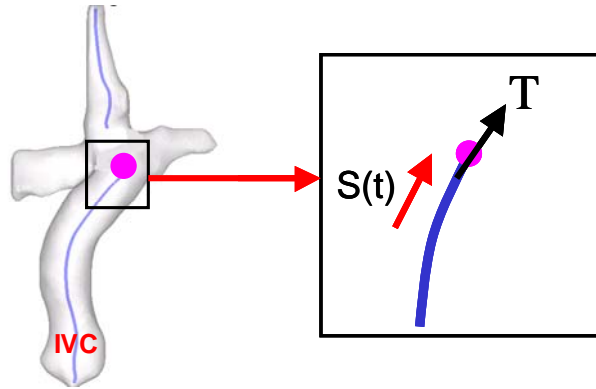
Figure 4.7: Sample TCPC geometry with the skeleton of the venae cavae is shown in the figure. Part of the IVC centerline is zoomed in to show the tangent vector T (black arrow) at the TCPC junction. The red arrow indicates the direction of the space curve s(t), which is the IVC centerline in this scenario.

4.5.3.2 Vessel Collinearity

Using the tangent vectors of the IVC and SVC at the TCPC junction (figure 4.8), a parameter is defined that can be used as an indication of collision of flows coming through these vessels. In this study, this parameter is called "vessel collinearity" and is computed as:

$$\phi = \tfrac{1}{2}\left(\left| \hat{T}_{ivc} \times \hat{r} \right| + \left| \hat{T}_{svc} \times \hat{r} \right| \right) \qquad (4.6)$$

where $\hat{T}$ is the unit vector of the tangent T and $\hat{r}$ is the unit displacement vector between the points where the IVC and SVC meet the junction. By definition, $0 \leq \phi \leq 1$. $\phi = 0$ corresponds to a head-on colliding orientation between the great veins, and $\phi = 1$ corresponds to a configuration where the SVC and IVC flows are anastomosed in parallel with the pulmonary arteries .
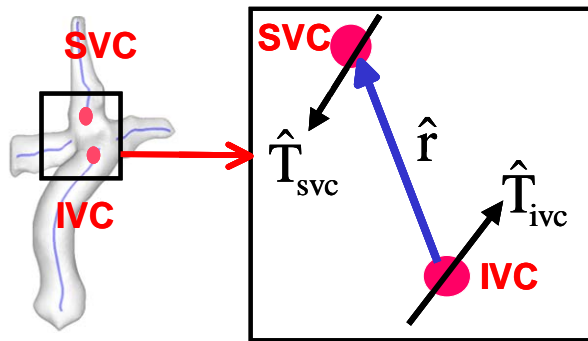
Figure 4.8: Schematic explaining the terms used for collinearity calculation. Sample TCPC geometry with the skeleton of the venae cavae is shown on the left. TCPC junction is enlarged on the right (black box) to show the unit tangent vectors $\hat{T}$ svc and $\hat{T}$ ivc (black arrows). The unit displacement vector $\hat{r}$ is shown in blue arrow.

4.5.4 Vessel Offset

Three vessel offsets are defined: (1) anterior-posterior (AP) offset between IVC and SVC; (2) right-left (RL) offset between IVC and SVC; and (3) PA-VC offset between pulmonary arteries (PA) and the venae cavae (VC). The first two were computed by projecting the displacement vector r along the AP and RL directions, respectively, while the PA-VC offset was computed as the shortest distance between the line connecting RPA to LPA and the line connecting SVC to IVCs, respectively. In the case of a zero PA-VC offset the two lines will intersect each other.

4.6 Fontan Hemodynamic Characterization

The primary purpose of quantitative geometric characterization is to correlate the geometric features with its hemodynamic performance. This section describes the three hemodynamic parameters taken into consideration: (1) power loss within the TCPC, (2) ventricular power output, and (3) cardiac index.

4.6.1 TCPC Power Loss

4.6.1.1 Overview

Power loss across the TCPC is a critical parameter that quantifies the overall efficiency of the connection. Control volume power loss quantification requires the simultaneous knowledge of velocity and pressures. These cannot be computed based on *in vivo* measurements (unless catheterization data are acquired in all four vessels), but can be obtained by conducting *in vitro* experiments or CFD simulations on anatomically accurate TCPC geometries. Two modalities are used in this study to acquire the power loss, CFD simulations and *in vitro* experiments. *In vitro* experiments previously conducted in our laboratory [Kitajima, 2007], provided with power loss data for six patients and CFD studies performed by Whitehead *et al* [Whitehead, 2007] provided power loss for nine patients from our anatomic database. The subsequent sections provide an overview of the experimental and CFD protocols followed for data acquisition and power loss computation.

Anatomically accurate *in-vitro* models are fabricated using stereolithography [De Zelicourt, 2005], based on the reconstructed 3D anatomies obtained in Section 4.2. The *in vitro* model is then inserted in a flow loop, which allows for the control of total cardiac output (CO) as well as IVC/SVC and LPA/RPA flow splits. Global flow rates and static pressures measurements are acquired at each inlet and outlet. These static pressures are corrected for pressure head bias introduced by small changes in the model elevation and then used to compute power losses ($\dot{E}_{loss}$) across the connection using an integrated, control-volume energy balance [De Zelicourt, 2005].

$$\dot{E}_{loss} = \sum_{Inlets} P_i \cdot Q_i - \sum_{Outlets} P_i \cdot Q_i \qquad (4.7)$$

where P_i and Q_i, are the corrected static pressure and volumetric flow rate respectively.

Flow conditions used for the study are shown in Table 4.1 and are based on the phase contrast MRI acquired at the time of the MRI scan. The average flows are then computed through the vessels of interest, which are prescribed at the time of the experiment. The lowest tested flow rates thus corresponded to the resting PC-MRI flow rates, while higher flow rates are used to simulate exercise conditions.

Table 4.1: Flow conditions used in the evaluation of power loss. * indicates the MRI flow conditions.

Patient	Flow Conditions (L/min)
CHOA007	2*, 3,4
CHOA008	2 *, 3,4
CHOP013	2,3 *, 4
CHOA009	2 *, 3,4
CHOA011	4*, 5,6,7
CHOP034	4*, 5.2,6.4,7.6

4.6.1.3 CFD Simulation

The 3D anatomical reconstructions described in section 4.2 are used for grid generation in which vessel volumes are divided into computational elements (meshes). The number of elements varies depending on geometry size and complexity, but ranges from 548,842 to 1,674,440 for the models studied [Whitehead, 2007]. At each element, the governing Navier-Stokes conservation equations of mass and momentum for laminar fluid flow are solved. The CFD computations were performed using the commercial software FIDAP 8.7.4 (Ansys Inc. Canonsburg, PA). Each patient geometry is simulated at MRI flow condition obtained from the PCMRI data averaged over the cardiac cycle.

Power loss through the TCPC is calculated using the control volume method, derived from the macroscopic energy balance equation [Liu, 2004]:

$$\dot{E} = \int\limits_{Surface} \left[p + \frac{1}{2}\rho u_j u_j \right] u_i n_i dS \cong \left(p + \frac{1}{2}\rho v^2 \right) Q \qquad (4.8)$$

where, P is the static pressure, u_i is the velocity component and Q is the volumetric flow rate.

In practical terms, net power loss is calculated by subtracting outlet power from inlet power:

$$\dot{E}_{loss} = \dot{E}_{SVC} + \dot{E}_{IVC} - \dot{E}_{lpa} - \dot{E}_{rpa} \qquad (4.9)$$

where, ($\dot{E}_{SVC} + \dot{E}_{IVC}$) is the outlet power and ($\dot{E}_{LPA} - \dot{E}_{RPA}$) is the inlet power. $\dot{E}_{loss}$ is the power loss in the control volume.

4.6.2 Ventricular Power Output and Cardiac Index

The mechanical energy of blood flow in the ascending aorta in the single ventricle patients is the total energy available to drive blood through both the systemic and the pulmonary beds. This ventricular power output may thus be used as a representation of the work done by the single ventricles of these Fontan patients.

From the PC MRI of the ascending aorta, the ascending aorta is segmented using an in house scheme [Sorenson, 2006 MS thesis], and cardiac output is calculated by integrating the velocities over the entire cardiac cycle. The cardiac output is then normalized by patient body surface area (called Cardiac Index) to facilitate comparison. The cardiac output, mean velocities and the cuff blood pressure measurements are then used in the modified Bernoulli equation to obtain the ventricular power output [Sundareswaran, 2006].

$$\dot{E} = \left(\tfrac{1}{2}\rho V^2_{systole} + P\right)Q_{systole} \tag{4.10}$$

where, $\rho = 1060$ kg/m^3 is the density of blood, $V_{systole}$ is the mean systolic velocity in the ascending aorta, P is the mean arterial pressure , and $Q_{systole}$ is the mean systolic flow rate.

4.6.4 Non-dimentionalization

In order to compare geometric ad hemodynamic features for different patients, the power loss needs to be appropriately indexed or non-dimensionalized. Vessel areas are normalized with patient body surface area (*BSA*).

Since the TCPC power loss, denoted as $\dot{E}_{loss}$ depends on the physical and geometrical characteristics, its functional dependence may be broadly characterized as a function of the blood flow rate (Q), density (ρ), viscosity (μ), BSA, flow split (α) and the specific parameters that describe the geometry completely (mainly, vessel dimensions, angles, orientation, etc). The following equation describes this complex relationship:

$$\dot{E}_{loss} = F\left(Q, \alpha, \rho, \mu, BSA, geometry_i^{'}\right) \tag{4.11}$$

Note that geometry is denoted with subscript *i*, signifying that it may be a vector quantity with several components corresponding to each geometric detail.

All the six variables mentioned in equation 4.11 have any one of the following 3 dimensions – length, mass and time. That means, this relationship could be reduced to a relationship between three dimensionless quantities, expressed in terms of the dimensions length (L), mass (M) and time (T) as explained below [Bukhingham, 1914].

By fluids law, Reynolds number (*Re*), which lumps flow rate, density, viscosity and characteristics length defined by BSA is one of the non-dimensional variables. Flow split α is already non dimensional and is thus the second non-dimensional variable. The geometry can be non-dimensionalized by the patients BSA that forms the third non-dimensional variable. Finally, $\dot{E}_{loss}$ can be non-dimensionalized using BSA, density and cardiac output. i.e.

$$[\dot{E}_{loss}] = [Q]^a [BSA]^b [\rho]^c \qquad \textbf{(4.12)}$$

In terms of their respective dimensions, each of these quantities can be expressed as Power loss in Kgm^2/sec^3 (Work done/Time), cardiac output in L/min, BSA in m^2, density in Kg/m^3. Expressing these quantities in terms of length (L), mass (M) and time (T), we get

$$ML^2T^{-3} = [L^3T^{-1}]^a [L^2]^b [ML^{-3}]^c$$

$$\textbf{(4.13)}$$

Simplifying the above equation and equating dimensionalities for M, L, and T we get the following three equations:

$$c = 1; 3a + 2b - 3c = 2; a = 3 \qquad \textbf{(4.14)}$$

Solving the above equations give, a = 3, b = -2, and c = 1. Thus is has been shown that $\dot{E}_{loss}$ scales with $\rho \frac{Q^3}{BSA^2}$, where ρ is the density of blood in Kg/m^3, Q is the CO in L/min and BSA is the patient body surface area in m^2. So the power losses, $\dot{E}_{loss}$, are thus normalized by E_0, defined as: $\qquad E_0 = \rho \frac{Q^3}{BSA^2} \qquad$ (4.15)

and the non dimensional relationship reduces to:

$$\dot{E}_{loss} \Big/ E_0 = f(\alpha, \text{Re}, geometry') \qquad \textbf{(4.16)}$$

4.7 Patient Population

4.7.1 Overview

In our laboratory, a database of over 200 patients has been created as part of an ongoing study seeking to better understand the Fontan hemodynamics and improve the TCPC design. This database contains anatomical PC MRI and necessary clinical information from 3 major hospitals in the United States - Egleston Hospital, Atlanta (CHOA), Children's Hospital of Philadelphia (CHOP) and University of North Carolina (UNC). Informed consent was obtained from all patients and all study protocols complied with the Institutional Review Boards of participating hospitals and the Georgia Institute of Technology.

4.7.2 Details on the database

The database includes details of all the three stages of Fontan surgery and the different templates available for each of these stages. Table 4.2 summarizes the number of patients in each category.

4.7.3 Inclusion criteria for the study

The work described in this thesis is a retrospective study designed to (i) compare the geometrical features of different TCPC templates and (ii) to assess the correlation between these geometrical parameters and the associated hemodynamic performances. The main focus is on EC and IA templates as these are the most widely represented anatomical types in the database. Accordingly, the inclusion criteria for this study are: (1) availability of experimental and CFD power loss data (2) availability of clinical information necessary to categorize each study group (3) the anatomic reconstruction

with no visible artifacts (some geometries have loss of MRI signal due to the presence of

"clips" in the vessels that surgeons attach to the vessel during surgery).

Table 4.2: Summary of patients in each Fontan category present in the database
    (as of March, 2007)

Fontan Category	Number of patients
Stage 1	1
Stage 2	
- Glenn	41
- Hemi Fontan	10
Stage 3	
- Intra atrial	85
- Extra cardiac	29
- Bi-lateral SVC	8
- Atrio pulmonary	4
- IVC-MPA connection	1
- Interrupted IVC	3

In addition the EC and IA TCPCs, there are some marginal groups that are also

analyzed in the study. One of them is Fontan with bi-lateral SVC. The inclusion criteria

for this group are similar to that of EC and IA with one addition, presence of two superior venae cavae.

In order to see how the geometrical characteristics of Fontan patients evolve with time the geometrical characteristics of pr and post Fontan surgical pairs are also included in the study. For this group, the criterion addition to that of EC and IA is the presence of pre Fontan PCMRI data.

Based on these criteria 34 patients were selected from the database for this study. Among these 34 patients, there are 13 intra atrials, 13 extra cardiacs, 5 bi-lateral SVC and 3 pre Fontan anatomies. A tabulated form of patients chosen in each category is shown in table 4.4. Details of the study groups are provided in the following sections.

Table 4.3: Summary of patients in each Fontan category studied in this work (The 3 pre-Fontan models are not included in this list)

Fontan type		Post-Fontan	Total
Intra atrial	12	1	13
Extra cardiac	12	1	13
Bi-lateral SVC	4	1	5

4.7.4 Extra cardiac vs. Intra atrial

At the time of patient selection (November 2006), there were about 75 intra atrial and 23 extra cardiac geometries in the database. Among these 26 patients, 13 each of extra cardiac (EC) and intra atrial (IA) were chosen based on the criteria defined in section 4.7.1. All these patients were imaged either at CHOA or CHOP.

60

Among the 13 EC patients, 2 are from CHOA and 11 from CHOP, while among the IA patients, 4 are from CHOA and 9 from CHOP. Details of the studied EC and IA patient populations are provided in Tables 4.5 and 4.6, respectively. 4 EC patients and 6 IA patients within the study group had an initial diagnosis of HLHS. Also, 16 of the 26 patients had bi-directional Glenn (BDG) as their 2nd stage Fontan and remaining 10 had a hemi-Fontan.

For all 26 patients, geometric characterization of the TCPC was performed to quantitatively differentiate EC and IA. Since there was a clear distinction about the diagnosis of the patients as HLHS and non-HLHS, a detailed analysis of these two categories are also performed where necessary. *In-vitro* power loss quantification for a range of cardiac outputs (CO) representing rest through exercise conditions and PA flow splits is available for 6 of 26 patients as well as CFD power loss data is available for nine of 26 patients. PCMRI data for the ascending aorta are available for 13 of 26 patients, which enabled estimation of the ventricular power output of the heart (Table 4.4). These parameters along with the cardiac index are used to analyze the hemodynamic correlates of the TCPC.

Table 4.4: Ventricular power output computed for the patients

Patient	Systolic Pressure (mm Hg)	Diastolic Pressure (mm Hg)	Mean Pressure (mm Hg)	Mean Velocity (cm/sec)	Power (watts)
CHOP006	135	65	89.50	20.96	1.64
CHOP007	119	62	81.95	50.63	1.90
CHOP013	123	61	85.80	31.94	1.22
CHOP067	103	64	78.18	26.16	1.51
CHOP089	110	54	66.44	27.12	1.62
CHOP090	126	69	83.78	25.85	2.78
CHOP091	98	62	72.80	19.66	1.47
CHOP095	96	67	79.61	18.86	1.61
CHOP008	137	69	123.40	1.62	0.58
CHOP018	123	65	82.40	23.27	1.95
CHOP030	116	74	82.40	59.95	2.79
CHOP068	107	54	66.72	21.88	0.82
CHOP092	110	70	83.33	18.55	0.84

Table 4.5: Clinical diagnosis of patients with extra cardiac Fontan repair.

Patient	Diagnosis	Fontan Type	Hemi/BDG	BSA (m^2)	Age (Yrs)
CHOA007	HLHS	EC	BDG	0.79	6
CHOA008	HRHS,TA	EC	BDG	0.69	5
CHOP006	HLHS	EC	Hemi	1.05	10
CHOP007	HRHS, Ebstein's anomaly	EC,DSK-ASD repair	BDG	1.02	8
CHOP013	HLHS,ASD	EC	Hemi	0.83	6
CHOP067	SV-DI LV,VPS-TGA	EC	BDG	1.064	9
CHOP085	HLHS	EC	BDG	0.589	3
CHOP088	DX, Juxtaposition of atria appendages,TA, TGA,AA hypoplasia	EC-Fenestrated	BDG	0.544	3
CHOP089	TA,VSD	EC-Fenestrated	BDG	0.872	7
CHOP090	PA,IVS, RV-Hypertrophy	EC-Fenestrated	BDG	1.152	8
CHOP091	DO-RV,IVS,MA,PA	EC-Fenestrated	BDG	0.994	8
CHOP095	DI LV,PA	EC-Fenestrated	BDG	1.253	8
CHOP116	Ebstein's Anomaly	EC	BDG	0.793	8

EC – extra cardiac; Hemi - hemi-Fontan; BDG - bidirectional glenn; HRHS - hypoplastic right heart syndrome; HLHS - hypoplastic left heart syndrome; TA - tricuspid atresia; ASD - atrial septal defect; VSD - ventricular septal defect; SV - single ventricle; LV - left ventricle; RV - right ventricle; DI - double inlet; DO - Double Outlet; TGA - transposition of great arteries; DX – dextrocardia; AA - aortic arch; PA - pulmonary atresia; DSK - Damus-Stansel-Kaye procedure;   MA -Mitral Atresia; IVS - intact ventricular septum

Table 4.6: Clinical diagnosis of patients with intra atrial Fontan repair.

Patient	Diagnosis	Fontan Type	Hemi/BDG	BSA (m^2)	Age (Yrs)
CHOA004	HRHS,TA,VSD, PS	IA	BDG	0.56	3
CHOA009	SV-DI AV connection	IA,DSK	BDG	0.58	2
CHOA011	HLHS	IA-Fenestrated	BDG	1.21	11
CHOA027	HRHS, TGA, TA, VSD, LPA hypoplasia	IA, DSK, fenestrated	BDG	0.58	2
CHOP008	HLHS	IA	Hemi	1.94	16
CHOP018	HLHS,ASD	IA	Hemi	1.23	12
CHOP030	TA,VSD	IA	Hemi	1.32	10
CHOP034	HRHS,SV,DX, TA,VSD,PS	IA	Hemi	1.19	11
CHOP037	PA,HRHS	IA	Hemi	1.49	15
CHOP068	HLHS	IA	Hemi	0.94	6
CHOP073	HLHS	IA	Hemi	0.963	9
CHOP092	HLHS,TGA, Hypoplastic AA, VSD	IA-Fenestrated	Hemi	0.495	1
CHOP096	PA	IA-Fenestrated	BDG	1.063	10

IA -intra atrial; Hemi - hemi-Fontan; BDG - bidirectional glenn; HRHS - hypoplastic right heart syndrome; HLHS - hypoplastic left heart syndrome; TA - tricuspid atresia; ASD - atrial septal defect; VSD - ventricular septal defect; SV - single ventricleAV - atrioventricular; DI - double inlet; TGA - transposition of great arteries; DX – dextrocardia; AA - aortic arch; PA - pulmonary atresia; PS - pulmonary stenosis; DSK - Damus-Stansel-Kaye procedure

4.7.5 Pre vs. post Fontan

Among the 34 patients MR images were available before and after the TCPC surgery for 3 pairs (i.e. images acquired at the 2nd stage and 3rd stage of the surgery). This allowed us to analyze the evolution of the vessel geometric characteristics between the Glenn and TCPC stages. Table 4.5 summarizes the information of these 3 surgical pairs.

Table 4.7: Clinical diagnosis of patients before and after Fontan surgery

Patient		Diagnosis	Fontan Type	Hemi/BDG	BSA (m^2)	Age (Yrs)
Pair 1	CHOA014	TGA, AVV atresia, HRHS, VSD	-	BDG	0.53	1
	CHOA027	HRHS, TGA, TA, VSD, LPA hypoplasia	IA, DSK, fenestrated	-	0.58	2
Pair 2	CHOP053	Heterotaxy, DX, CCAVC unbalanced to the RV, RV aorta with PA, hepatic veins and IVC to RA, PV to LA	-	BDG	0.63	4
	CHOP055	Heterotaxy, DX, CCAVC unbalanced to the RV, RV aorta with PA, hepatic veins and IVC to RA, PV to LA	EC, bi-lateral SVC	-	0.63	4
Pair 3	CHOP057	HLHS	-	BDG	0.43	2
	CHOP085	HLHS	EC	-	0.589	3

BDG - bidirectional glenn; HRHS - hypoplastic right heart syndrome; HLHS - hypoplastic left heart syndrome; TA - tricuspid atresia; VSD - ventricular septal defect; RV - right ventricle; LA - left atrium; RA - right atrium; AV - atrioventricular; TGA - transposition of great arteries; DX – dextrocardia; PA - pulmonary atresia; PVS – pulmonary valve stenosis; DSK - Damus-Stansel-Kaye procedure; VPS – valvular pulmonary stenosis; AVC - Atrio-ventricular Canal

2 patients in the pre-post pair, CHOA027 and CHOP085 also comes under the category of IA and EC groups respectively, and are used for the comparison of EC vs. IA study. Also CHOP055, the post pair of CHOP053 is included in the bi-lateral SVC analyses also.

4.7.6 Bilateral SVC

Because of their unique characteristics of having 2 SVCs, one connected to the right side (RSVC) and one to the left side (LSVC) of the pulmonary arteries, patients with bilateral SVCs stand out as a separate template in the database. Geometric characterization is thus performed on this TCPC type as well. For this purpose, 5 TCPCs with bilateral SVCs are analyzed in this study. The selection criteria are defined in section 4.7.1. Clinical details of these patients are listed on Table 4.6.

Table 4.8: Clinical diagnosis of Bilateral SVC patients

Patient	Diagnosis	Fontan Type	Hemi/BDG	BSA (m^2)	Age (Yrs)
CHOA039	HLHS	EC	---	0.575	3
CHOP019	HLHS	EC	---	0.91	7
CHOP022	DX, SV-DO RV, PA, Heterotaxy, AVC	EC	Hemi	1.01	9
CHOP032	Common AVV, super inferior ventricles, DORV with PS	EC	---	2.01	18
CHOP055	Heterotaxy, DX, CCAVC unbalanced to the RV, RV aorta with PA, hepatic veins and IVC to RA, PV to LA	EC	-	0.63	4

HLHS - hypoplastic left heart syndrome; TA - tricuspid atresia; VSD - ventricular septal defect; SV – single ventricle; RV - right ventricle; LA - left atrium; RA - right atrium; AV - atrioventricular; TGA - transposition of great arteries; DX – dextrocardia; DO- double outlet; PA - pulmonary atresia; PVS – pulmonary valve stenosis; DSK - Damus-Stansel-Kaye procedure; VPS – valvular pulmonary stenosis; AVC - Atrio-ventricular Canal

4.8 Statistical Analysis

To perform the statistics on the analyzed data, the first task is to test the normality of the data. The normality test showed that all comparative data are non-normal and correspond to a two-sample population (EC vs. IA). Hence the non-

parametric Mann-Whitney test is used to examine statistical significance among the various geometric parameters evaluated. All statistics are performed using the software Minitab (Minitab Inc, PA).

The Mann-Whitney test is a non-parametric test used for assessing two samples of observation coming from the same distribution. In this study, the two samples extra cardiac and intra atrial are coming from the same distribution – Fontan surgical group. Here the null hypothesis is that the two samples are drawn from a single population, and therefore that probability distributions are equal.

Because of the low sample size of 3 patients for pre-post Fontan pair and 5 bi-lateral SVCs no statstical analysis could be performed on these study groups.

Factors are considered statistically significant for p values <0.05. To examine the association between anatomic and hemodynamic parameters, a regression analysis for two variables was performed using Microsoft Excel (Microsoft Office 2000, Microsoft). P values <0.05 are considered statistically significant. P values slightly higher than 0.05 are also reported as nearly significant findings.

CHAPTER 5

RESULTS

5.1 Overview

This chapter presents the results of the geometric analyses starting with the validation studies conducted in idealized TCPC geometries. The following section then moves on to the patient-specific anatomies selected from the database, detailing the results obtained for the different study subsets of the Fontan geometries, namely extra cardiac vs. intra atrial, pre vs. post Fontan and bi-lateral SVC. Finally the third and last section provides the hemodynamic correlates of the TCPC anatomies, using the power losses computed using CFD simulations and *in vitro* experiments and the ventricular power output when they are available.

5.2 Skeletonization Results – Specific Aim1

The skeletonization method described in Chapter 4 was successfully implemented. However, prior to applying it to patient-specific anatomies and drawing any clinical conclusions from our findings, a critical step was to validate it on geometries with known geometrical parameters. Accordingly, this section first goes over the validation studies and demonstrates the results obtained when skeletonizing patient-specific TCPC anatomies.

5.2.1 Validation Studies

In order to validate the skeletonization approach, the method was tested on idealized TCPC models whose details are provided in Chapter 4. The two validation models along with their corresponding centerline representations are shown in figure 5.1. Note that the centerlines are computed for each vessel separately for the ease of comparison.

(a)   (b)
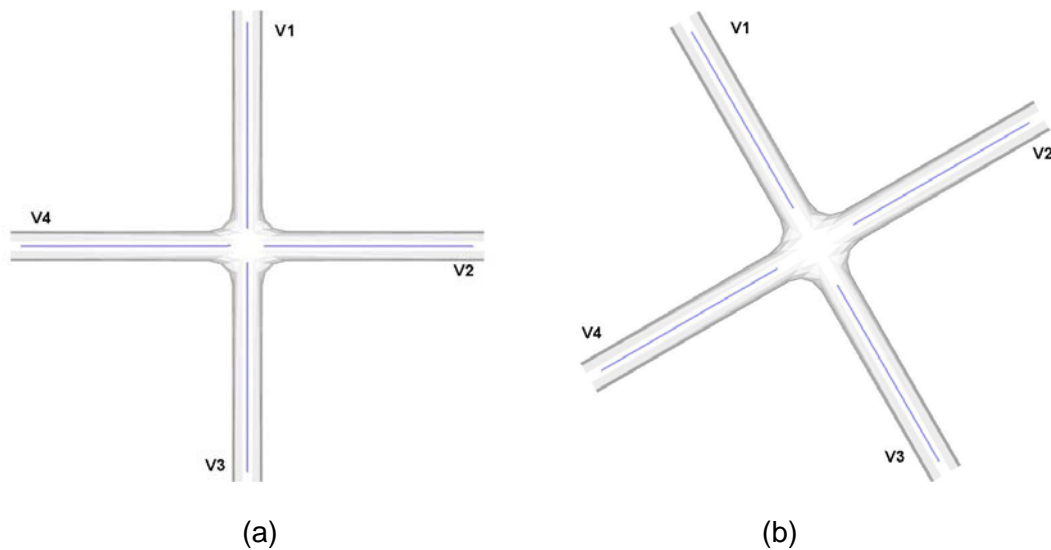
Figure 5.1: Results of method validations on idealized TCPC models are shown here. (a) Idealized Fontan geometry with zero offset between the venae cavae. (b) The same zero offset model as in figure (a) rotated at 30^0 with respect to its original co-ordinates. The blue lines are the centerline representation of the models and v1, v2, v3 and v4 represents the vessels of the TCPC geometry.

For the representation of the centerline to be accurate, the vessel slicing in the final iteration should be done in directions perpendicular to the vessel axis. This is indeed what was observed for our validation test-case (see Figures 5.2 and 5.3).
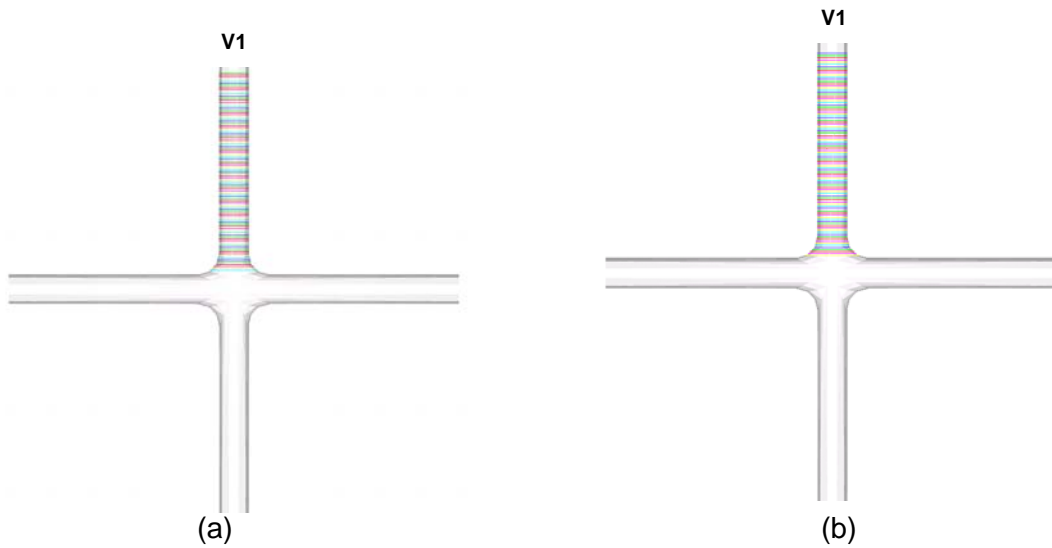
Figure 5.2: Slices obtained after the (a) first and (b) second iteration on vessel v1 of the zero-offset validation model.
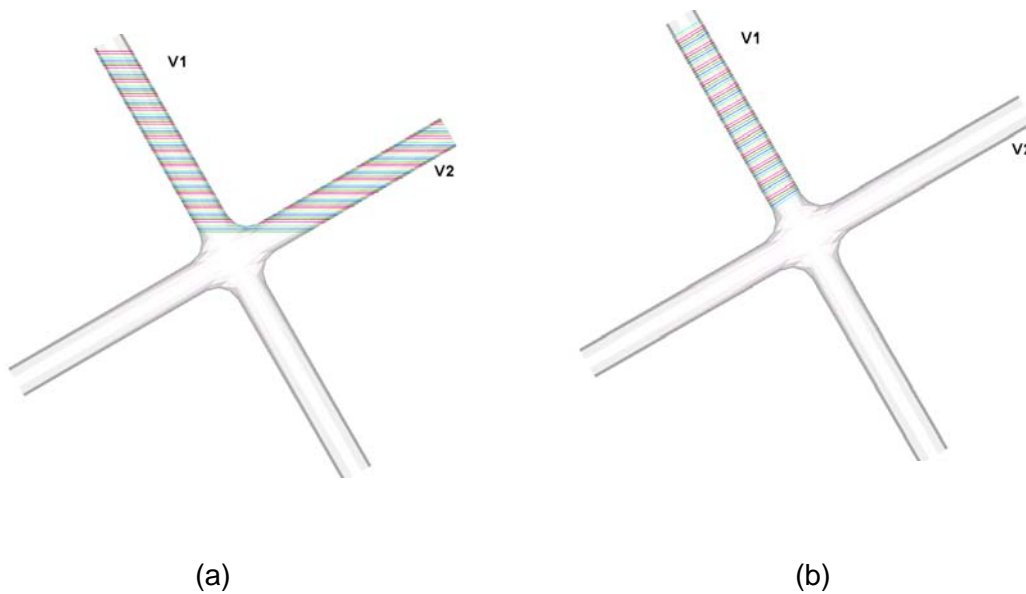
Figure 5.3: Slices obtained after the (a) first and (b) second iteration on vessel v1 of the 30^0 rotated zero-offset model. Note the over estimation of slice area and extension of slices onto vessel v2 in figure (a).

Figure 5.2 shows the results of vessel slicing on vessel v1 of the idealized model after the first and second iterations, respectively. A perfect match is obtained for both cases because the vessel axis is exactly perpendicular to the slices taken in this case.

However in Figure 5.3 the same geometry is rotated at a fixed angle with respect to the center so that the vessel axis is now off from the initial slicing direction. Over estimation of the slice area as well as the fact that slicing is extended to vessels that are not of interest (vessel v2 in this example) are clearly visible in Figure 5.3a. However, as shown in Figure 5.3b, the slices are back to a orientation perpendicular to the vessel axis, resulting in an accurate centerline of the geometry, as soon as in the 2nd iteration

Figure 5.4 shows the area plots obtained for the validation models. These plots provide quantitative details of the cross-sectional area variations along the vessel length for the different tested configurations. For the1st configuration with no rotation (Figure 5.4a, the vessel area starts at the value ~225 mm^2 and then decreases to ~150 mm^2. The initial increase in area is because the region where the vessel connects to the TCPC is also included in the picture. The good agreement between the first and second iteration curves show that the respective centerlines are also converging with one another, which was expected since, with no rotation, the initial slicing direction was exactly perpendicular to the vessel axes. Now looking at the rotated configuration (Figure 5.4b), it is very clear that the initial slices shown using the curve 1 (shown in blue) yielded inaccurate area estimations (see Figure 5.3a). Despite such inaccuracy in the initial estimates, the accurate slices were obtained after the second iteration, which is shown by curve 2 (shown in pink).
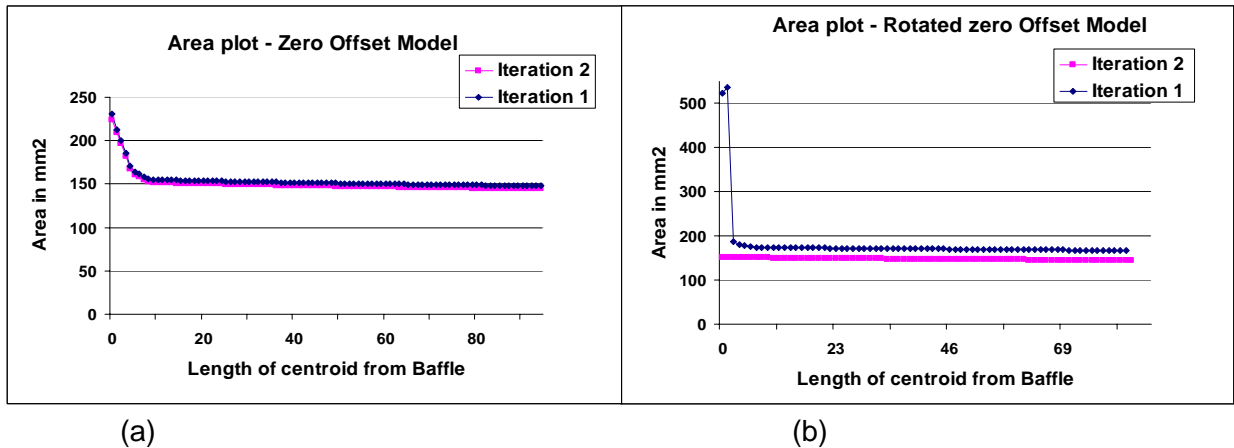
Figure 5.4: Area plot showing the cross sectional area of vessel v1 for the zero offset model (a) with no rotation and (b) with rotation. Note the good match between the first and second iteration curves in figure (a) and the area overestimation shown in figure (b).

Since both test cases employed the exact geometry, both plots are expected to be identical and equal to the design specifications. The zero-offset model was designed with vessel diameters of 14mm. Accordingly, the expected cross-sectional area was of 153.86mm^2. Figure 5.5 compares this theoretical value to the output of the skeletonization approach to both configurations. It should be noticed that (1) the skeletonization method yielded identical results irrespective of the initial slicing orientation for both configurations; and (2) the cross-sectional areas computed in both cases were of about 148mm^2 (diameter of 13.7mm), which was in close agreement with the theoretical value of 153.86mm^2. Both observations are critical features that validated the ease of use of the developed method (with minimum constraints on the initial model orientation) as well as for its reliability and accuracy. An excel spreadsheet of all the computed parameters for the validation studies is provided in Appendix B.

Area plot - Zero Offset Model
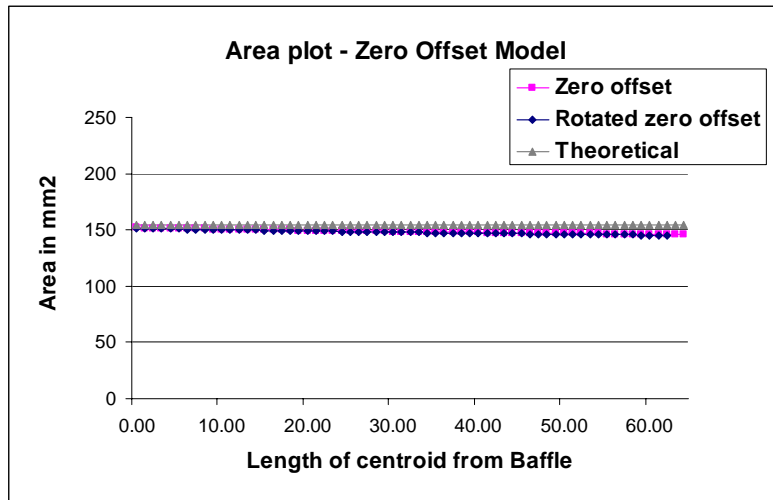
Figure 5.5: Comparison of the cross-sectional area plots obtained for the zero-offset model after 2nd iteration with and without rotation (pink and blue, respectively) against the theoretical value (gray).

5.2.2 Application of skeletonization – Centerline of TCPC geometries

TCPC geometries that have been analyzed using the skeletonization approach in each study category are shown in figures 5.6 to 5.9. Figure 5.6 shows the 3 pairs of pre and post Fontan groups that have been used in this study along with their centerline representation and figure 5.7 shows the same for the four bilateral SVC models. Figure 5.8 and 5.9 presents the skeletonization and geometries of the 12 EC and 12 IA patient groups, respectively, underscoring their large geometric variability and complexity. In all these Figures, the geometries are oriented such that the vessel pointing to the top of the page is the SVC, towards the bottom is the IVC, to the left is the RPA and to the right is the LPA.
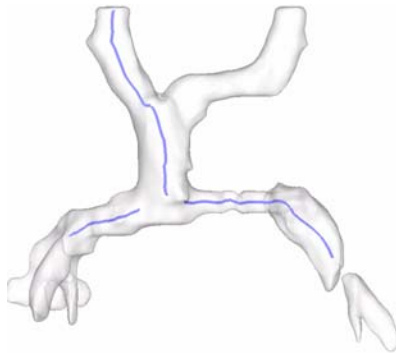
PAIR1:   CHOA014   CHOA027
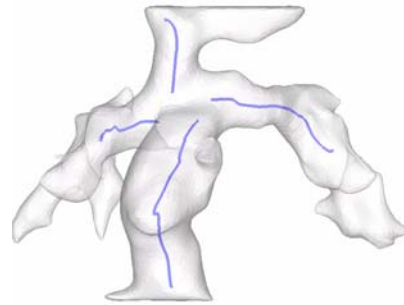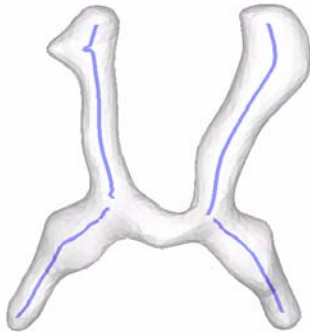
PAIR 2:   CHOP053   CHOP055
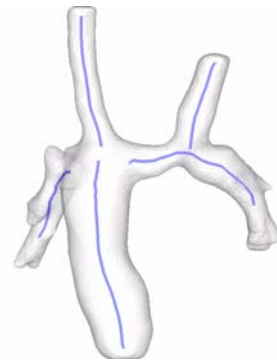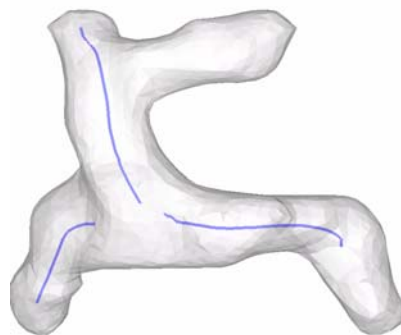
PAIR 3:   CHOP057   CHOP085
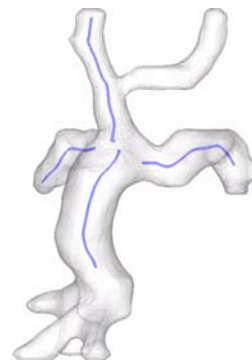
Figure 5.6: 3D reconstructed TCPC anatomies with centerline curves for the three pairs of pre and post Fontan models. Pre Fontan models are shown on the left side while post Fontan models are shown on the left. Since CHOP055 is a bi-lateral SVC it is included in the analysis of bi-lateral SVC also. Similarly, CHOA027 (IA geometry) and CHOP085 (EC geometry) are used in the analysis of EC vs. IA.

CHOP019

CHOP022

CHOP032

CHOA039
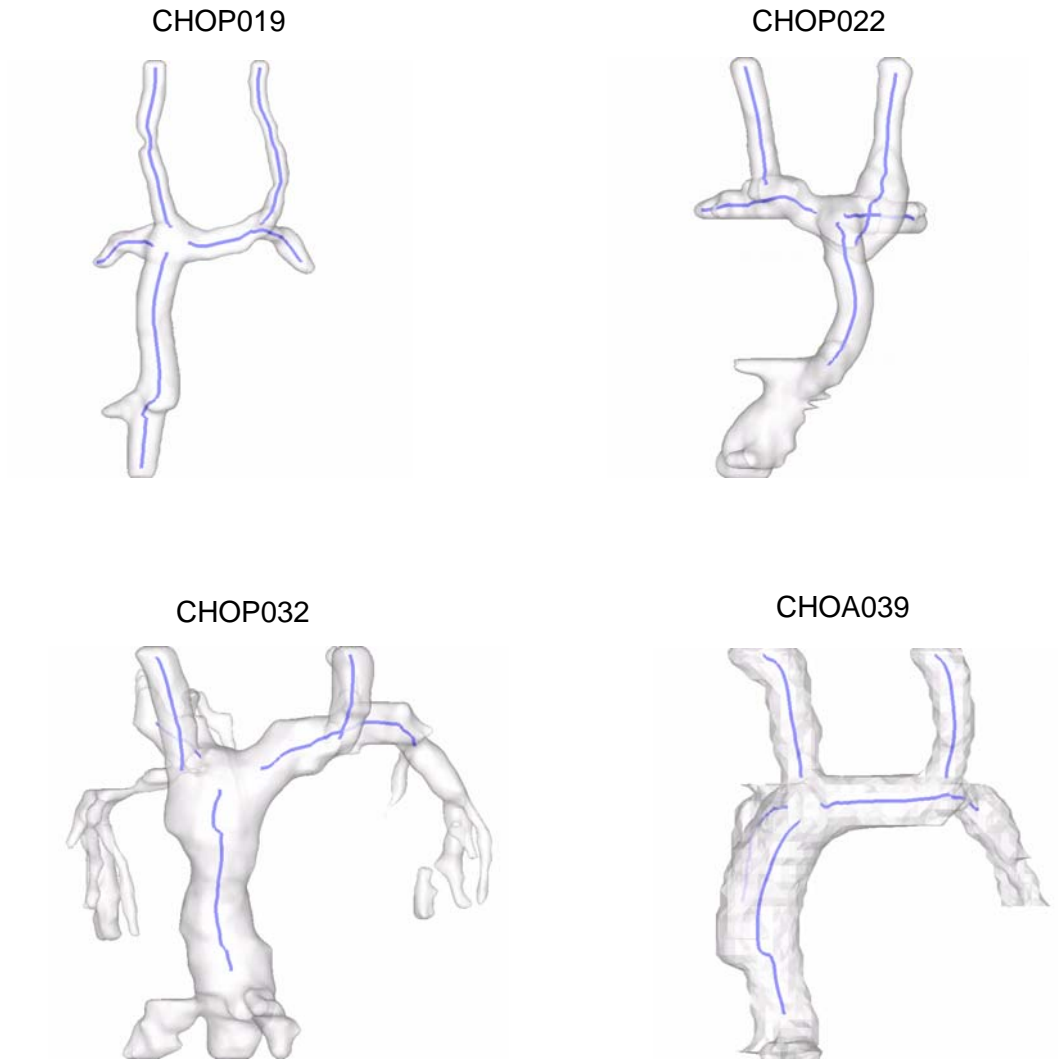
Figure 5.7: 3D reconstructed TCPC geometry along with the centerline curves for the 4 Bilateral SVC models. SVC seen on the right hand side is called LSVC and the one on the left hand side is the RSVC. The fifth bi-lateral SVC in this category is CHOP055, and it is shown in figure 5.6.
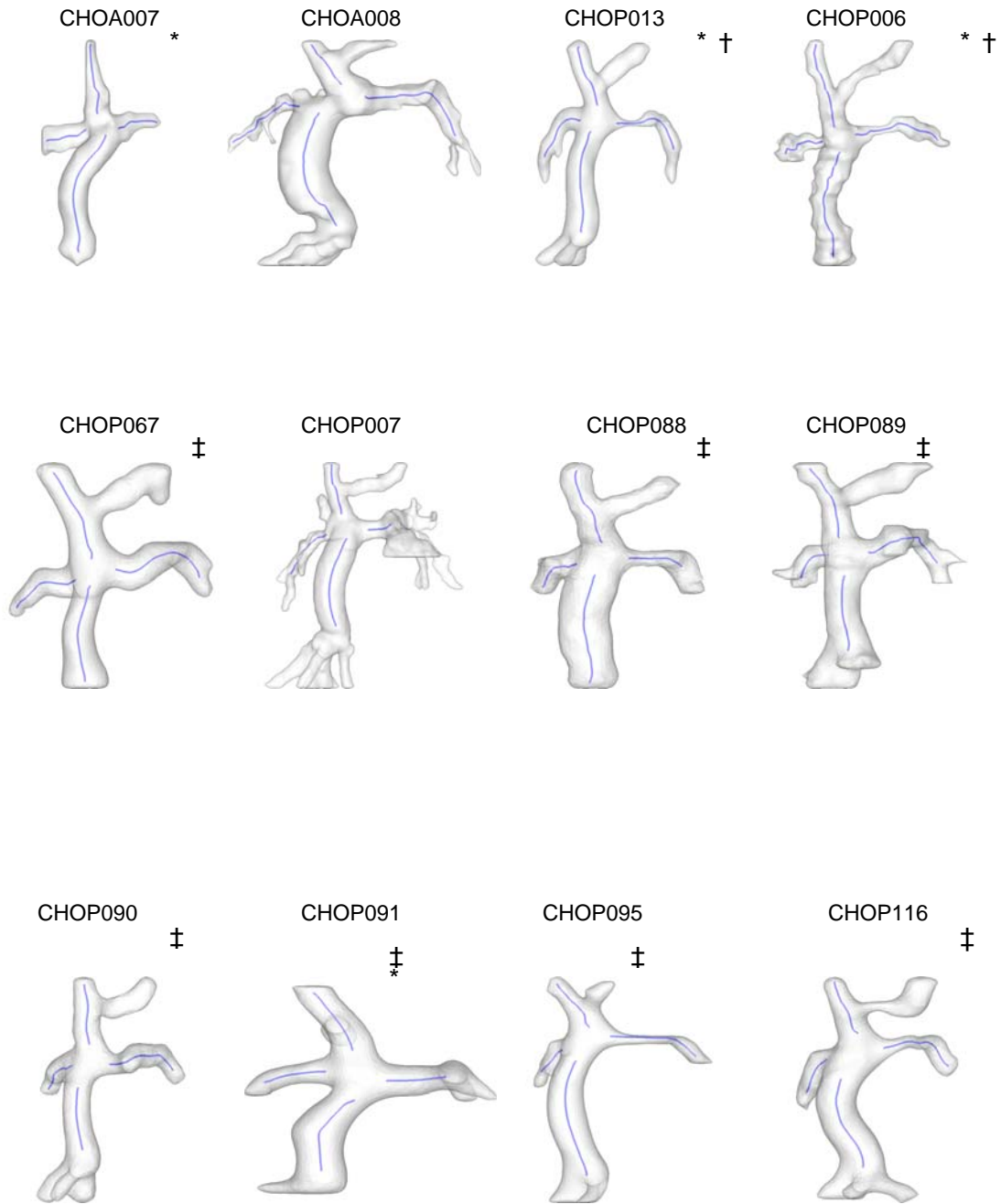
Figure 5.8: 3D reconstructed TCPC anatomies with centerline curves for extra cardiac geometries; the special characters shows the subgroups within each category - * HLHS, † hemi, ‡ - BDG.
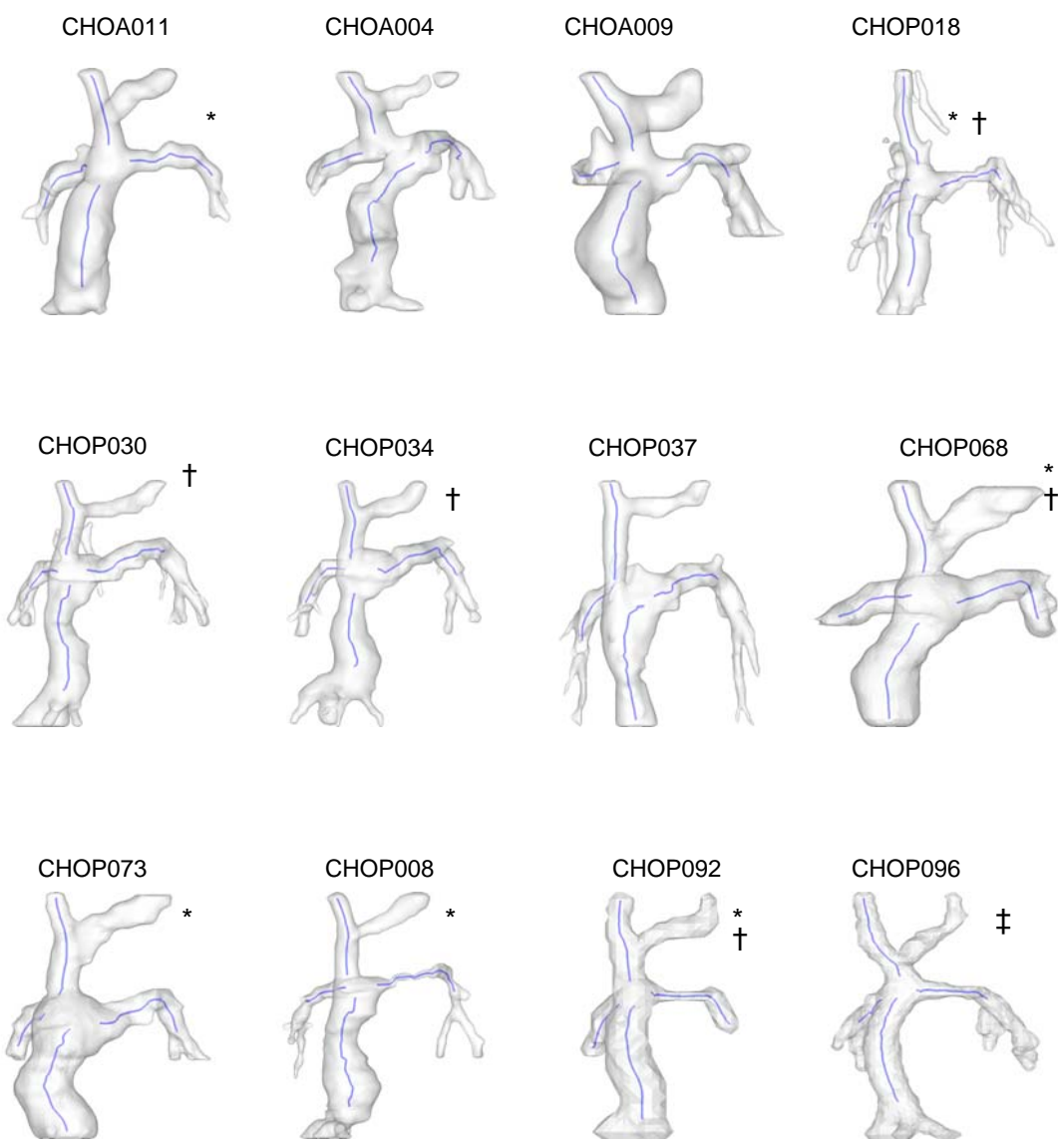
Figure 5.9: 3D reconstructed TCPC anatomies with centerline curves for intra atrial geometries; the special characters shows the subgroups within each category - * HLHS, † hemi, ‡ - BDG.

5.3 Geometrical Characteristics of the TCPC – Specific Aim 2

This section focuses on the quantification and analysis of the parameters retained to characterize the TCPC geometry, namely the vessel area, the vessel orientation and curvature and the vessel offsets. This analysis was performed on the following study subgroups - extra cardiac vs. intra atria; pre vs. post Fontan; and Bilateral SVC.

5.3.1 Extra cardiac vs. Intra atrial TCPC

Results of the geometric characterization performed in 13 extra-cardiac (EC) and 13 intra-atrial (IA) models are shown here. In order to isolate factors others than the procedure used for the 3rd stage alone, these two study groups are further subdivided into (1) HLHS vs. non-HLHS (2) IA-HLHS, IA – non-HLHS, EC – HLHS, EC – non-HLHS and (3) Glenn vs. hemi-Fontan, wherever it is necessary. A summary of all the computed values for EC and IA models along with their p values are given in Table 5.1.

Table 5.1: Summary of the computed values of geometric characteristics for 13 EC and 13 IA geometries.

Computed Variables	Extra Cardiac	Intra Atrial	P Value
Mean Vessel Cross-Sectional Area / BSA			
IVC	$3.67 \times 10^{-4} \pm 1.83 \times 10^{-4}$	$4.03 \times 10^{-4} \pm 1.71 \times 10^{-4}$	0.2917
SVC	$1.65 \times 10^{-4} \pm 0.67 \times 10^{-4}$	$1.34 \times 10^{-4} \pm 0.63 \times 10^{-4}$	0.0874
RPA	$1.18 \times 10^{-4} \pm 0.70 \times 10^{-4}$	$1.19 \times 10^{-4} \pm 0.62 \times 10^{-4}$	0.2917
LPA	$1.12 \times 10^{-4} \pm 0.59 \times 10^{-4}$	$0.95 \times 10^{-4} \pm 0.41 \times 10^{-4}$	0.1704
Vessel Cross-Sectional Area Ratio			
LPA/IVC	0.32 ± 0.19	0.27 ± 0.15	0.2534
LPA/SVC	0.69 ± 0.34	0.79 ± 0.42	0.1427
RPA/IVC	0.34 ± 0.15	0.31 ± 0.12	0.1562
RPA/SVC	0.72 ± 0.28	0.89 ± 0.26	0.0443
Vessel Area Standard deviation / BSA			
IVC	$3.42 \times 10^{-5} \pm 1.96 \times 10^{-5}$	$9.17 \times 10^{-5} \pm 4.55 \times 10^{-5}$	0.0006
SVC	$4.17 \times 10^{-5} \pm 1.29 \times 10^{-5}$	$3.23 \times 10^{-5} \pm 1.7 \times 10^{-5}$	0.0970
RPA	$2.38 \times 10^{-5} \pm 1.39 \times 10^{-5}$	$2.95 \times 10^{-5} \pm 2.13 \times 10^{-5}$	0.4426
LPA	$3.51 \times 10^{-5} \pm 2.22 \times 10^{-5}$	$3.89 \times 10^{-5} \pm 1.80 \times 10^{-5}$	0.2722
Minimum Vessel Cross-Sectional Area / BSA			
RPA	$7.99 \times 10^{-5} \pm 5.97 \times 10^{-5}$	$7.71 \times 10^{-5} \pm 4.64 \times 10^{-5}$	0.3537
LPA	$6.57 \times 10^{-5} \pm 4.64 \times 10^{-5}$	$4.71 \times 10^{-5} \pm 2.92 \times 10^{-5}$	0.1183
Vessel Curvature at the TCPC junction			
IVC	0.19 ± 0.11	0.26 ± 0.19	0.2179
SVC	0.22 ± 0.19	0.18 ± 0.16	0.4199
RPA	0.34 ± 0.43	0.22 ± 0.26	0.0705
LPA	0.21 ± 0.17	0.16 ± 0.11	0.3537
IVC-SVC Collinearity	0.54 ± 0.11	0.48 ± 0.28	0.0562
IVC-SVC AP offset / BSA$^{1/2}$	$3.44 \times 10^{-3} \pm 3.4 \times 10^{-3}$	$2.36 \times 10^{-3} \pm 1.81 \times 10^{-3}$	0.1704
IVC-SVC RL offset / BSA$^{1/2}$	$4.6 \times 10^{-3} \pm 3.01 \times 10^{-3}$	$4.47 \times 10^{-3} \pm 4.33 \times 10^{-3}$	0.2917
PA-VC Offset / BSA$^{1/2}$	$7.01 \times 10^{-3} \pm 2.01 \times 10^{-3}$	$7.51 \times 10^{-3} \pm 2.64 \times 10^{-3}$	0.4655

The mean and standard deviation of vessel areas computed for the EC and IA patient groups are shown in Figure 5.10. Although the mean cross-sectional areas are larger for the SVC, LPA and RPA in case of EC compared to the IA connections, there was no statistically significant difference for any of them (Figure 5.10a). Standard deviations of the cross sectional area computed along the vessel length on the other hand did reveal statistically significant differences between the two groups with regard to the IVC area variation with $p = 0.0006$ (Figure 5.10b). Another statistically significant difference ($p = 0.0443$) was observed in the ratios of mean cross-sectional areas of RPA to SVC between the EC and IA (Figure 5.11).

(a)   (b)
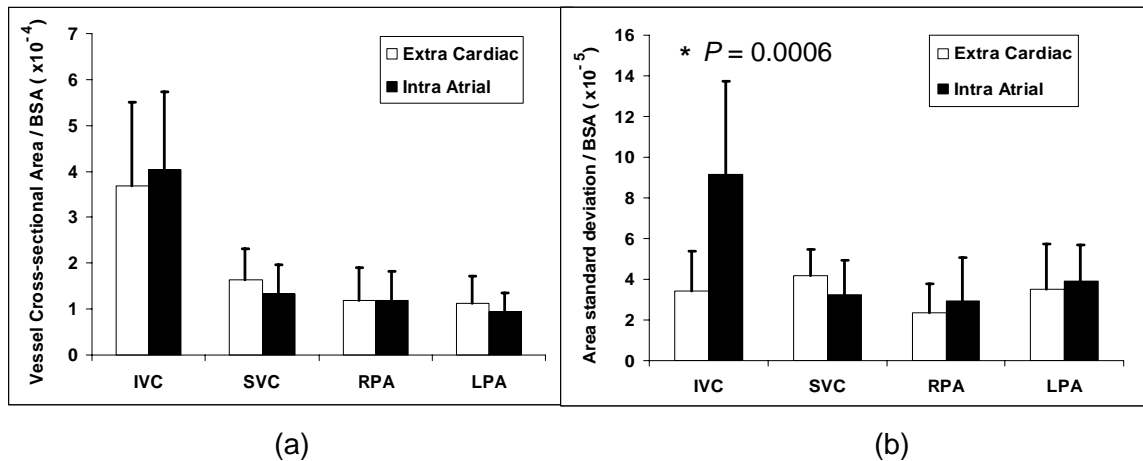
Figure 5.10: Vessel area characteristics with (a) mean and (b) standard deviation of each vessel in the vicinity of the TCPC compared between EC and IA patient groups (N=13 each).
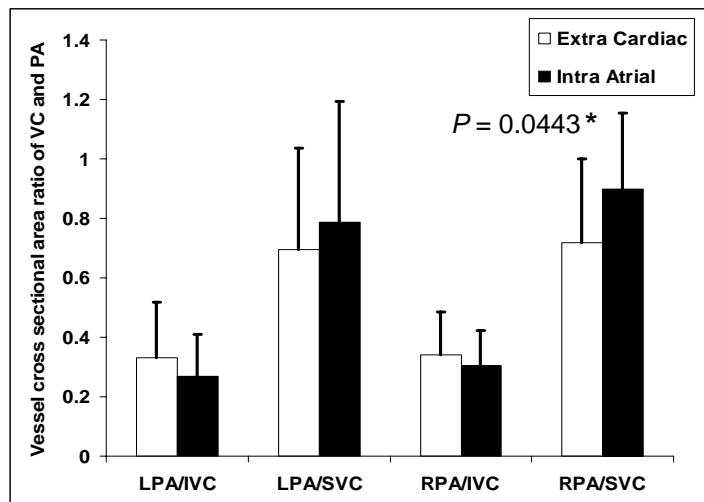
Figure 5.11: Vessel area ratios between the venae cavae and pulmonary arteries for EC and IA patient groups (N=13 each).

There was no statistically significant difference in minimum PA cross-sectional areas (i.e. smallest cross-section along the length of the skeletonized PA) between the EC and IA patient groups. However, as shown in Figure 5.12a, the minimum LPA cross-sectional area was found to be significantly lower (p = 0.016) than the RPA among the IA population. A potential explanation for the minimum LPA cross-sectional area to be smaller than the minimum RPA cross-sectional area is the presence of LPA stenosis after aortic reconstruction, which is typically associated with the surgical repairs of HLHS patients. In order to test for this hypothesis, the study groups were reorganized as HLHS and non-HLHS patients (Figure 5.12b). There was no statistical difference between minimum LPA and RPA cross-sectional areas for non-HLHS patients, while the minimum LPA cross-sectional area was significantly smaller than the minimum RPA cross-sectional area (p = 0.0106) among HLHS patients. Furthermore, the minimum LPA cross-sectional area was found to be significantly smaller for HLHS than for non-HLHS patients (p = 0.0163). Investigating the question a little further, the two-subgroup classifications were combined leading to four categories: IA-HLHS, IA-non-HLHS, EC-

HLHS and EC-non HLHS. Here again minimum PA cross-sectional areas are compared across all four subgroups (Figure 5.12c). Among HLHS patients, the LPA had a significantly smaller (p = 0.0227) minimum cross-sectional area than the RPA for the patients with IA connection. Also, for non-HLHS patients, the minimum LPA cross-sectional area was smaller for patients with an IA TCPC than for those with an EC TCPC (p = 0.0533).
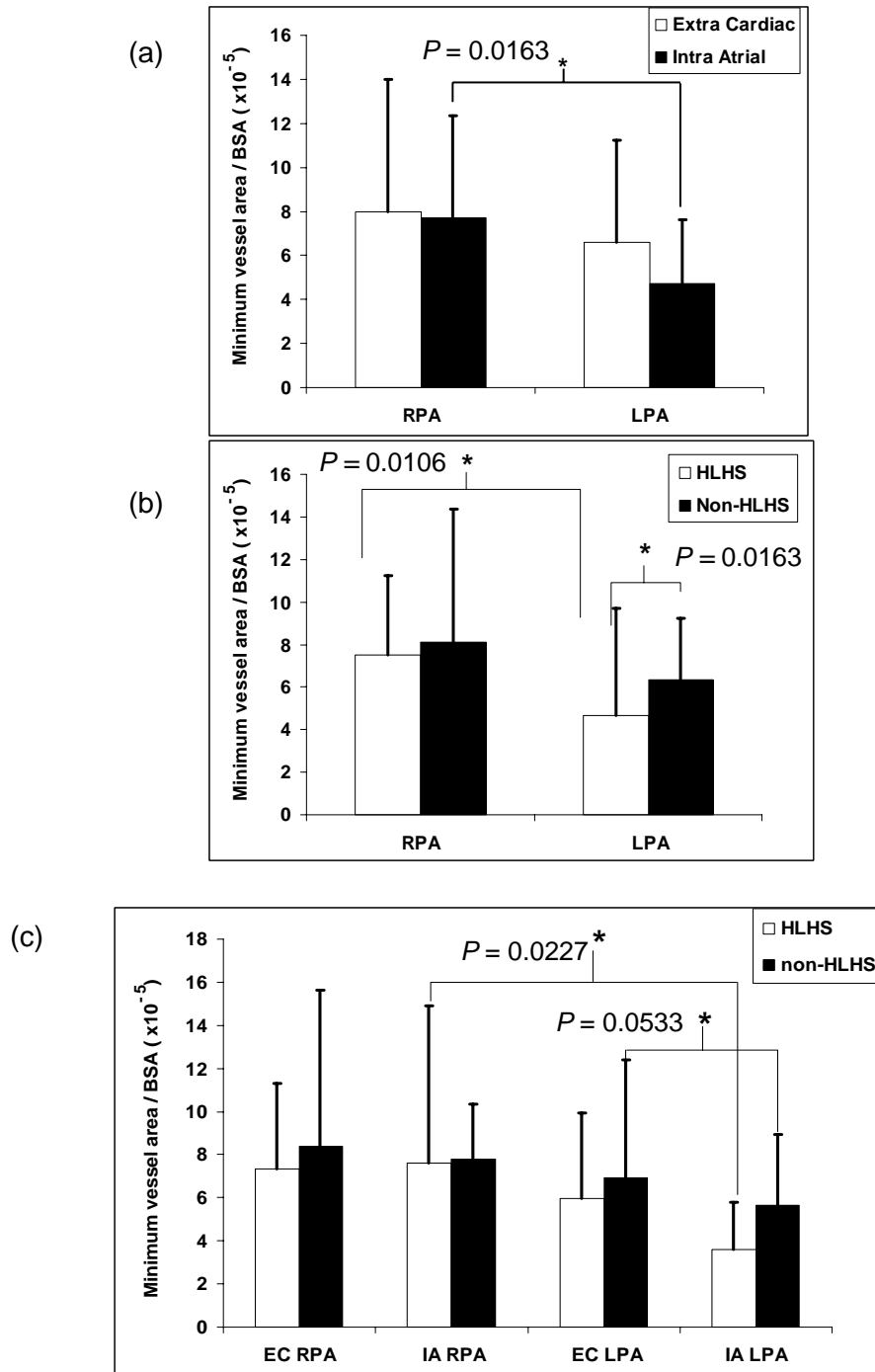
Figure 5.12: Minimum vessel area for the pulmonary arteries – LPA and RPA for population groups: (a) EC and IA (N=13 each) (b) HLHS (N=10) and non-HLHS (N=16), and (c) EC HLHS (N=4), EC non-HLHS (N=9), IA HLHS (N=6) and IA non-HLHS (N=7).

5.3.1.2 Vessel Orientation and Curvature:

Figures 5.13 and 5.14 show the results related to vessel curvature and orientation. Figure 5.13 compares the averaged vessel curvatures observed in the IA and EC connections. The RPA curvature for the EC group was found to have larger patient-to-patient variation. As depicted in Figure 5.14a, the IA collinearity was significantly smaller than EC collinearity (p = 0.0562). Since the second stage surgery of these patients can significantly influence collinearity, we compared the collinearity between hemi-Fontans and BDG and report that hemi-Fontans had significantly smaller collinearity (p = 0.0467; Figure 5.14b).
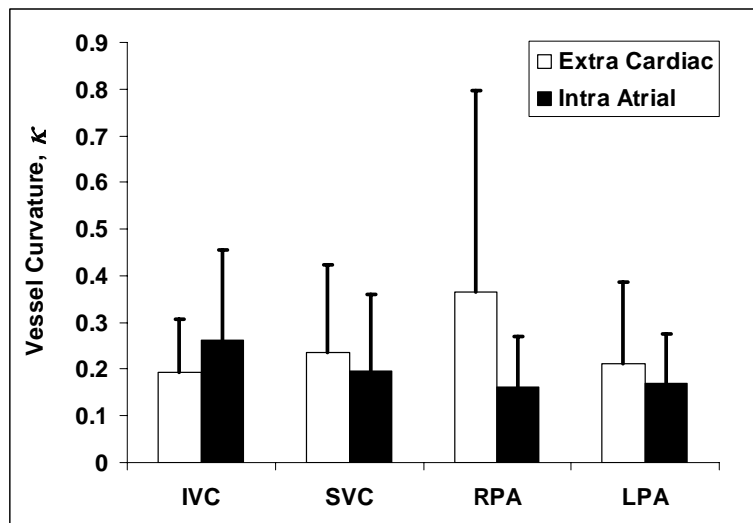
Figure 5.13: TCPC orientation depicted by mean vessel curvature between the EC and IA patient groups (N=13 each).

(a)   (b)
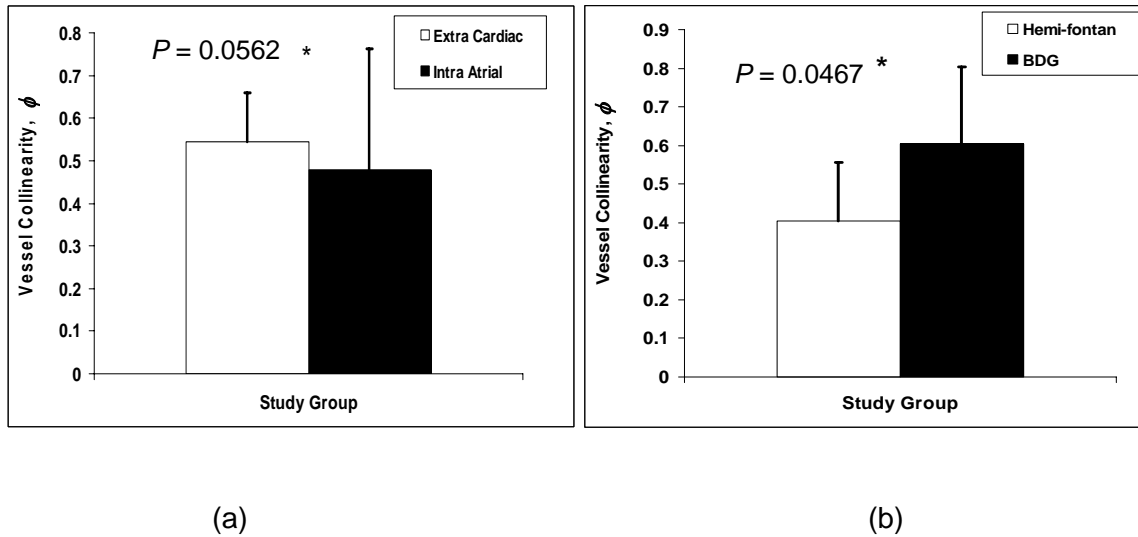
Figure 5.14: TCPC orientation depicted by (a) mean collinearity for EC and IA (N=13 each) (b) mean collinearity for hemi-Fontan (N =10) and BDG (N=16)

5.3.1.3 Vessel Offset:

Comparison between the three types of vessel offsets - (1) right-left (RL) offset between IVC and SVC, (2) anterior-posterior (AP) offset between IVC and SVC, and (3) PA-VC offset between pulmonary arteries and the venae cavae - showed no statistical significance. All the offset values are divided with square root of BSA, so as to provide proper normalization. Each of these results is shown independently in Figures 5.15, 5.16 and 5.17. Since these offsets largely depend on the second stage of the Fontan, the same comparison between Glenn and hemi Fontan is also provided in these figures. The PA-VC offset showed a smaller p value of 0.15 when the comparison was made between the second-stage Fontan i.e. hemi-Fontan and Glenn (Refer Table 5.1).
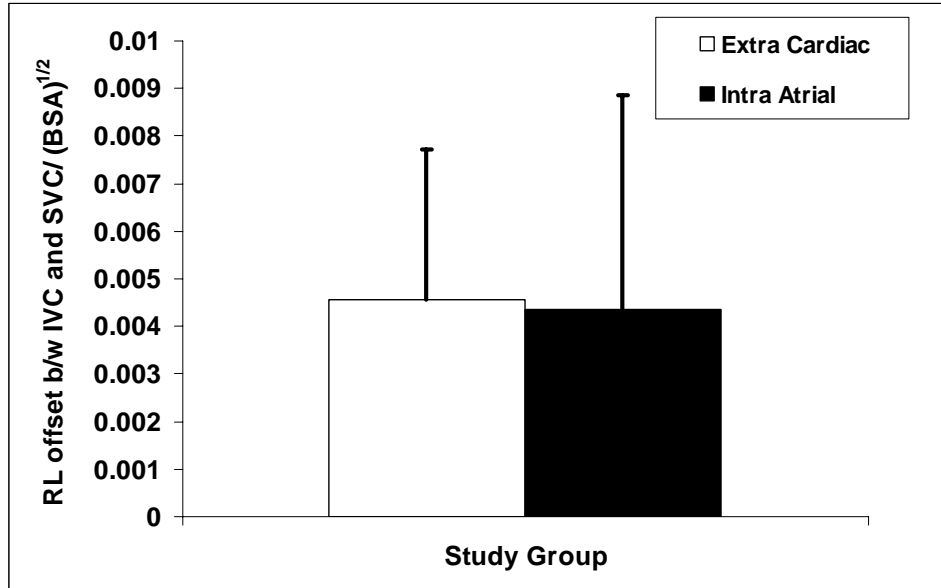
(a)
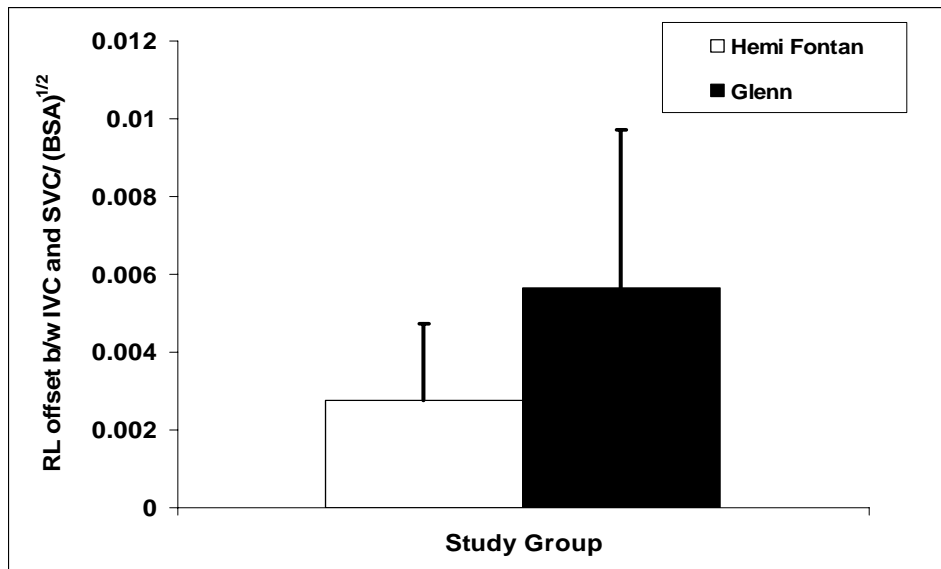
(b)

Figure 5.15: RL offset between the IVC and SVC of the TCPC for (a) EC and IA (N=13 each) (b) hemi-Fontan (N=10) and BDG (N=16)
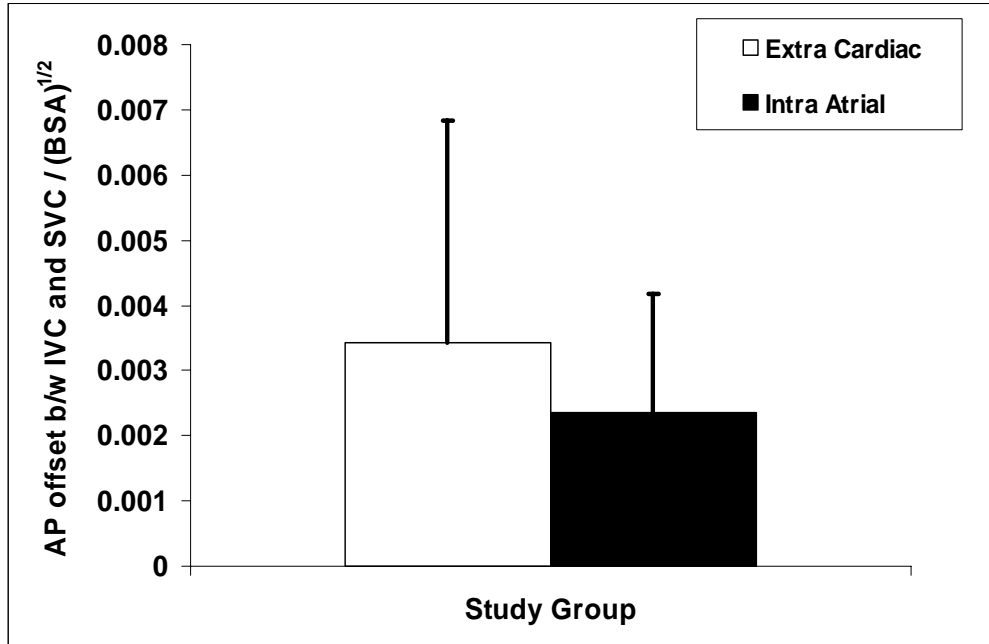
(a)
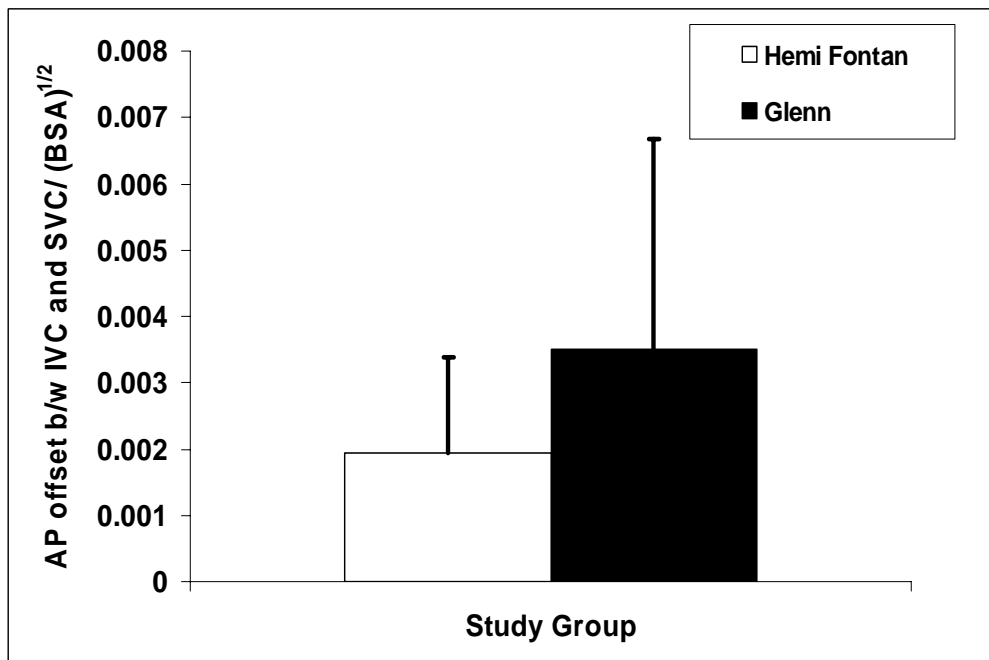
(b)

Figure 5.16: AP offset between the IVC and SVC of the TCPC for (a) EC and IA (N=13 each) (b) hemi-Fontan (N=10) and BDG (N=16)
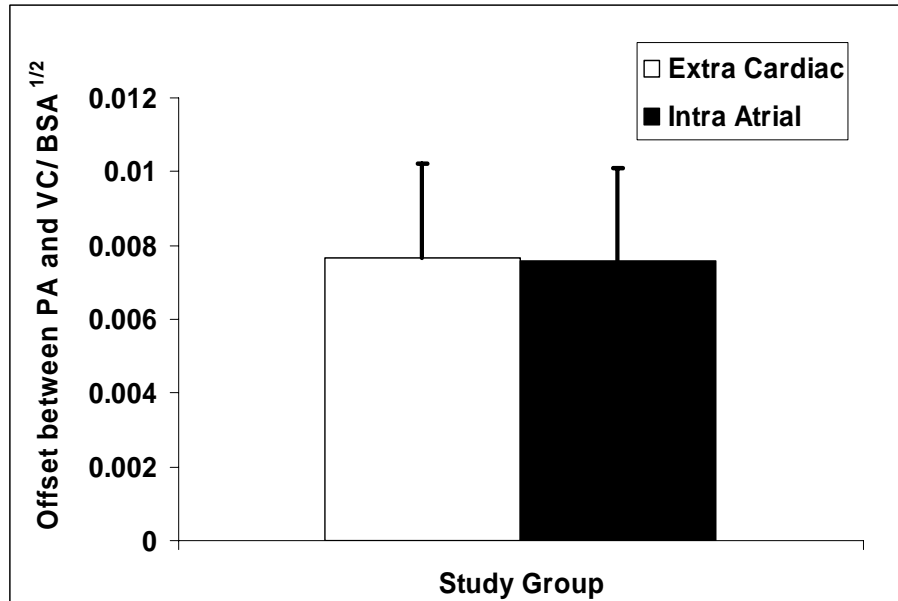
(a)
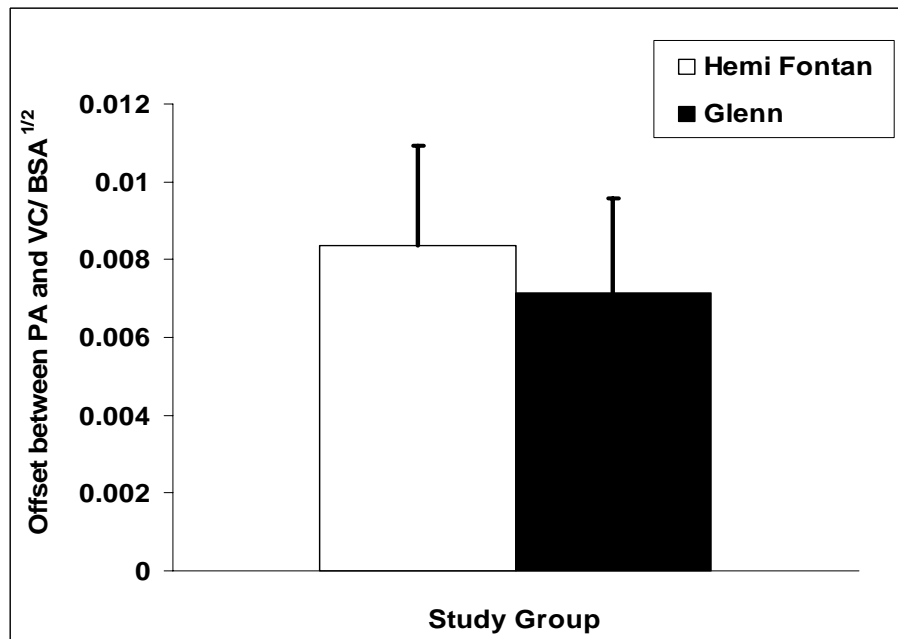
(b)

Figure 5.17: Offset between the venae cavae and pulmonary arteries TCPC for (a) EC and IA (N=13 each) (b) hemi-Fontan (N=10) and BDG (N=16)

5.3.2 Pre Fontan vs. Post Fontan

Geometric characteristics of three pairs of pre and post Fontan models are quantified in this section. Each computed parameter is averaged over the 3 models and its values before and after the 3rd stage surgery are compared. Since the sample size was three and one of the models was a bilateral SVC no statistical analysis could be performed on the data. In addition, since bilateral SVC has both RSVC and LSVC, RSVC is used for comparing with normal SVC of other models. The LSVC value is also plotted in all the graphs. The pre Fontan stage does not include an IVC, hence only the post-Fontan characteristics of the IVC are included in the analysis. A summary of the quantified parameters for the pre and post Fontan pairs is provided in Table 5.2.

Table5.2: Summary of the computed values of geometric characteristics for pre and post Fontan groups

Computed Variables	Pre Fontan	Post Fontan
Mean Vessel Cross-Sectional Area / BSA		
IVC	-	$5.61 \times 10^{-4} \pm 0.81 \times 10^{-4}$
SVC	$2.43 \times 10^{-4} \pm 1.46 \times 10^{-4}$	$1.73 \times 10^{-4} \pm 0.82 \times 10^{-4}$
LSVC	1.64×10^{-4}	1.53×10^{-4}
RPA	$2.25 \times 10^{-4} \pm 1.36 \times 10^{-4}$	$2.25 \times 10^{-4} \pm 0.43 \times 10^{-4}$
LPA	$1.95 \times 10^{-4} \pm 1.36 \times 10^{-4}$	$1.81 \times 10^{-4} \pm 0.41 \times 10^{-4}$
Vessel Cross-Sectional Area Ratio		
LPA/IVC	-	0.32 ± 0.06
LPA/SVC	0.90 ± 0.62	1.16 ± 0.42
LPA/LSVC	1.10	0.92
RPA/IVC	-	0.40 ± 0.04
RPA/SVC	1.05 ± 0.64	1.44 ± 0.49
RPA/RSVC	1.24	1.31
Vessel Area Standard deviation / BSA.		
IVC	-	$8.26 \times 10^{-5} \pm 6.64 \times 10^{-5}$
SVC	$2.26 \times 10^{-5} \pm 1.64 \times 10^{-5}$	$2.16 \times 10^{-5} \pm 1.71 \times 10^{-5}$
LSVC	1.76×10^{-5}	7.97×10^{-5}
RPA	$4.16 \times 10^{-5} \pm 2.99 \times 10^{-5}$	$4.58 \times 10^{-5} \pm 2.54 \times 10^{-5}$
LPA	$6.03 \times 10^{-5} \pm 1.36 \times 10^{-5}$	$4.56 \times 10^{-5} \pm 1.16 \times 10^{-5}$
Minimum Vessel Cross-Sectional Area / BSA		
RPA	$1.62 \times 10^{-4} \pm 1.02 \times 10^{-4}$	$1.51 \times 10^{-4} \pm 0.37 \times 10^{-4}$
LPA	$1.24 \times 10^{-4} \pm 1.16 \times 10^{-4}$	$1.22 \times 10^{-4} \pm 0.43 \times 10^{-4}$
Vessel Curvature at the TCPC junction		
IVC	-	0.10 ± 0.10
SVC	0.12 ± 0.09	0.06 ± 0.03
LSVC	0.03	0.01
RPA	0.26 ± 0.15	0.38 ± 0.56
LPA	0.21 ± 0.08	0.27 ± 0.27
PA-VC Offset / BSA$^{1/2}$	$4.88 \times 10^{-3} \pm 2.63 \times 10^{-3}$	$7.12 \times 10^{-3} \pm 4.12 \times 10^{-3}$

Four parameters of the TCPC geometry are quantified in this section. These include vessel cross sectional areas, area standard deviations, ratios of the LPA and RPA cross-sectional areas over the IVC and SVC areas, and minimum PA areas. Counter intuitively, the SVC and LPA cross-sectional areas averaged over the entire vessel length were slightly less after the surgery than before (Figure 5.18). Investigating whether this could be attributed to the appearance of new LPA stenosis, minimum vessel cross-sectional areas were compared but no difference was observed between the pre and post values (Figure 5.19). In order to quantify the area variation across the vessel length, the standard deviation of the cross sectional area is plotted for each of the vessels in the vicinity of the TCPC, revealing higher variations in LPA cross-sectional area before the surgery than after (Figure 5.20).
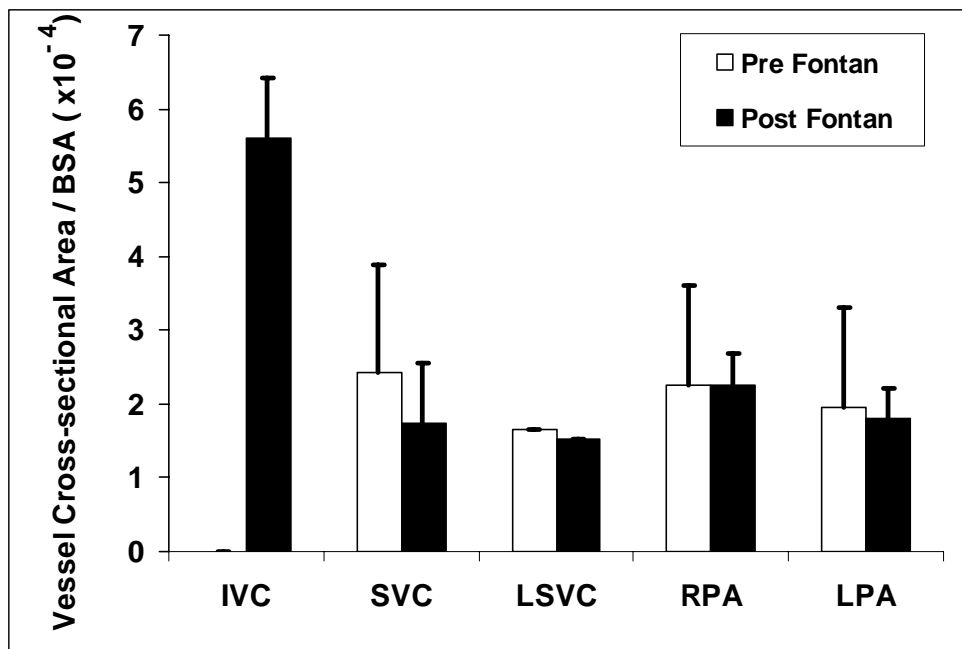
Figure 5.18: Mean vessel cross sectional area depicted for pre and post Fontan geometries (N=3 each)
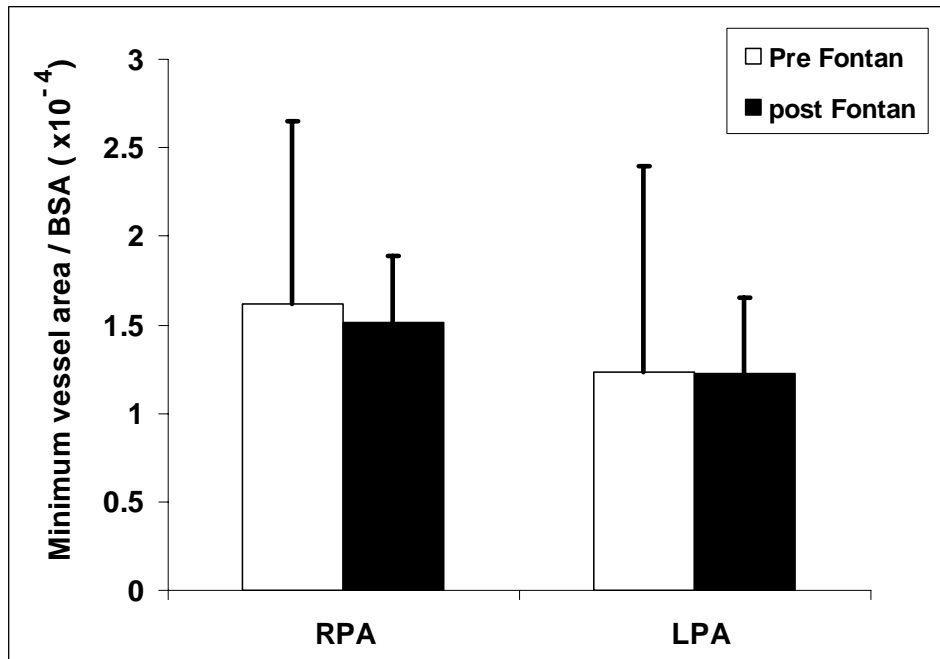
Figure 5.19: Minimum vessel areas of the pulmonary arteries depicted for pre and post Fontan geometries (N=3 each)
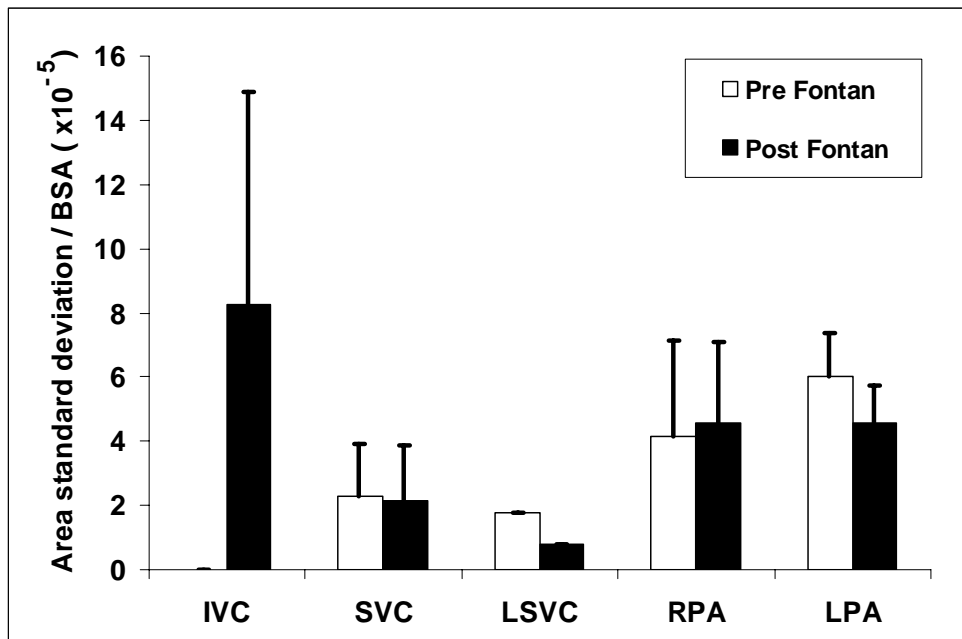
Figure 5.20: Area standard deviation of the TCPC vessels depicted for pre and post Fontan geometries (N=3 each)

5.3.2.2 Vessel Curvature:

Figure 5.21 shows the vessel curvature at the junction of the TCPC for all the connecting vessels for the pre and post Fontan pairs. Curvature of both the PAs showed smaller values before the surgery. Also the RPA curvature for the post Fontan group was found to have larger patient-to-patient variation. Curvature of the SVC was slightly higher for the pre-Fontan group than for the post-Fontan geometry.

5.3.2.3 Vessel Offset Characteristics:

Since pre-Fontan connections do not include the IVC, the AP, RL and PA-VC offsets were not computed on 2nd stage anatomies.
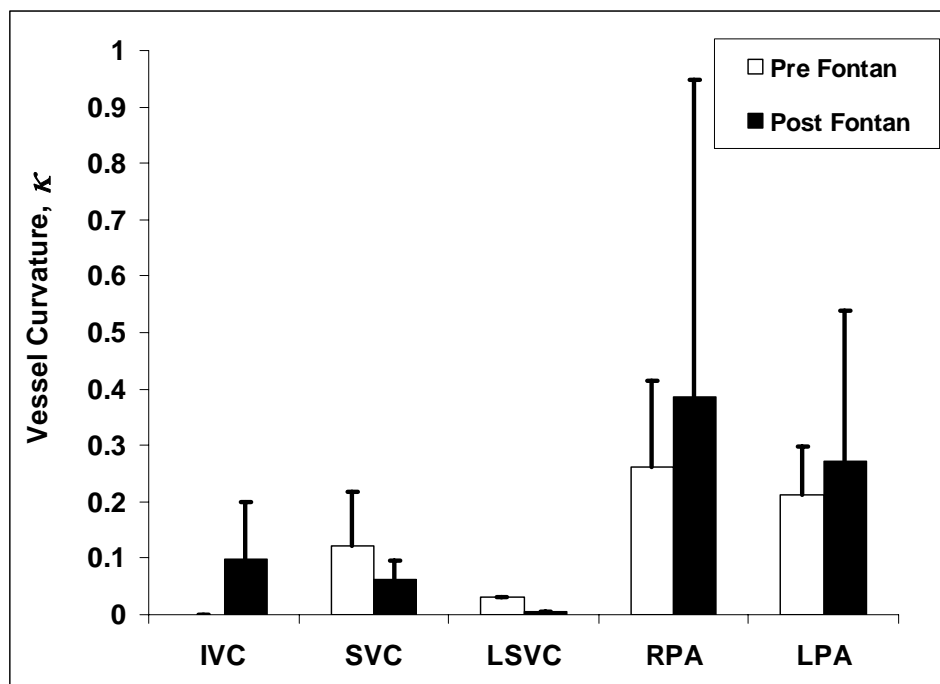
Figure 5.21: Vessel curvature depicted for pre and post Fontan groups for all the vessels in the vicinity of the connection (N=3)

5.3.3 Bilateral SVC TCPC models

Bilateral SVC models are a special category of Fontan patients with two SVCs named as right SVC (RSVC) and left SVC (LSVC) as shown in Figure 5.6. This section quantifies the geometric features of five bilateral SVC models. The results of calculated parameters for all the models are presented in tabulated format for each category.

5.3.3.1 Vessel Area Characteristics:

Mean vessel cross-sectional area, area standard deviation and the minimum vessel area for the PAs are computed in this analysis (Table 5.3). To see how the vessel dimensions of bilateral SVCs compared to that of common Fontan geometries, the mean vessel cross sectional area of all the vessels, except the LSVC, of bi-lateral SVCs where compared to that of EC TCPC (Figure 5.22). The reason to choose EC TCPC is because, all the five bi-lateral SVCs have extra cardiac TCPC.

There was no significant difference between the cross sectional areas of RSVC and LSVC (Figure 5.23). Also sum of RSVC and LSVC of the bi-lateral SVCs are used for comparing with the SVC of normal Fontans. However, the vessel area standard deviation across the vessel length for the LSVC is almost double that of the RSVC (Figure 5.24).

Table 5.3: Vessel area characteristics computed for the 5 bilateral SVC models along with their mean values.

Computed Variables	Bilateral SVC					
	CHOA039	CHOP019	CHOP022	CHOP032	CHOP055	Mean
Mean Vessel Area / BSA						
IVC	4.08×10^{-4}	1.96×10^{-4}	1.20×10^{-4}	2.58×10^{-4}	4.79×10^{-4}	2.92×10^{-4}
RSVC	1.8×10^{-4}	0.69×10^{-4}	0.61×10^{-4}	0.62×10^{-4}	1.00×10^{-4}	0.95×10^{-4}
LSVC	1.5×10^{-4}	0.46×10^{-4}	1.02×10^{-4}	0.75×10^{-4}	1.53×10^{-4}	1.07×10^{-4}
RPA	1.61×10^{-4}	0.69×10^{-4}	1.0×10^{-4}	0.73×10^{-4}	2.00×10^{-4}	1.21×10^{-4}
LPA	2.34×10^{-4}	0.75×10^{-4}	0.69×10^{-4}	1.08×10^{-4}	1.41×10^{-4}	1.27×10^{-4}
Vessel Area Stdev./ BSA						
IVC	11.06×10^{-5}	1.05×10^{-5}	1.24×10^{-5}	6.82×10^{-5}	4.64×10^{-5}	4.96×10^{-5}
SVC	1.85×10^{-5}	1.64×10^{-5}	7.81×10^{-5}	6.75×10^{-5}	9.82×10^{-5}	1.19×10^{-5}
LSVC	2.46×10^{-5}	1.34×10^{-5}	6.93×10^{-5}	8.16×10^{-5}	7.97×10^{-5}	2.47×10^{-5}
RPA	3.23×10^{-5}	1.57×10^{-5}	3.206×10^{-5}	1.60×10^{-5}	4.02×10^{-5}	2.73×10^{-5}
LPA	8.19×10^{-5}	1.92×10^{-5}	6.34×10^{-5}	3.5×10^{-5}	4.73×10^{-5}	3.79×10^{-5}
Min. Vessel Area / BSA						
RPA	9.45×10^{-5}	4.19×10^{-5}	4.89×10^{-5}	4.95×10^{-5}	12.1×10^{-5}	7.11×10^{-5}
LPA	6.88×10^{-5}	4.42×10^{-5}	5.49×10^{-5}	6.11×10^{-5}	8.19×10^{-5}	6.22×10^{-5}
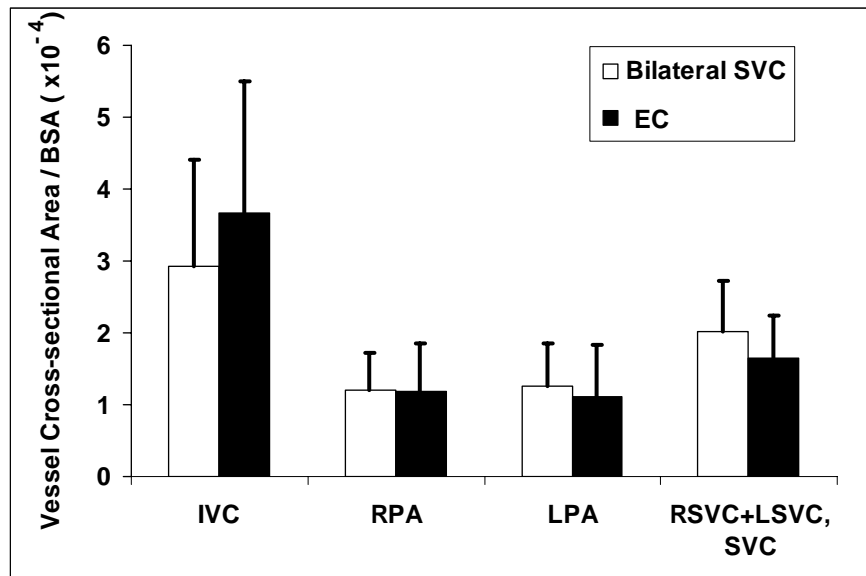
Figure 5.22: Mean vessel cross sectional area of bilateral SVC (N=5) compared to that of EC Fontan (N=13). Note that the sum of RSVC and LSVC of the bi-lateral Fontans are used to compare to the SVC of EC Fontan
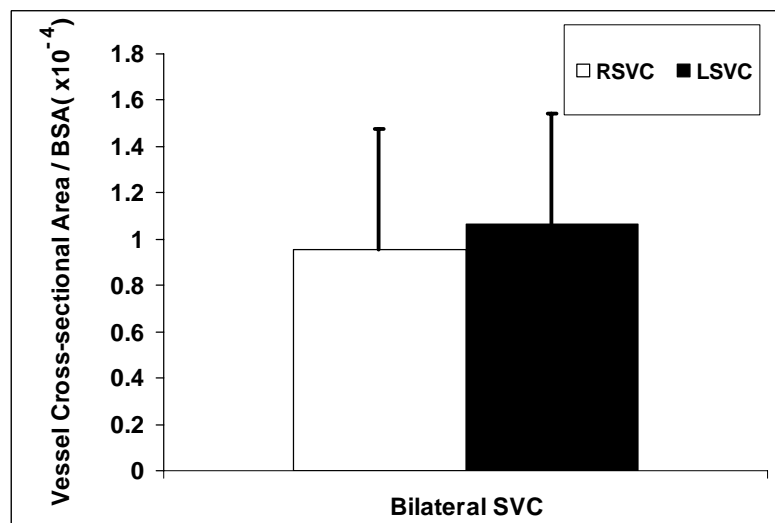
Figure 5.23: Mean vessel cross sectional area of the left and right SVC of bi-lateral SVC Fontans (N=5)
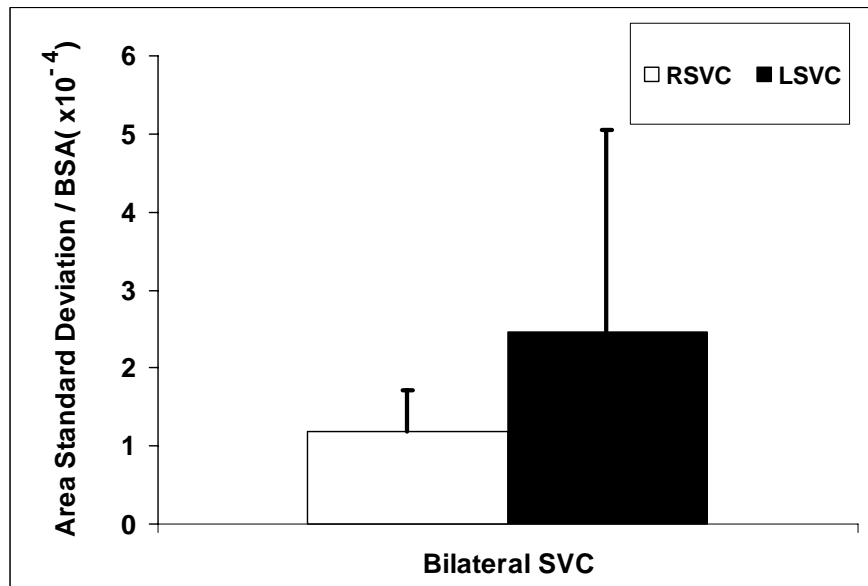
Figure 5.24: Vessel area standard of the left and right SVC of bi-lateral SVC Fontans (N=5). Area variation of LSVC is almost twice as compared to RSVC.

5.3.3.2 Vessel Curvature:

Curvature of all the vessels for the five bilateral SVC models is shown in table 5.4. No comparison between the curvature of the EC Fontans and bi-lateral SVCs could be made case because the SVCs of the bi-lateral Fontans are connected to the PAs directly in certain geometries (CHOP019 and CHOA039 of Figure 5.6).

5.3.3.3 Vessel Offset Characteristics:

Offset between the PA and VC is computed for all the five bilateral SVCs are shown in Table 5.5.

Table 5.4: Vessel curvature computed for the 5 bilateral SVC models

Vessels analyzed	CHOA039	CHOP019	CHOP022	CHOP032	CHOP055
IVC	0.13	0.23	0.18	0.04	0.21
RSVC	0.17	0.23	1.94	0.34	0.09
LSVC	0.03	0.27	0.60	0.46	0.006
RPA	0.13	0.23	0.58	0.62	0.13
LPA	0.72	0.12	0.38	0.21	0.57

Table 5.5: PA-VC offset computed for the 5 bilateral SVC models

Bilateral SVC Models	PA-VC Offset / BSA$^{1/2}$
CHOA039	7.54×10^{-3}
CHOP019	5.32×10^{-3}
CHOP022	9.81×10^{-3}
CHOP032	4.73×10^{-3}
CHOP055	3.31×10^{-3}

5.4 Anatomy vs. Hemodynamic correlates of the TCPC – Aim 3

Some of the geometric parameters computed using the skeletonization method might be correlated with the TCPC hemodynamics, mainly the TCPC power loss, Cardiac Index and the ventricular power output. This correlation between the TCPC geometry and the hemodynamic parameters are explained in this section of the chapter.

Previous experimental and numerical studies have all underscored the tight relationship between the TCPC design and its efficiency [Pekkan, 2005; De Zelicourt, 2005]. Though these studies have led to some suppositions as to what features could play an important role in dictating the overall connection efficiency of TCPC, no study has yet been able to correlate TCPC hemodynamics to simple geometric parameters.

The skeletonization approach, developed in this study is a strong tool that can be used to demonstrate such correlation. Accordingly, this last section of the Chapter seeks to take advantage of the geometric features analyzed in the previous sections and correlate them with the following hemodynamic parameters: experimental and CFD control volume power losses, cardiac index and ventricular power output.

5.4.1 TCPC Geometry and Experimental Power Loss

Figure 5.25 depicts the non dimensionalized *in-vitro* power loss ($\dot{E}_{loss}/E_0$) for six patients, as a function of the minimum vessel sizes normalized with the BSA at 50-50 pulmonary flow split at MRI cardiac outputs. From Figure 5.25, the relationship between power losses within the TCPC and minimum LPA cross-sectional area appears to be the most coherent. Power loss is found to scale as a power law with respect to the minimum LPA area with an R^2 of 0.96 (Figure 5.25c). The R^2 values with respect to IVC, SVC, and RPA vessel characteristics were not significant.

To further investigate the effect of minimum vessel cross-sectional area on power loss, non-dimensionalized *in-vitro* power loss ($\dot{E}_{loss}/E_0$) at equal pulmonary resistance (refer appendix D for the details about computing the equal pulmonary resistance) and at MRI flow split condition (both calculated at MRI cardiac output) are also plotted on Figures 5.26 and 5.27, respectively. However, the R2 values are not significant for the minimum LPA area (and all other vessels) in these plots. Table 5.6 summarizes the power-losses computed at 50-50 pulmonary flow split, MRI flow split and equal pulmonary resistance conditions for experimental condition. The non-dimensionalized power loss values along with the normalized minimum vessel areas are provided in Appendix B.
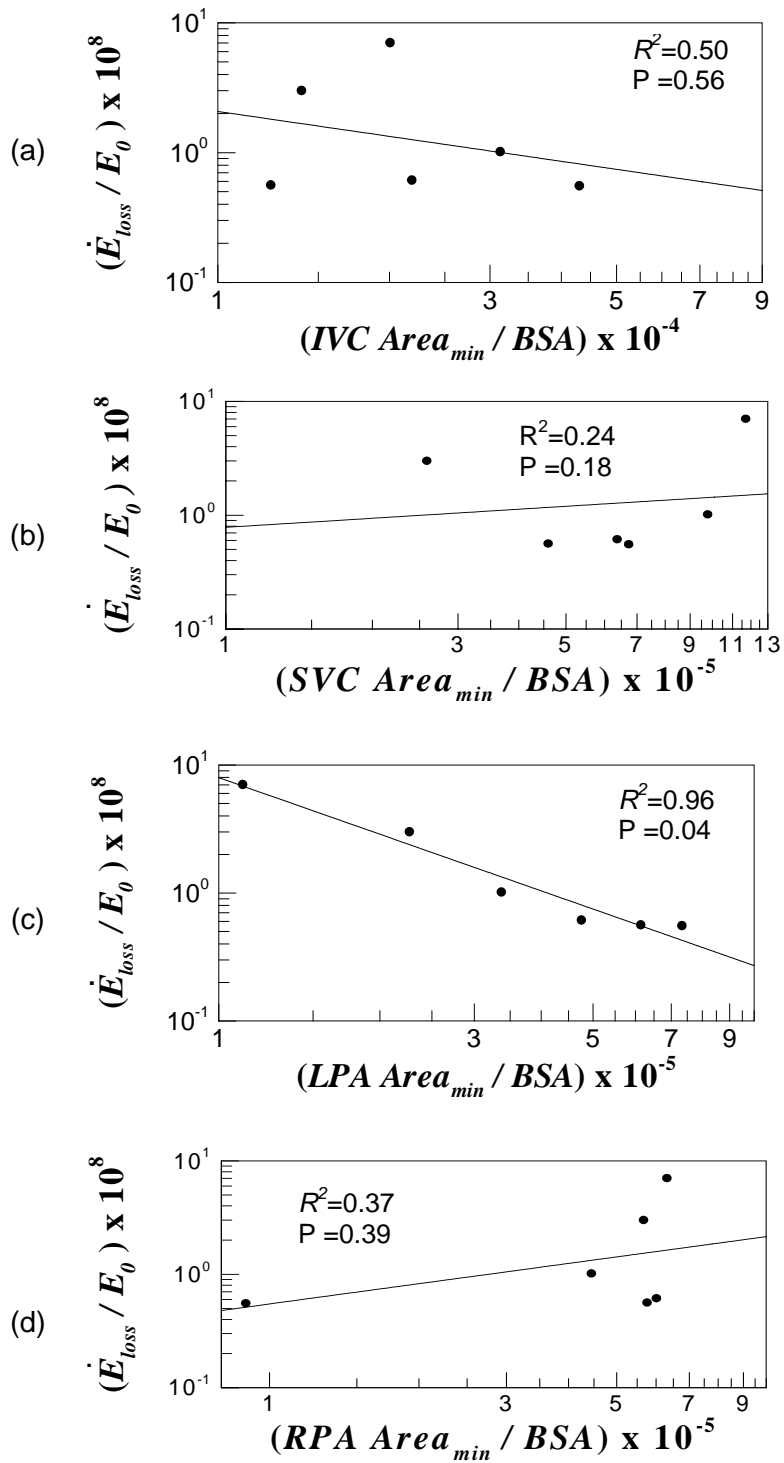
Figure 5.25: Non-dimensionalized experimental power loss ($\dot{E}_{loss}/E_0$) at 50-50 pulmonary flow split and at MRI cardiac outputs for six TCPC geometries plotted against the minimum vessel cross-sectional area of: (a) IVC and (b) SVC (c) LPA and (d) RPA. The highest correlation is observed with minimum LPA area.
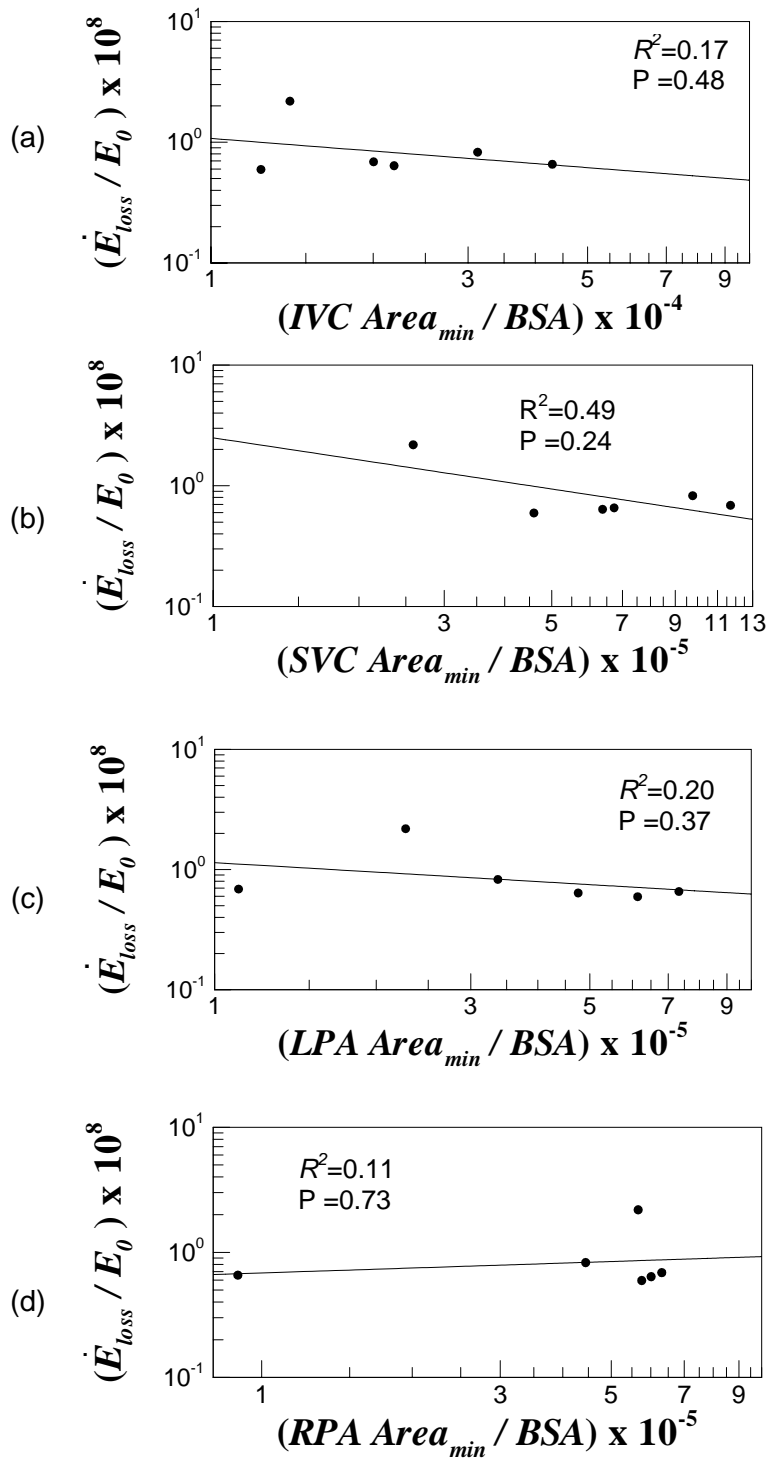
Figure 5.26: Non-dimensionalized experimental power loss ($\dot{E}_{loss}/E_0$) at equal pulmonary resistance flow split and at MRI cardiac outputs for six TCPC geometries plotted against the minimum vessel cross-sectional area of: (a) IVC and (b) SVC (c) LPA and (d) RPA.
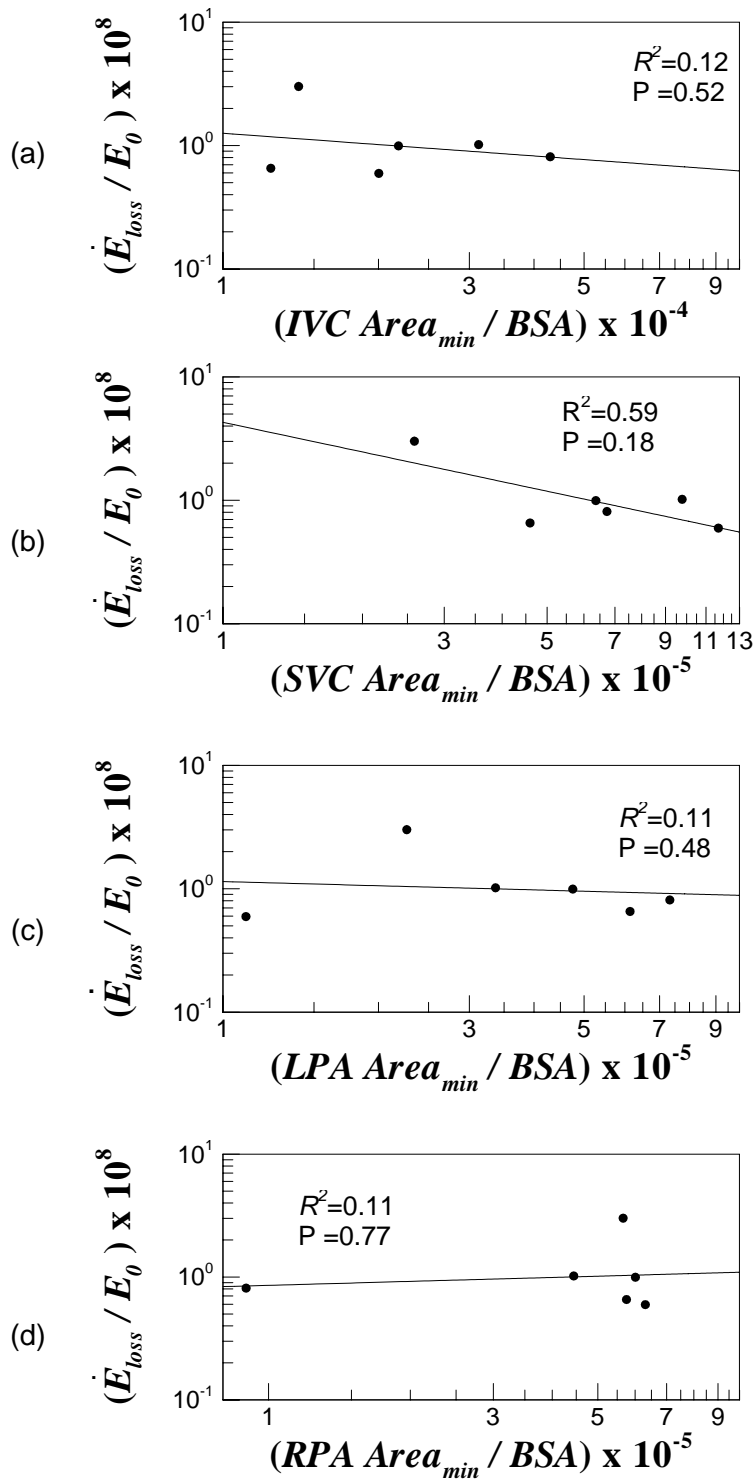
Figure 5.27: Non-dimensionalized experimental power loss ($\dot{E}_{loss}/E_0$) at MRI flow split condition and at MRI cardiac outputs for six TCPC geometries plotted against the minimum vessel cross-sectional area of: (a) IVC and (b) SVC (c) LPA and (d) RPA.

104

Table 5.6: Summary of experimental power loss (PL) values computed at MRI cardiac output for the flow conditions – 50-50 pulmonary artery flow split, MRI flow condition and at equal pulmonary resistance (eq.PR)

Model	PL at 50% flow split (mW)	PL at MRI flow split (mW)	PL at eq.PR (mW)
CHOA007	19.03	19.03	13.80
CHOA008	4.60	6.72	5.44
CHOP013	135.99	11.50	8.65
CHOA009	11.94	11.94	9.70
CHOA011	13.26	21.42	13.76
CHOP034	12.56	14.59	13.24

5.4.2 TCPC Geometry and CFD Power Loss

Power losses computed using CFD simulations for nine patients are also plotted against the minimum vessel diameters to see the strength of the correlation. Figures 5.28, 5.29 and 5.30 shows these plots for non-dimensionalized CFD power losses ($\dot{E}_{loss}/E_0$) computed at the flow conditions: 50-50 pulmonary artery flow split, MRI flow condition and at equal pulmonary resistance (eq.PR), respectively. Refer table 5.7 for the summary of the computed power loss values.

These power losses are computed at MRI flow conditions using PCMRI data and are plotted against minimum vessel cross-sectional areas of IVC, SVC, LPA and RPA similar to section 5.4.1. However, with the CFD power loss it is the RPA that shows more correlation than that of LPA. This means that it the minimum vessel area of the outlet vessels, i.e. the pulmonary arteries have highest correlation with the TCPC power loss.
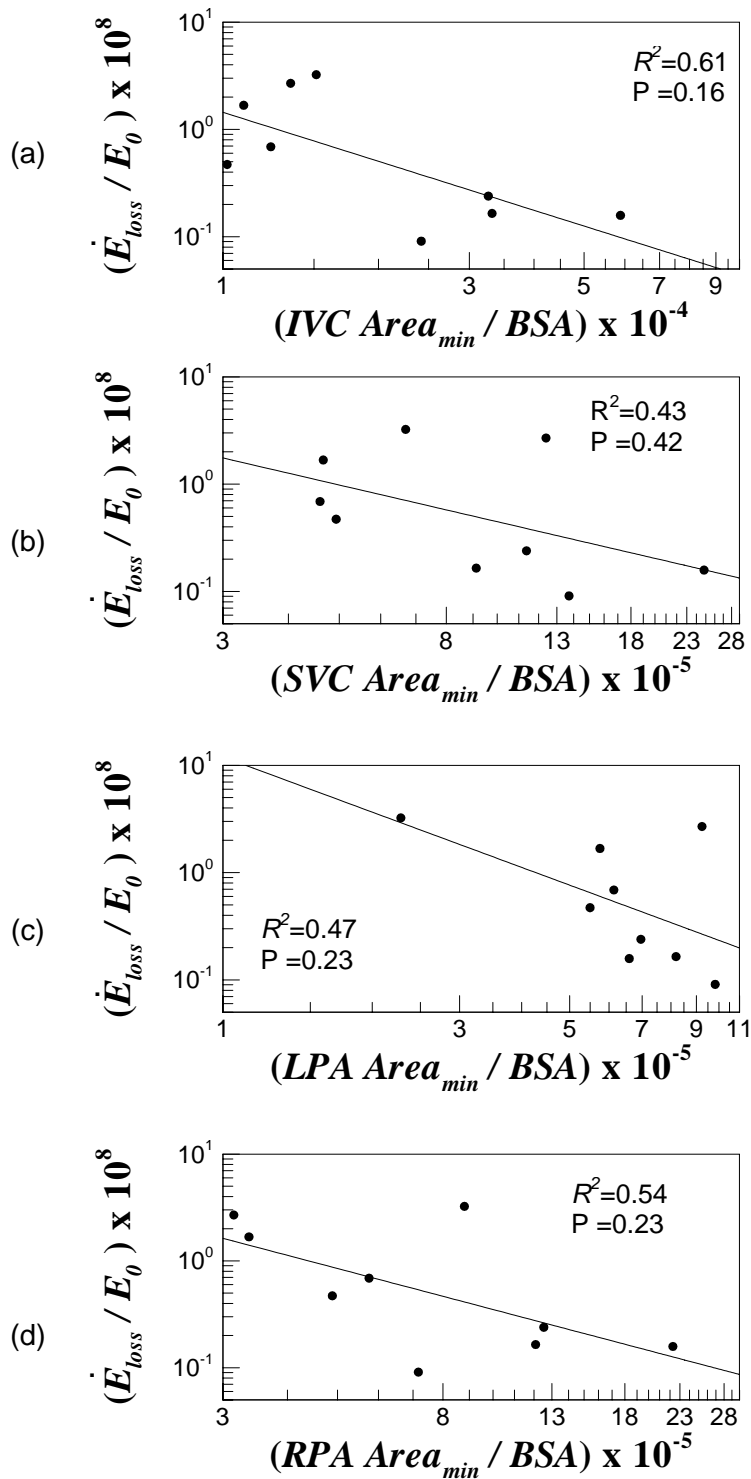
Figure 5.28: Non-dimensionalized CFD power loss ($\dot{E}_{loss}/E_0$) at 50-50 pulmonary flow split condition and at MRI cardiac outputs for nine TCPC geometries plotted against the minimum vessel cross-sectional area of: (a) IVC and (b) SVC (c) LPA and (d) RPA.
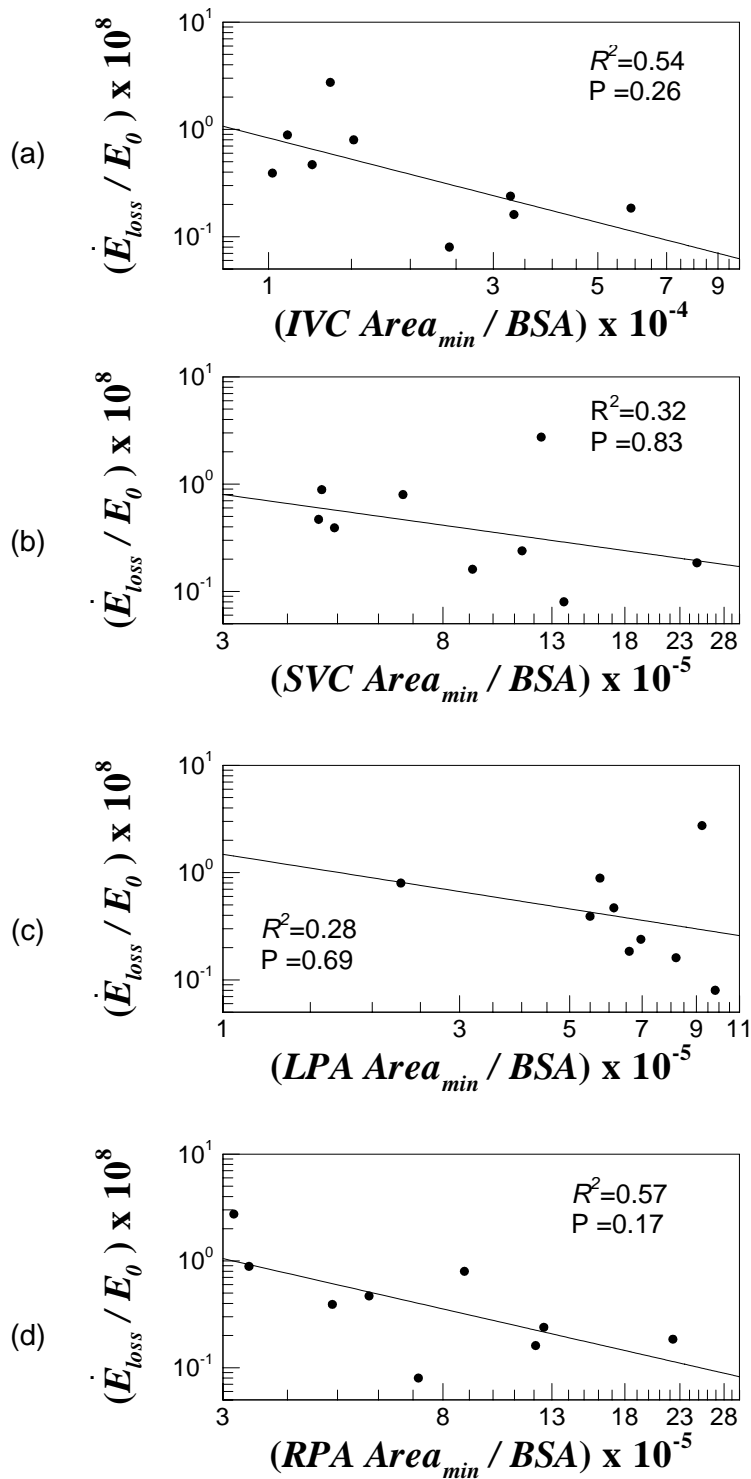
Figure 5.29: Non-dimensionalized CFD power loss ($\dot{E}_{loss}/E_0$) calculated at equal pulmonary flow split condition and at MRI cardiac outputs for nine TCPC geometries plotted against the minimum vessel cross-sectional area of: (a) IVC and (b) SVC (c) LPA and (d) RPA.
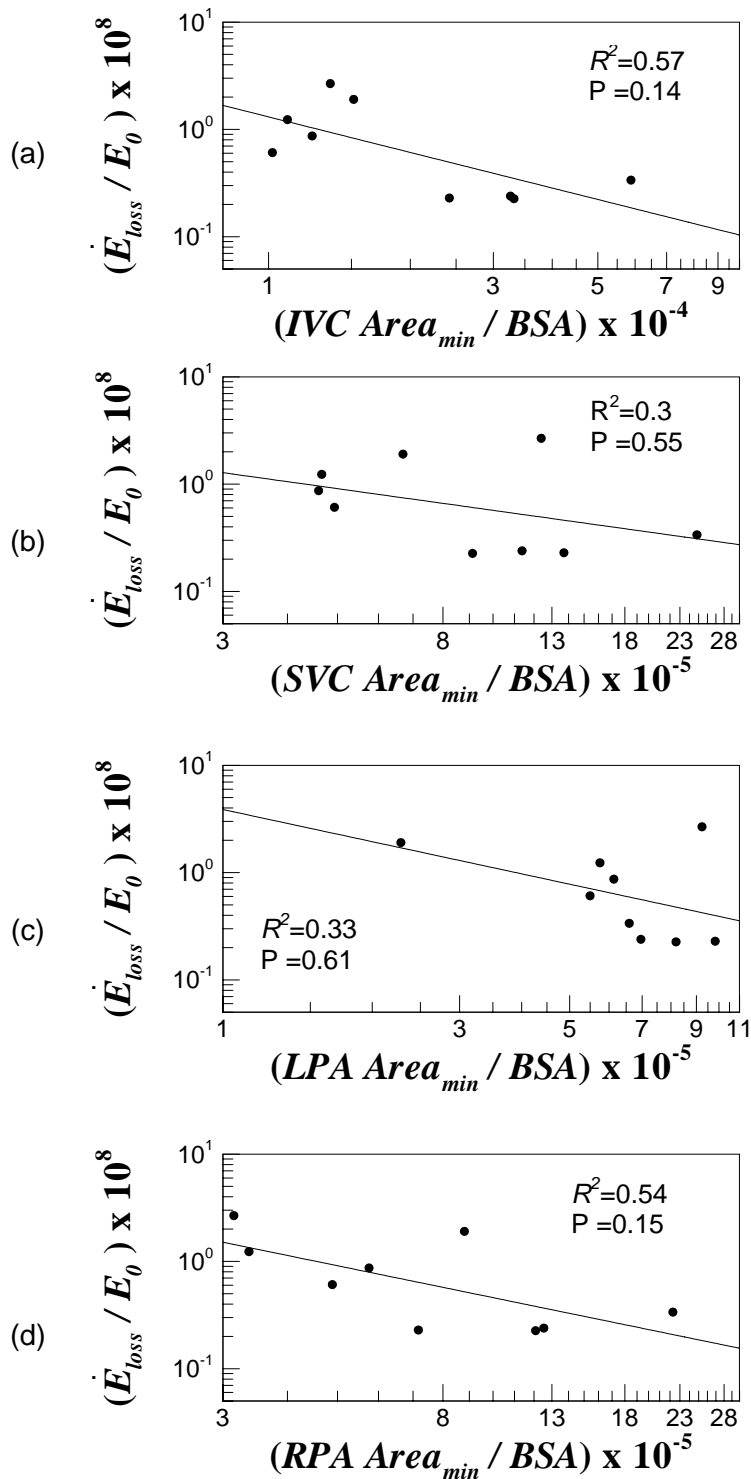
Figure 5.30: Non-dimensionalized CFD power loss ($\dot{E}_{loss}/E_0$) calculated at MRI flow split condition and at MRI cardiac outputs for nine TCPC geometries plotted against the minimum vessel cross-sectional area of: (a) IVC and (b) SVC (c) LPA and (d) RPA.

Table 5.7: Summary of CFD power loss (PL) values computed at MRI cardiac output for the flow conditions – 50-50 pulmonary artery flow split, MRI flow condition and at equal pulmonary resistance (eq.PR)

Model	PL at 50% flow split (mW)	PL at MRI flow split (mW)	PL at eq. PR (mW)
CHOP018	31.56	18.56	7.79
CHOP022	5.83	7.53	4.85
CHOP034	34.53	43.57	23.51
CHOP037	25.61	18.83	13.56
CHOP055	0.68	0.94	0.67
CHOP067	61.87	61.53	63.12
CHOP088	0.83	1.77	0.97
CHOP089	2.84	2.84	2.84
CHOP090	1.37	3.47	1.21

The non-dimensionalized power loss values along with the normalized minimum vessel areas are provided in Appendix B.

5.4.3 TCPC Geometry and Cardiac Index

Figure 5.31 depicts the impact of TCPC geometry on the patient's cardiac output (CO) by showing both the *in-vitro* power loss data and CFD power loss data at MRI conditions plotted against the *in-vivo* cardiac indices obtained from the clinical information. As shown in Figure 5.31a, a significant association between the patients' cardiac index and the experimental power loss was observed with an R^2 value of 0.84. However, there was no statistically significant association between the *in-vivo* cardiac index and the *CFD* power loss. Power loss plots at equal pulmonary resistance are also

given in Figure 5.32. The results show similar trend as that of the MRI condition with no significant correlation seen for CFD simulations.
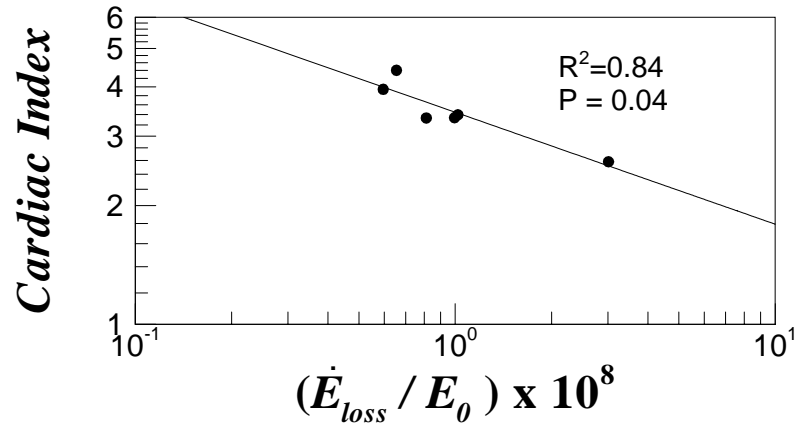
(a) CI vs. Experimental power loss at MRI flow split
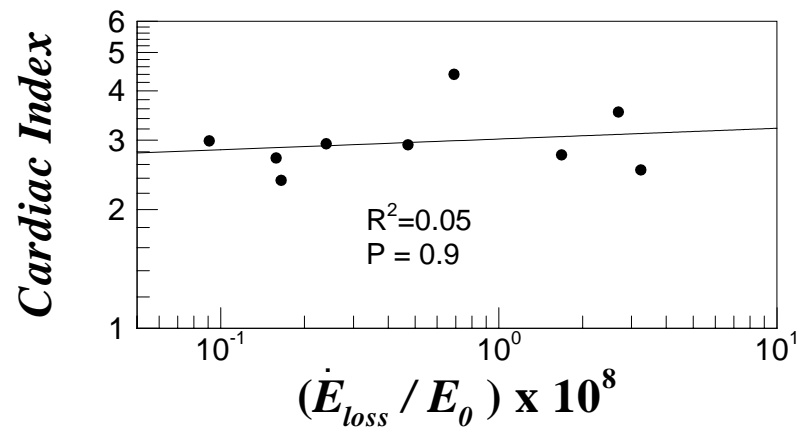
(b) CI vs. CFD power loss at MRI flow split

Figure 5.31: Cardiac index plotted against (a) normalized *in-vitro* power loss ($\dot{E}_{loss}/E_0$) and (b) normalized CFD power loss ($\dot{E}_{loss}/E_0$) at MRI flow split condition.
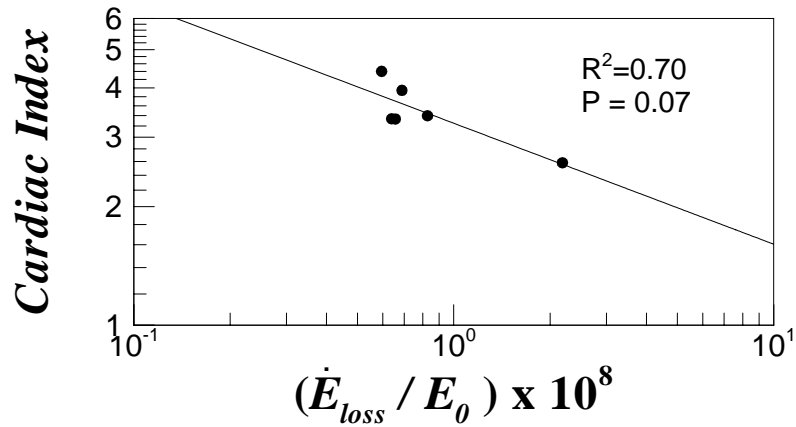
(a) CI vs. Experimental power loss at eq. PR
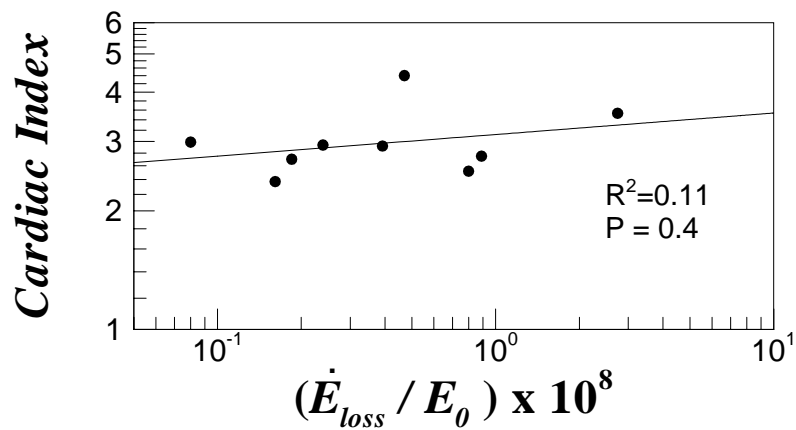
(b) CI vs. CFD power loss at eq. PR

Figure 5.32: Cardiac index plotted against (a) normalized *in-vitro* power loss ($\dot{E}_{loss}/E_0$), and (b) normalized CFD power loss ($\dot{E}_{loss}/E_0$) at equal pulmonary resistance flow split condition.

Since we have previously shown that the normalized minimum LPA cross-sectional area correlated with increased experimental power loss, cardiac index and power losses were plotted together testing if they could be correlated as well. It can be seen from Figure 5.33, that cardiac index drops when the vessel area of LPA decreases, however there was no statistical significance.
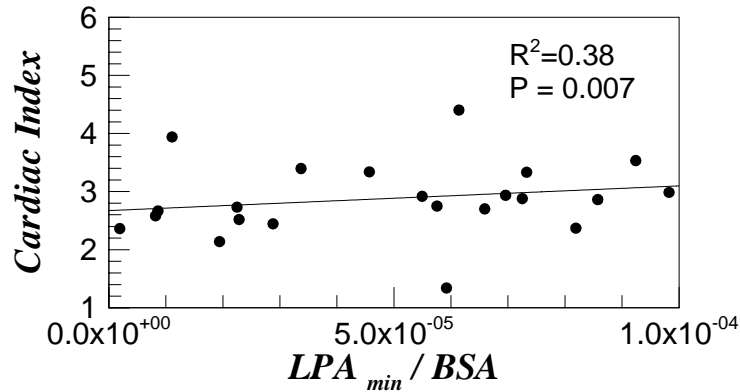
Figure 5.33: Cardiac index plotted against normalized LPA minimum area for all 26 patients

5.4.4 Ventricular Power Output

The circulatory power (or available mechanical energy) in the ascending aorta normalized by E_0 is a measure of ventricular power output ($\dot{E}$) relative to the patient's TCPC power loss. Regression between this quantity, $\dot{E}/E_0$ (normalized ventricular power output), and the normalized minimum LPA cross-sectional area (N=13) also showed a negative correlation (P = 0.04) as shown in Figure 5.34. Figure 5.35a shows the statistical comparison of the ventricular power output between the EC and IA patients. The two populations had a statistically significant difference (p = 0.0336), with the ventricular power output relative to the TCPC power loss being higher for the IA population than for the EC population. Also note that the standard deviation among the IA population is higher. When comparing the same data between HLHS and non-HLHS patient groups there was no statistical significance (p = 0.4715) as seen in figure 5.35b. However a higher standard deviation in ventricular power output relative to the TCPC power loss was seen in HLHS patients as compared to non-HLHS patients. Figure 5.35c

shows that among the HLHS patients, IA patients are associated with higher ventricular

power output ($p = 0.0558$) and relatively higher patient-to-patient variability.
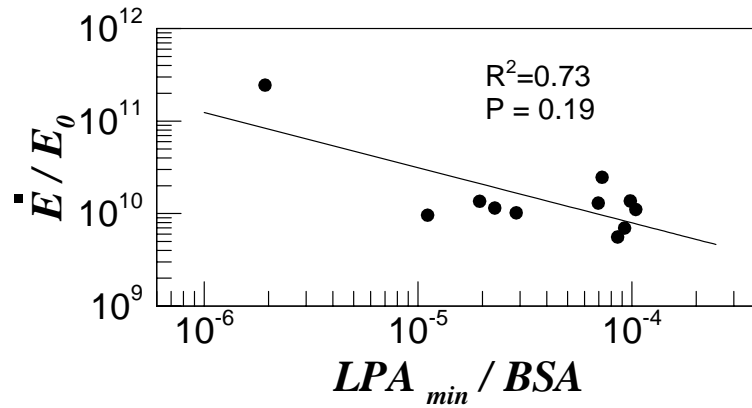
Figure 5.34: Normalized Ventricular power output ($\dot{E}/E_0$) plotted against minimum LPA area for 13 of the 26 patients, whose PCMRI data for the ascending aorta were available.
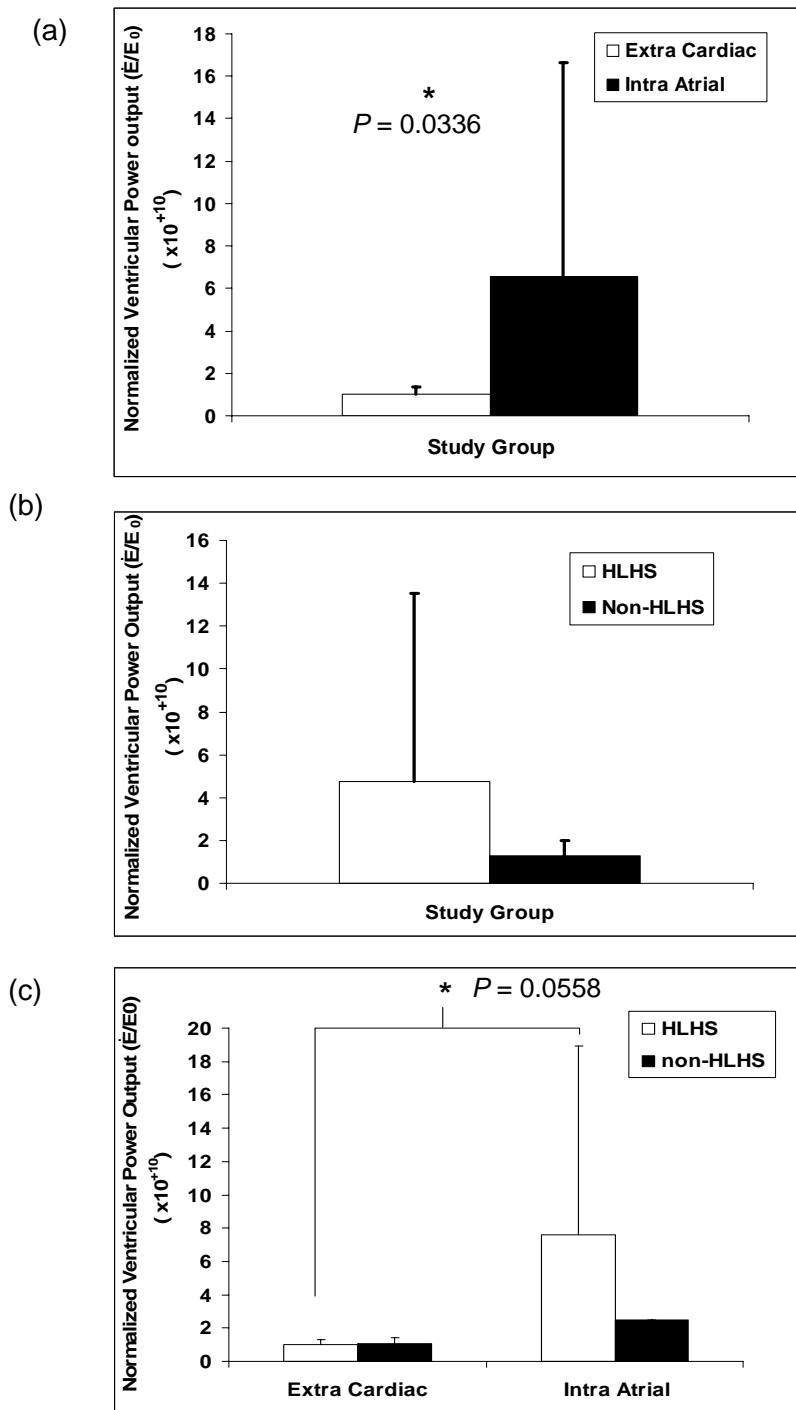
Figure 5.35: Power in the ascending aorta normalized with the TCPC dissipation scale, $\dot{E}/\varepsilon_0$ compared between (a) EC (N=8) and IA (N=5) and (b) HLHS (N=6) and non-HLHS group (N=7) (c) EC - HLHS (N=2), IA - HLHS (N=4), EC - non-HLHS (N=6) and IA - non-HLHS (N=1)

CHAPTER 6

DISCUSSION

6.1 Overview

Literature reviews show that, so far there exists no quantification of the geometric characteristics of the complex Fontan geometries. This motivated us to design the present study, whose main objectives were i) to develop a methodology to obtain the skeletalized representation of the TCPC ii) utilize this method to obtain the geometric characteristics of the Fontan models iii) correlate the Fontan geometries with their hemodynamics.

As detailed in the previous chapters, we have developed a method to obtain the centerline approximations of the complex TCPC anatomies. This method was used to obtain the geometrical characteristics associated with the TCPC models. Quantifying the geometrical parameters of Fontan anatomies are useful to get a better insight of the geometrical characteristics of different Fontan templates. This information will come in handy for the surgical planning of Fontan surgeries, which is one of the overall objectives of the multi-center Fontan research program. In addition, this method also correlates some of the important geometrical parameters of TCPC like the vessel dimensions with the TCPC hemodynamics, especially the power loss.

The skeletonization methodology and its application to analyze the Fontan geometries are discussed in detail in this chapter.

6.2 Skeletonization

Skeletonization, a commonly used technique in pattern recognition and shape analysis applications is now finding more and more opportunities in the medical field. Its ability to provide accurate geometrical information of complex shapes is the main attraction of this approach. Among the various techniques available to obtain the centerline representation of geometries, we chose the technique that iteratively adjusts a path toward the central axis. The simplicity of the algorithm and ease of implementation of the program are the major reasons for selecting this approach.

The basic principle of this method, as detailed in section 4.3, is to "slice" the geometry of interest into a series of frames and then define the geometric centerline as the line that connects the center of mass of each frame. However, such an approach is highly sensitive to the chosen slicing direction and may in some cases yield completely erroneous estimates of the geometry skeleton. Two major concerns are 1) though this technique tends to keep the path centralized the center of mass in a 2D slice may not lie along the central axis of the 3D structure and 2) this method does not guarantee that the path will stay within the geometry. In addition, when using the cross-sections obtained with the initial arbitrary slicing to perform further geometrical analysis, a commonly encountered problem was that the computed cross-sections did not actually correspond to the true vessel cross-sections. So to rectify these issues, an iterative procedure was added to the existing approach. The first iteration proceeds exactly as explained above, based on an arbitrary slicing direction prescribed by the user. In all subsequent iterations, however, the geometry is re-sliced in a direction perpendicular to the previously iterated centerline. In this way the results will be more accurate. Validation

studies performed to test the accuracy and sensitivity of this method to obtain the geometric centerlines are discussed in the following section

6.2.1 Validation Studies

The validation studies were performed on idealized Fontan models. These models have uniform vessel diameters for all four vessels. In addition, the model was positioned such that in the non-rotated configuration, the vessel axes were exactly aligned with the Z coordinate axis for the IVC and SVC and the X coordinate axis for the LPA and RPA.

Accordingly, the outputs expected from the skeletonization when applied to the non-rotated configuration were that: (i) the cross-sectional area plots of all four vessels should fall right on top of each other; (ii) the computed cross-sectional areas should be constant and equal to the design specification; and finally (iii) the computed center line should be parallel to the coordinate axis. The results shown in Chapter 5, demonstrate an excellent agreement between the theoretical and computed results in all respects.

The motivation for testing the two orientations was to assess the effect of the initial slicing direction and also to measure the extent to which the subsequent iterations where able to correct the erroneous start. Indeed, due to the 30 degrees rotation with respect to the center of the model, the vessel axes were no longer parallel to x or z – coordinate axes, which resulted in over estimated cross-sections after the first iteration. The main output of the skeletonization process when applied to the test-case was that the cross-sectional area plots obtained on the rotated configuration should be exactly identical to those obtained with the non-rotated one, As mentioned before, this aspect was validated as well and the code converged within a few iterations.

6.2.2 Reproducibility

Since the computation of geometric skeleton is an automated process, the only section that needs user interaction in the entire procedure is where the user has to define the meeting point of each vessel at the TCPC junction. The variability in this judgment affects the length of the computed skeleton. Intra observer error in determining each vessel's meeting point at the junction was calculated using 5 different users and the difference in the x, y and z co-ordinates of the point at the junction was quantified. The errors for all the four vessels were less than 5%. A detailed table used for the calculation of intra observer error is added in Appendix B

6.3 Geometrical Analysis

As mentioned earlier, quantifying the geometrical characteristics of various types of Fontan models was the main motivation of this study. We analyzed 26 TCPC models among which 13 were extra cardiac and 13 were intra atrial TCPCs. Among them, there was a subcategory of patients based on their clinical diagnosis as HLHS and non-HLHS, as shown in Tables 2.2 and 2.3. Another category was the group of patients with bi-lateral SVCs and five models were studied in this section. Finally, the last group was the patients whose MRIs were taken before and after the Fontan surgery, which included 3 patients. Among these 3 patients, two were from the extra cardiac vs. intra atrial group (one each) and one was from the bi-lateral SVC group. Results of the geometrical analysis performed on all the three categories are discussed in the following sections.

6.3.1 Extra Cardiac Vs. Intra Atrial

EC and IA anatomies result from different approaches to the surgical reconstruction of the Fontan baffle as described in the section 2.4.2. However, our results show that there is no significant difference in their baffle sizes. Instead the difference appears to be a higher standard deviation of the baffle cross-sectional area along its length in IA TCPCs when compared to EC TCPCs (Figure 5.10). Thus, it may be concluded that the IA baffle always has larger cross-sectional fluctuations than the EC conduit, which is to be expected as the former is constructed using part of the right atrium while a smooth and uniform graft conduit is used for the latter. The large standard deviation of the IVC cross-sectional areas observed in the IA TCPCs could also be the reason why there was no statistical significance between the IVC dimensions in IAs and ECs. No trends in the standard deviations of LPA and RPA could be detected.

IA patients showed significantly higher values in the ratio of mean cross-sectional areas of RPA to SVC, which is possibly because the TCPC junction for the IA and EC are not located at the same point on the native RPA. The native RPA anatomically decreases in diameter toward the right side, and the location on the RPA where the TCPC is constructed for the IA is possibly slightly shifted toward the left side compared to the EC TCPC. From a hemodynamic standpoint, the closer the TCPC is to the main pulmonary artery (MPA), the larger the PA sizes will be and thus the lesser the overall constriction in the flow transport.

There was no statistical significance in the curvature of the vessels at the meeting point of the TCPC junction. The reason for the large standard deviation in the curvature of the RPA may be attributed to a particular geometry, CHOP013 shown in Figure 5.8, in which the RPA was more curved than the other anatomies.

As depicted in Figure 5.14.a, the IA Fontans have lower collinearity (nearly significant) value than their EC counter parts. As defined in section 4.5.3.2, collinearity values approaching zero can be interpreted as their IVC and SVC are oriented in a head on collinear manner. So IA Fontans have an increased chance of flow stagnation and a highly unsteady and dissipative interaction between the colliding flows, compared to that in ECs. Since most of the ECs analyzed in this study have bi-directional Glenn (BDG) as their 2nd stage and IA have hemi-Fontan as their 2nd stage (Tables 4.5 and 4.6, respectively) it could be attributed that the difference between BDG and hemi-Fontan procedures are most likely the reason for the observed difference in collinearity. As shown in Figure 5.14.b, hemi-Fontans had smaller collinearity ($p = 0.0467$), than their BDG counterparts. This is counter-intuitive since hemi Fontans have the SVC anastomosed posteriorly as compared to the BDG. Therefore, we expected more collinearity for Fontans with the BDGs as their 2nd stage.

6.3.1.1 HLHS vs. non-HLHS Patients:

Results in Figure 5.12 show that the minimum LPA diameter (region of smallest cross-sectional area) depends on both the patient's single ventricle pathology (HLHS or non-HLHS) and also the surgical protocol (EC or IA).

Figure 5.12c shows all possible combinations of the EC/IA and HLHS/non-HLHS categories (EC HLHS, EC non-HLHS, IA HLHS and IA non-HLHS) and the important conclusion is that, for HLHS patients who underwent IA surgery, the minimum LPA size is significantly smaller than their minimum RPA size ($p = 0.0227$). The trend is the same for HLHS patients who underwent EC surgery too but there is no statistical significance ($p = 0.1562$). The lack of significance may be due to the fact that the minimum RPA is also smaller owing to the right shifted attribute of EC TCPCs which, as discussed in the

previous section, makes the RPA area also small and thus reduces the relative difference between LPA and RPA cross-sectional areas. From these data, it is clear that the HLHS patients have a significantly constricted LPA, which, could be attributed to the aortic reconstruction procedure, where the reconstructed aorta appears to compress the LPA.

Interestingly, for non-HLHS patients, results show that the minimum LPA size of the patients who underwent IA surgery was near-significantly smaller than the minimum LPA size of patients with EC surgery. The trend is the same for minimum RPA size but with no statistical significance. Precise reason for this observation cannot be distinguished from these data.

6.3.1.2 Discrete and diffuse stenosis:

There are two types of anatomically observed stenosis morphologies: (1) a discrete stenosis in which the vessel is constricted for a smaller vessel length and will be expanded after the constriction region (2) a diffuse stenosis in which the vessel constriction is observed for a longer length compared to the discrete stenosis. Figure 6.1 shows the discrete and diffuse stenosis seen in two TCPC reconstructions used in this study.

Among the 26 patients analyzed in the EC vs. IA study population, severe LPA stenosis was observed in 13 patients by visual inspection of their 3D reconstructions. Table 6.1 groups the stenosis seen in these patients as the discrete and diffuse categories. Among the six discrete stenosis cases, except CHOA009 all other patients have HLHS. Among the seven diffused stenosis patients 3 have HLHS (CHOA007, CHOP008 and CHOP092) and CHOP088 have a hyplostatic aortic arch that needs an aortic reconstruction.
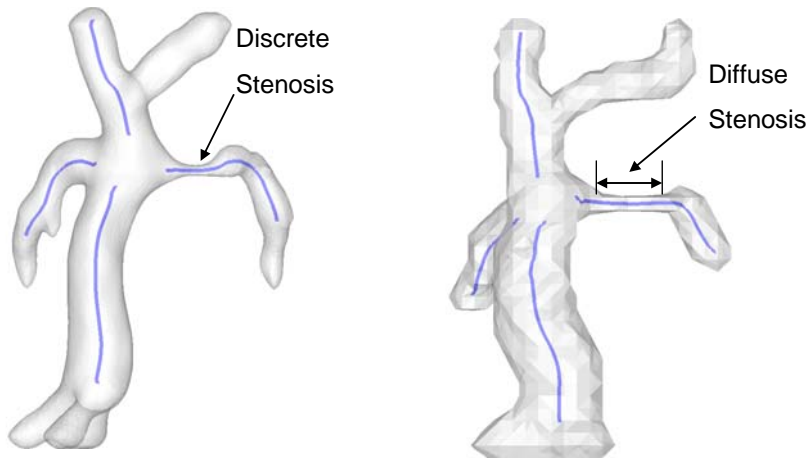
(a) CHOP013   (b) CHOP092

Figure 6.1: Two types of LPA stenosis: (a) discrete and (b) diffuse stenosis are shown using the anatomic reconstruction of two TCPC geometries

Table 6.1: Patients having discrete and diffused LPA stenosis

Discrete Stenosis	Diffused Stenosis
CHOA009	CHOA007
CHOA011	CHOP008
CHOP006	CHOP088
CHOP008	CHOP092
CHOP013	CHOP095
CHOP018	CHOP096
	CHOP0116

6.3.2 Pre vs. post Fontan

Pre Fontan patients have only their SVC attached to the pulmonary arteries, while the IVC still drains to the right atrium. Since the Fontan operation is performed after 12 months to a couple of years after the second stage surgery, notable variations in the geometric characteristics were expected. However, the mean vessel cross-sectional area of the geometries showed surprising behavior after the surgery. For the SVC and LPA there was a small reduction in vessel area (Figure 5.18). These reductions in cross sectional area after the TCPC surgery could be due to acute post surgical trauma of the vessels. However, this could only be proved using the long-term follow up data on these patients, which were not available during the time of this study.

Since there were only 3 pairs of patients in this study no statistical analysis could be performed. Also the patient distribution was in consistent; two were from the same hospital (CHOP) and the third one from CHOA, and one of the two datasets from CHOP had a bilateral SVC connection.

Figure 6.2 shows the vessel cross-sectional areas for the 3 pre and post Fontan pairs. From this figure, it is clear that this reduction in area after the surgery was noted only for the two patients from CHOP, while the third pair from CHOA had an increase in vessel dimensions after the surgery.
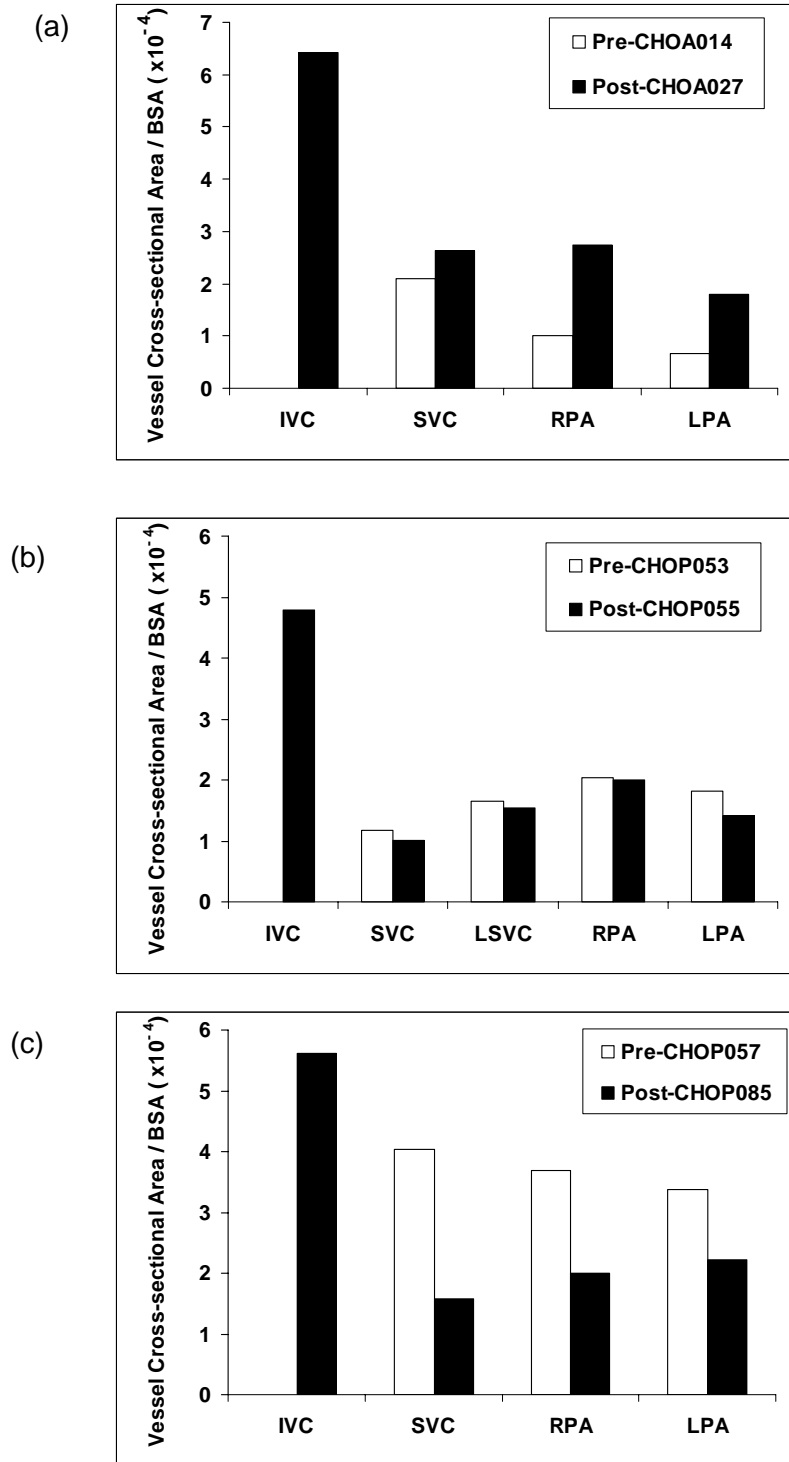
Figure 6.2: Vessel cross-sectional area for all the vessels in the vicinity of TCPC for the three patient pairs before and after the Fontan operation is shown here. Note the reduction in vessel areas of SVC and LPA for figures b and c.

The standard deviation of the cross-sectional areas along the vessel length did not vary significantly between the pre and post geometries for all vessels. This was expected, as the surgery does not involve any PA or VC vessel reconstructions. Similarly, the minimum vessel cross-sectional areas were approximately the same before and after the surgery for both of the pulmonary arteries. This re-confirms the previous observation (seen in Figure 5.12) that narrowing of the LPA could be due to the aortic reconstruction performed in HLHS patients during the 1st stage of the Fontan surgery and that 2nd or 3rd stage do not contribute to this phenomenon.

The larger standard deviation in the RPA curvature of post Fontans may be due to the higher curvature of the RPA of CHOP085 as seen in Figure 5.6. An increase in the vessel curvatures were observed for the right and left PAs of post-operative anatomies as compared to the pre-operative ones (Figure 5.21). Potential reason for such an observation could the addition of flaring and offset to the TCPC structure during the connection of IVC baffle onto the 2nd stage anatomy.

6.3.3 Bilateral SVC

It is the presence of an additional SVC that differentiates bilateral SVCs from other Fontans. The TCPC connection aspects of bilateral SVCs are similar to other Fontans except the location of the IVC with respect to the two SVCs and the vessel dimensions of the two SVCs. As shown in Figure 5.7, for some cases the IVC was connected in between the two SVCs (CHOP032 and CHOP022), while for others the IVC was connected facing the RSVC (CHOA039 and CHOP019).

Comparison between the mean vessel cross sectional areas of right and left SVC for the 5 bi-lateral geometries, showed that both the vessels have a similar cross sectional area (Figure 5.23). This motivated us to compare all the vessel areas of the bi-

lateral SVCs with their Fontan counterparts. As explained in the results section 5.3.3.1, all five bi-laterals in this study had an extra cardiac connection for their TCPC. So we decided to choose EC TCPC for comparison purposes. Also RSVC of the bi-lateral model was used to compare with the SVC of EC Fontan. This is because, in most of the bi-lateral SVC's it is the RSVC that is connected near to the IVC and the LSVC is located more towards the left lung.

There was no difference between the vessel areas of the pulmonary arteries. However, RSVC of the bi-lateral model showed smaller cross sectional area when compared to the SVC of the EC TCPC. Table 5.3 shows that LSVC also had the same trend (Mean vessel cross sectional areas for each of these vessels are: RSVC = $0.95 \text{X} 10^{-4}$, LSVC = $1.07 \text{ X} 10^{-4}$, and EC SVC = $1.34 \text{ X} 10^{-4}$). IVC cross sectional area of the bi-lateral model was also less than the EC IVC area. Area variation across the vessel length for RSVC and LSVC showed a higher variation on the LSVC.

Because some of the models have their IVC connected directly to the PAs, no intra group comparison seems fair for the vessel curvature and offset analysis as the computation of these parameters involve the meeting points of the vessels at the connection site. For bi-lateral SVCs it was hard to define a TCPC junction point for the pulmonary arteries. Computed values for each model are tabulated in Tables 5.4 and 5.5.

6.4 Anatomy vs. Hemodynamics

As discussed in the previous section, comparison of the extra cardiac and intra atrial geometries showed that minimum LPA diameter is the most distinguishing geometric feature and is intimately related to both the underlying pathology (HLHS or non-HLHS) and surgery type (EC or IA). In this section, we examine the influence of geometric factors on the patient's *in-vitro* and *in-vivo* hemodynamics, with a specific emphasis on the minimum PA diameter. Essentially, this section tries to answer the following questions: "Do the anatomic characteristics of the TCPC impact its hydrodynamic efficiency?", and "Does this affect the functioning of the single functioning ventricle?" What is shown in the following subsections is that the minimum PA diameter is the most important geometrical parameter that has the highest impact on TCPC hemodynamics and that it does in turn significantly impacts patient cardiac output and ventricular loading.

6.4.1 TCPC Power Loss:

From the experimental power loss plot shown in Figures 5.25, it is clear that minimum LPA size, which is a measure of the geometric bottleneck of the TCPC, is the primary influencing factor in determining the TCPC efficiency, with $\dot{E}_{loss}/E_0$ scaling inversely with minimum LPA area. This correlation was stronger in the 50-50 pulmonary flow split condition. However, no significant correlation between the minimum vessel area and power loss was seen with MRI flow split condition or at equal pulmonary resistance (Figures 5.26 and 5.27). However, when looking at the values of the pulmonary flow splits obtained from PC MRI (Table 6.2), it is striking that geometries

with unbalanced PA dimensions lead to unbalanced flow splits and lung perfusion (Ex: CHOA008 with an RPA stenosis, CHOP013 with an LPA stenosis).

This re-confirms the fact that, in the actual Fontan physiologic condition, the flow splits are naturally adjusted to incorporate any vessel narrowing like an LPA stenosis. In order to shed further light on this phenomenon, let us consider a simple Poiseuille flow in a rigid straight pipe. The relationship between pressure drop, ΔP, across the pipe and the flow rate Q, going through it is given by:

$$\Delta P = -\frac{8L\upsilon}{\pi R^4} Q \qquad\qquad\qquad (6.1)$$

where R is the pipe radius, L is the pipe length and υ is the dynamic fluid viscosity. Based on this simple example, we can see that in a straight pipe the resistance opposed by the pipe to the flow scales as R^{-4}. Given the choice between two pipes with radii R_1 and R_2 such that $R_1 < R_2$, the pressure drop required to force a flow rate Q through pipe 1 will be higher than through pipe 2, which in terms of power losses translates into higher power loss in pipe 1 than pipe 2 for a given flow rate. Accordingly, if one of the PAs is constricted, decreasing (up to a certain point) the share of the flow going through the constricted vessel will decrease the overall power losses. This is basically what comes out of the MRI flow splits listed in Table 6.1. Given a constriction along the vasculature, the body tends to redistribute the flow to minimize energy losses along the way. Thus when more flow is imposed on the constricted vessels, this results in higher power losses within the TCPC. For example, as shown in Table 5.6, the CHOP013 geometry results in a larger power loss at 50-50flow split compared to the MRI condition (PL $_{50\%lpa}$ = 135.99mW vs. PL $_{MRI}$ = 11.50mW) and this geometry has a severe LPA stenosis (see Figure 5.6).

Table 6.2: MRI flow split conditions for the six experimental models computed using the PCMRI data.

Model	Mean IVC Flow Rate (L/Min)	Mean SVC Flow Rate (L/Min)	Mean RPA flow rate (L/min)	Mean LPA flow rate (L/Min)	LPA/RPA flow split
CHOA007	1.01	1.03	1.04	0.929	50-50
CHOA008	0.93	1.37	0.57	1.28	70-30
CHOP013	1.85	1.42	1.37	0.83	60-40
CHOA009	0.82	1.15	1.03	1.08	50-50
CHOA011	2.56	1.48	0.72	2.47	80-20
CHOP034	3.31	1.93	1.85	2.27	55-45

When evaluating the power loss values obtained from the CFD simulations, (as shown in Figures 5.28-5.30), it was the minimum RPA area that exhibited the highest correlation. This suggests that efficiency of TCPC depends highly on the outlet vessel diameter (i.e., either LPA or RPA). To further confirm this observation, the minimum PA values were plotted against the power loss obtained from both CFD and experimental studies as shown in Figure 6.3. A combined plot showing the power loss from the two modalities plotted against the minimum PA area is also shown in Figure 6.4.
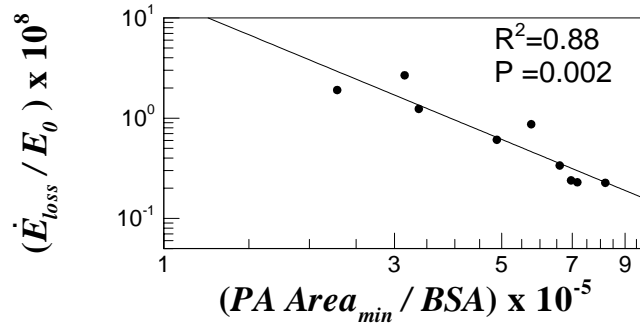
(a) CFD power loss
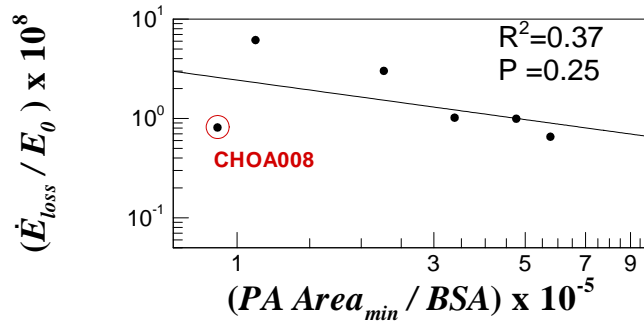
(b) Experimental power loss

Figure 6.3: Minimum PA values of RPA and LPA plotted against the normalized power loss ($\dot{E}_{loss}/E_0$) at MRI flow split condition obtained from (a) CFD; (N=9) and (b) experimental (N=6) studies. The CHOA008 model with a severely stenosed RPA is marked in the red circle.
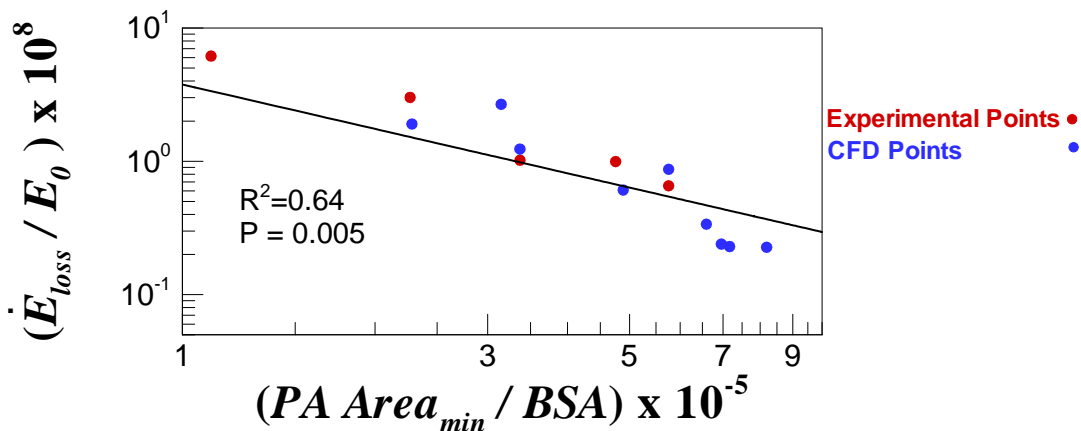
Figure 6.4: Minimum PA values of RPA and LPA vs. the power loss obtained from both CFD (blue) and experimental (red) studies at MRI flow split condition (N=15). The common trend line for data points from both the modalities is shown in black.

Good correlation between the minimum vessel areas of the PAs and the power loss are seen in these figures except for Figure 6.3b, which is the experimental power loss condition. Further investigation showed that the low correlation was due to one particular data set used in experimental power loss, CHOA008. The anatomic reconstruction of this data showed a severely stenosed RPA (Figure 6.5 a). However, when the model was used for experimental analyses, the stl file used to create stereo-lithographic model of CHOA008 was sliced before the stenosis site (see Figure 6.5b). When the plot shown in Figure 6.3b is redrawn without CHOA008, the R^2 value jumps to 0.96 indicating a very strong correlation (see Figure 6.6a). Similarly for the combined plot of CFD and experimental vs. min PA area, the correlation coefficient increased to R^2 = 0.91 (see Figure 6.6b). This again confirms the fact that any narrowing of the pulmonary arteries could result in a larger power loss within the TCPC.
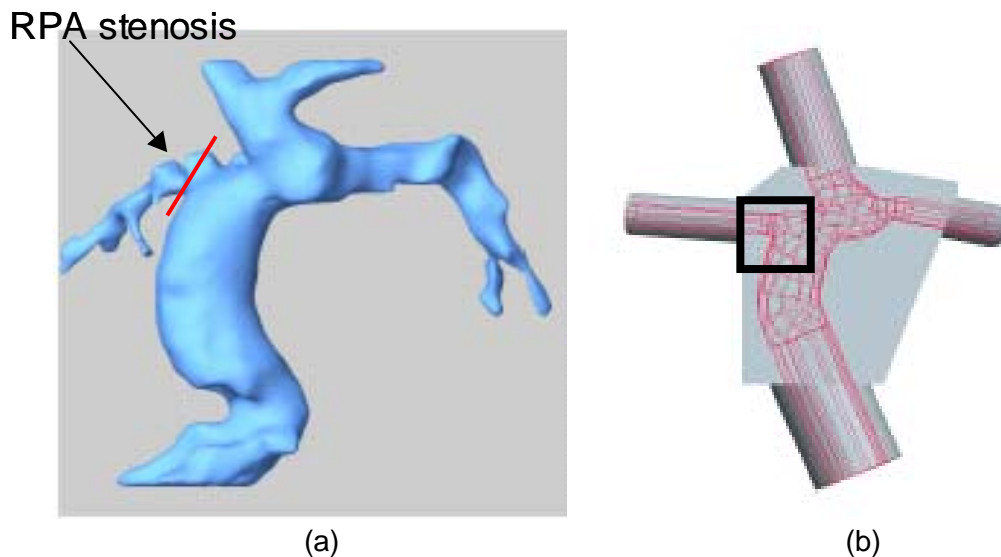
Figure 6.5: (a) 3D anatomic reconstruction of CHOA008. Red bar shows the point where the RPA was sliced for making stl model and the black arrows shows the severe RPA stenosis. (b) The stl model of CHOA008 used for experimental study. The end of the RPA vessel in the model is shown inside the black box.
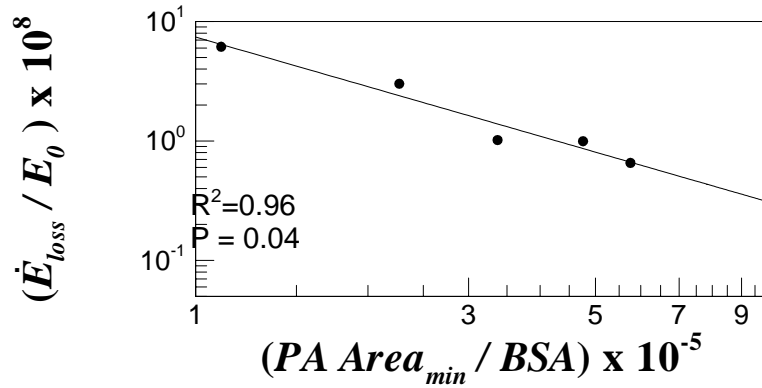
(a)
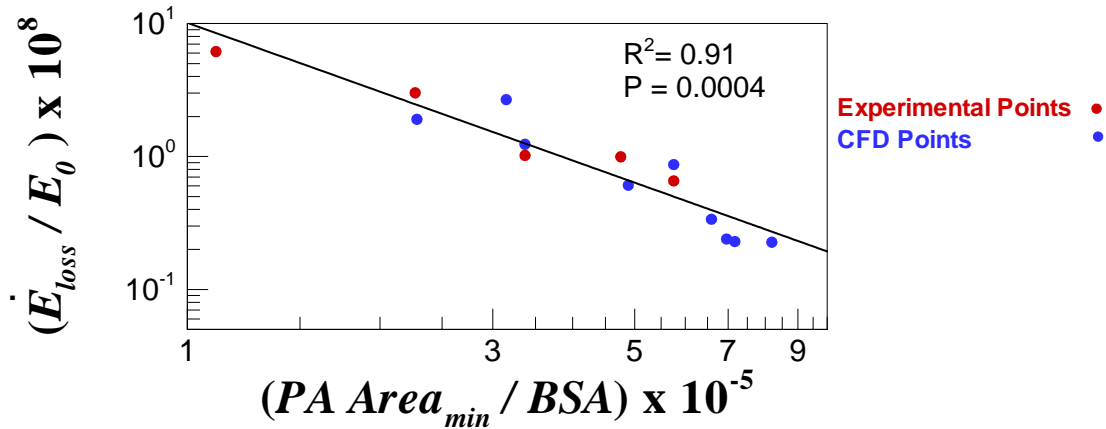
(b)

Figure 6.6: Minimum PA values of RPA and LPA plotted against the normalized power loss ($\dot{E}_{loss}/E_0$) at MRI flow split condition obtained from; (a) experimental (N=5) studies alone and (b) experimental and CFD studies combined (N=14), after removing the CHOA008 point, which was used for experimental studies.

The highest correlation coefficient (R^2-value) of 0.96 for the power loss vs. minimum LPA area (see Figure 5.25c) for the experimental studies shows that all other relevant geometric parameters have second order effects in relation to the minimum LPA area. From a fluid mechanics standpoint, the relationship between $\dot{E}_{loss}/E_0$ and the geometry is multivariate with possible varying non-linearities associated with each

parameter. Given the extent of correlation observed in Figure 5.25c, the trends observed in Figure 5.25a, b, and d cannot be the true trends with respect to the corresponding variables (minimum vessel areas of IVC, SVC and RPA). Due to the small sample size a multivariate analysis was not possible in this study. As a result, the dominating influence of the minimum LPA area could mask out the real trend of other geometric parameters. For example, the increasing trend for $\dot{E}_{loss}/E_0$ with minimum RPA area does not make physical sense, as clearly a reduction in RPA diameter (e.g. RPA stenosis) must increase the power loss. By plotting the ratio of $\dot{E}_{loss}/E_0$ with the power-law fit from Figure 5.25c, i.e. further indexing the data with respect to minimum LPA area, it was found that the trend reversed thus showing that $\dot{E}_{loss}/E_0$ does increase with decreasing RPA minimum area when accounted for the confounding minimum LPA area. Figure 6.7 shows the power loss plots for the experimental studies after indexing with the power-law fit from the LPA plot (Figure 5.25c) for minimum vessel areas of IVC, SVC and RPA. Note that, the IVC plot, which showed a decreasing power loss with increasing IVC area, also had a less significant trend after removing the effect of the LPA.

While our data cannot provide the complex functional relationship between $\dot{E}_{loss}/E_0$ and all the geometric parameters, it is however sufficient to show that minimum PA area is the most important factor in determining TCPC power loss rate when compared all other factors as shown in Figures 5.25 - 5.31.
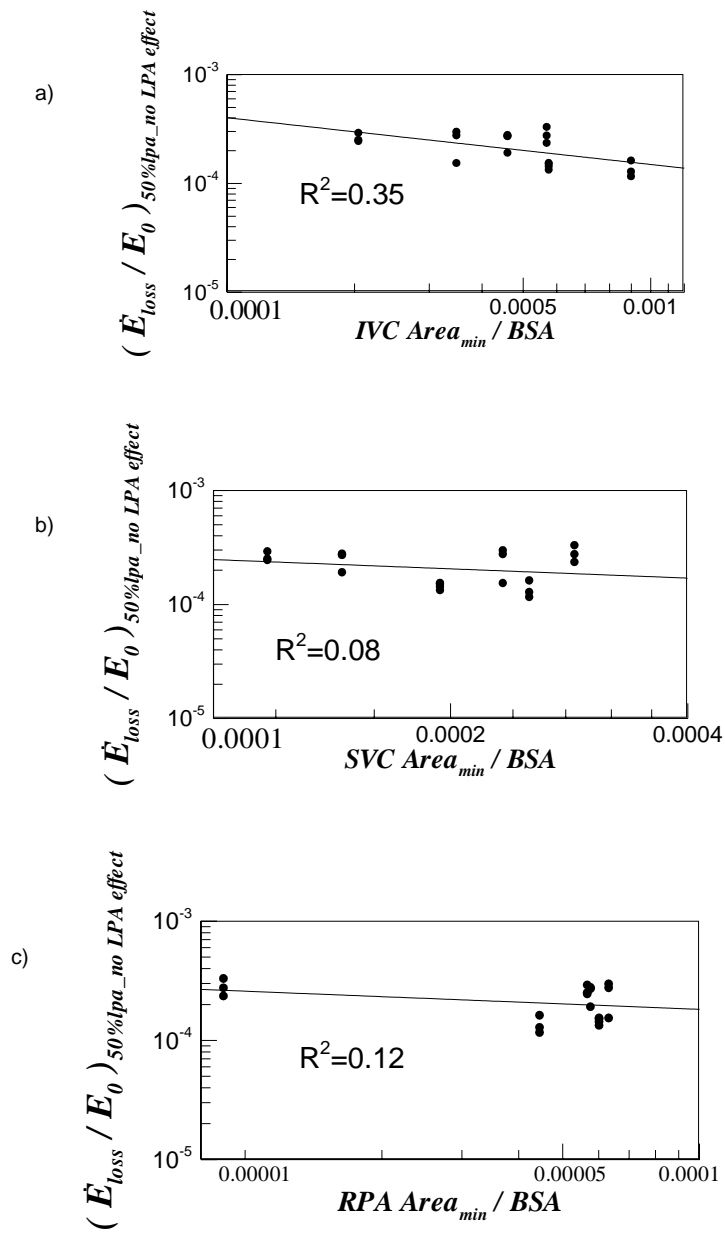
Figure 6.7: Normalized experimental power loss ($\dot{E}_{loss}/E_0$) at 50-50 flow splits and all the cardiac output indexed with the power-law fit of LPA plotted against the minimum cross-sectional areas of: (a) IVC and (b) SVC and (c) RPA.

In addition to the pulmonary arteries, the IVC also showed a strongest correlation with power loss, (with R^2 values around 0.5). This was observed in both experimental

cases. This strong correlation between power loss and minimum IVC area could be due to the fact that, an input flow split of 60-40 is assigned between IVC and SVC for both experimental and CFD studies. Especially, in case of 50-50 flow split, it is the IVC that carries the highest flow rate (IVC – 60%, SVC – 40% and LPA and RPA – 50% each). This relation was clearly seen in the figures 5.25 and 5.28 that plotted 50-50 flow split condition for both experimental and CFD studies (with R^2 values of 0.50 and 0.61, respectively). Also because of this high flow rate in the IVC, when there is a vessel constriction in IVC, it will show a power loss. As seen in figures 5.6 and 5.7, some of the IVC vessels show severe constriction in the vessel cross-sectional areas (Eg; CHOP 018, CHOP034, CHOP037). This could also impact the power loss.

Given the statistical significance of the standard deviation of IVC area, we examined if this geometric parameter correlated with $\dot{E}_{loss}/E_0$. Since the ratio of the standard deviation to the mean is a measure of in homogeneity, higher losses for larger values of this ratio are expected, analogous to the effect of wall unevenness in simple pipe flows. However, there was no significant correlation (Figure 6.8). To further investigate the correlation between IVC area variance and power loss, power loss from both CFD and experiments were plotted separately for EC and IA TCPCs. However, no significant correlation was seen for both the categories at MRI condition and at 50% flow split (Figure 6.9)
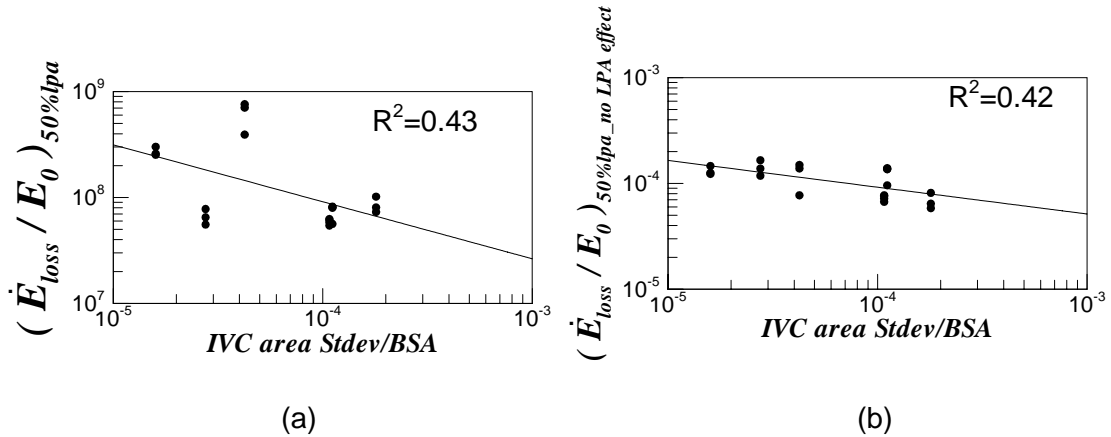
Figure 6.8: Normalized experimental power loss ($\dot{E}_{loss}/E_0$) at 50-50 flow splits and all the cardiac outputs plotted against IVC area standard deviation (a) with and (b) without the effect of LPA

(a) MRI flow split for EC TCPC

(b) MRI flow split for IA TCPC

(a) 50-50 flow split for EC TCPC

(b) 50-50 flow split for IA TCPC
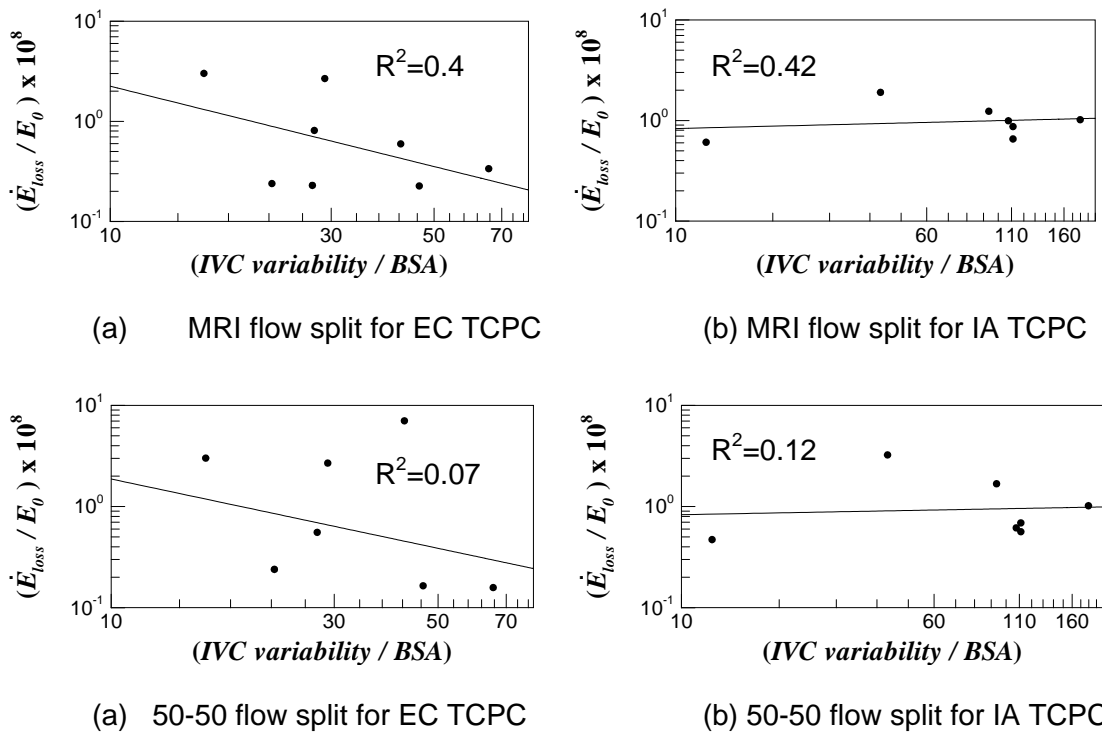
Figure 6.9: Cardiac index plotted against the normalized power loss ($\dot{E}_{loss}/E_0$) from CFD and experimental studies combined at MRI flow split for (a) extra cardiac TCPC (b) intra atrial TCPC and at 50-50 flow splits for (c) extra cardiac TCPC (d) intra atrial TCPC. N=8 for EC and N=7 for IA

This once again points out that the primary confounding variable is the minimum PA diameter (in this case the LPA), and the notion that a large "fluctuating" IVC morphology produces higher power loss appears to be a second order effect. The dominance of size vs. shape with respect to power loss is in fact classical. Even in simple pipe junction flows, the pipe diameter plays a more dominant effect on power loss than surface roughness or other geometric shape factors (angle, curvature etc). Similar to standard deviation of IVC area, we have seen that there was no significant correlation for any of the other parameters calculated, namely collinearity and offset. The correlation of power loss vs. these parameters with and without the LPA effect is shown in Figures 6.10 and 6.11, respectively.

(a)   (b)
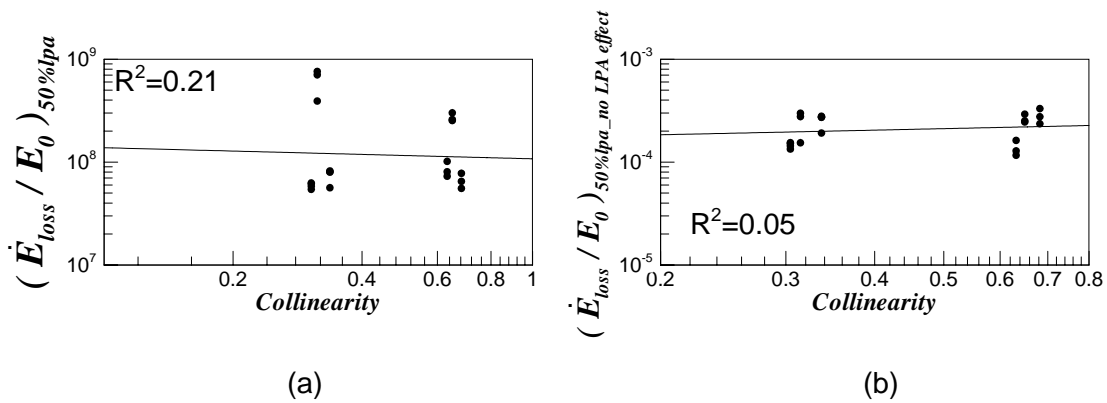
Figure 6.10: Normalized experimental power loss ($\dot{E}_{loss}/E_0$) at 50-50 flow splits and all the cardiac outputs plotted against collinearity (a) with and (b) without the effect of LPA
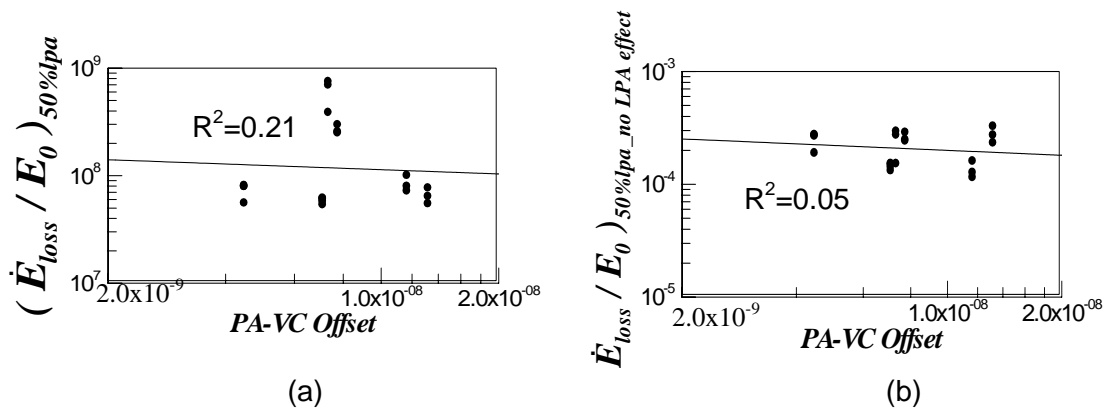
Figure 6.11: Normalized experimental power loss ($\dot{E}_{loss}/E_0$) at 50-50 flow splits and all the cardiac outputs plotted against PA-VC offset (a) with and (b) without the effect of LPA

6.4.2 Cardiac Index:

The Result section extensively investigates the relationship of power losses to different geometrical features of the TCPC. However, this approach only provides a local measure and does not grant that the local TCPC hemodynamics truly impact the whole cardiovascular system. Cardiac index was thus brought into the picture as a metrics that is representative of the performance of the whole cardiovascular circuit. Results show that minimum LPA diameter is inversely correlated with power loss (Figures 5.25c) and positively with cardiac index (Figure 5.33). The direct translation of these correlations is that a stronger vessel constriction (smaller minimum LPA diameter) corresponded to higher energy dissipation in the TCPC (higher power loss) as well as to a lower cardiac index. To more quantitatively assess the relationship between those three parameters, Figures 5.25c and 5.33 are collapsed into a single one in Figure 6.12. The black data points and trend-line represent the cardiac index data, while the red trend-line represents the regression fit for power losses. This regression was obtained based on

the *in-vitro* experimental power loss shown in Figure 5.25c, leading to the following expression for power loss in the TCPC:

$$\dot{E}_{loss} = 294.65\left(\rho\,\frac{Q^3}{BSA^2}\right)\left(\frac{LPA_{\min}}{BSA}\right)^{-5/4} \text{(Watts)} \tag{6.2}$$

The display retained for Figure 6.12 shows the impact of minimum LPA area on both power loss within the TCPC itself and on the cardiac index on the same graph. For a given minimum LPA area, the corresponding cardiac index can be read by taking the point on the cardiac index curve (shown in black in the figure 6.12) and reading its coordinate on the left axis. Similarly, the corresponding normalized power loss through the TCPC can be read using the red curve along with the right axis. It can thus be seen that (Figure 6.13 shows the details of this calculation), a normalized minimum LPA area of 3×10^{-5} corresponds to a normalized power loss of 1.3×10^8 and a cardiac index of $2.75 L/min/m^2$, while a normalized minimum LPA area of 9×10^{-5} corresponds to a normalized power loss and cardiac index of 0.4×10^8 and $3.25 \ L/min/m^2$, respectively. By plotting these three variables together, it is thus evident that energy dissipation across the TCPC and cardiac performance (via the cardiac index) are intimately related, and a variation in the TCPC power loss can impact the resting cardiac index by up to 50%.

Finally, it should be noticed that the power loss relation given in Equation 6.2 has an exponential relationship to both minimum LPA area, LPA_{min}, and flow rate, Q. Accordingly, if a small variation in LPA_{min} was shown to have a strong impact on power loss and cardiac index under resting conditions, this impact will be amplified under exercise conditions.
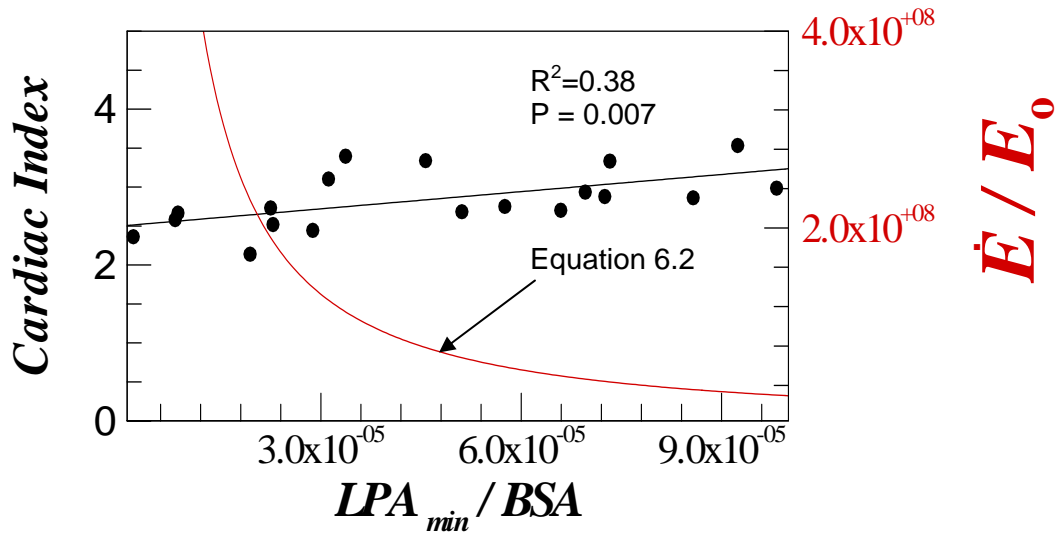
Figure 6.12: Cardiac index plotted against normalized LPA minimum area. Also depicted is Equation 6.2 in red color, which shows the relation between TCPC power loss and the minimum LPA area.
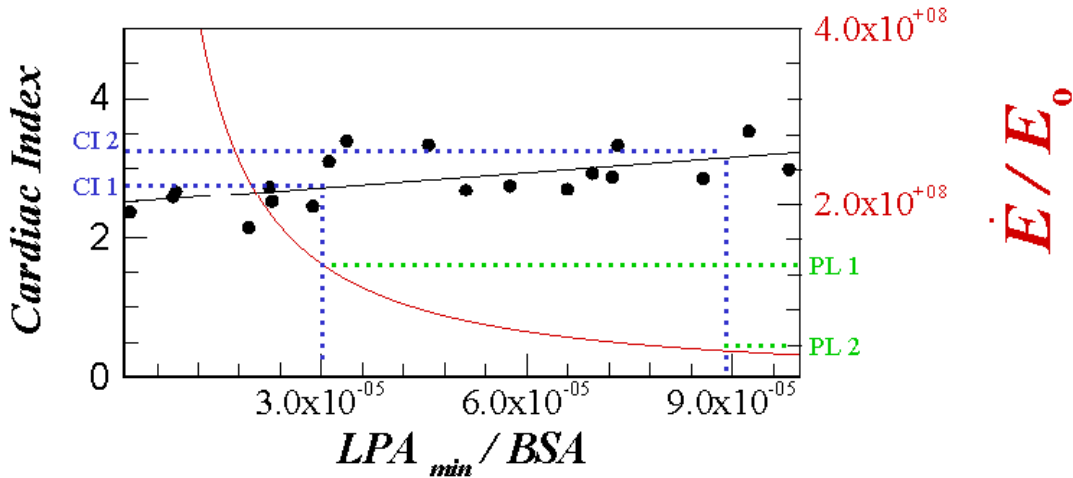
Figure 6.13: Cardiac index plotted against normalized LPA minimum area along with the TCPC power loss (shown in red). For ease of reading the graph, readings correspond to two LPA areas 3 X 10-5 and 9 X 10-5 is explained here. PL1 and PL2 (shown in green) correspond to the power loss for the LPA areas 3 X 10-5 and 9 X 10-5 respectively, while CI 1 and CI2 (shown in blue) are their respective cardiac indices.

Even though a statistically significant correlation was seen between the minimum LPA area and cardiac index, no significant relationship could be identified when the cardiac index was plotted against the minimum PA area as shown in figure 6.14.
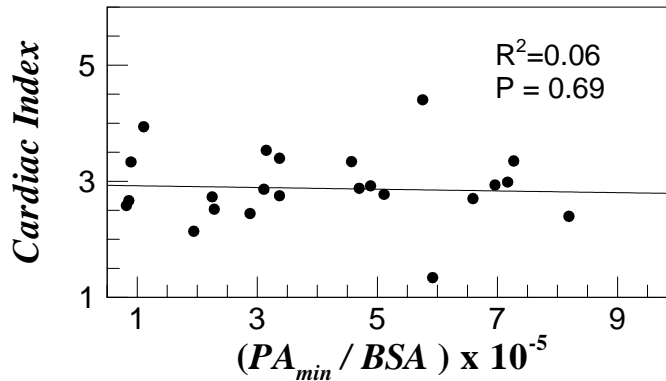
Figure 6.14: Cardiac index plotted against normalized minimum PA area. No significant correlation was seen in this case.

6.4.3 Ventricular power output:

The high regression and low P value (0.04) between $\dot{E}/E_0$ and the normalized minimum LPA diameter confirm that the ventricular power output increases with decreasing PA diameter (increasing resistance), especially with the minimum LPA which showed the highest correlation. In other words, the single ventricle pump has to increase its power if there is an increase in the resistance. However, considering that the cardiac index decreased with decrease in minimum LPA diameter, the heart is not only pumping harder (at increased resistance) but also fails to compensate by providing sufficient cardiac output. The statistical significance (p = 0.04) of this result underscores that the TCPC geometry (in particular the minimum PA size) is extremely important since it does impact ventricular function and loading. Furthermore, the data shown in Figure 5.34 only correspond to resting conditions, which means that if the single ventricle fails to compensate under resting conditions, exercise conditions will be extremely challenging.

Given that the minimum LPA diameter is intimately related to both TCPC geometry (i.e. EC or IA) and pathology (i.e. HLHS or non-HLHS) as shown in Figure 5.12, the study Group 1 (IA vs. EC) was further subdivided according to patients'

diagnosis for a deeper examination of ventricular power output as a function of these variables. While Figure 5.35a shows that the ventricular power output for IA TCPCs is higher, the impact of the TCPC on the non-HLHS patients clearly seems less severe with a lower workload than in HLHS patients. This finding, juxtaposed with previous results on the performance of HLHS and non-HLHS patients [Sundareswaran, 2006], reveals a clear message: i.e, hypoplastic left ventricles, which are poor pumps to begin with, unfortunately need to work harder than their non-HLHS counterparts. Figure 5.35c shows all possible combinations and shows that among the HLHS patients, IA TCPCs are associated with higher workloads than EC TCPCs. The figure also shows that the ventricular power output for EC TCPCs is about the same for both HLHS and non-HLHS patients. Therefore, it may be concluded that EC surgery is beneficial to the ventricle irrespective of whether the patient has HLHS or not. However, the precise reason for this finding needs further research and understanding of the Fontan physiology.

As discussed earlier, it has been shown that the lower minimum LPA sizes in HLHS patients is due to their aorta reconstruction, in which the aorta anatomically rests on the LPA, causing LPA stenosis. In order to support this finding a reconstruction of one of the non-HLHS patient anatomy is presented here and compared to an HLHS patient anatomy (Figure 6.15). We would like to emphasize that the LPA, which passes under the aorta is extremely susceptible to physical contact forces. An enlarged aorta as seen in HLHS patients easily constricts space available for LPA and may limit growth of the LPA and perhaps indirectly the left lung.
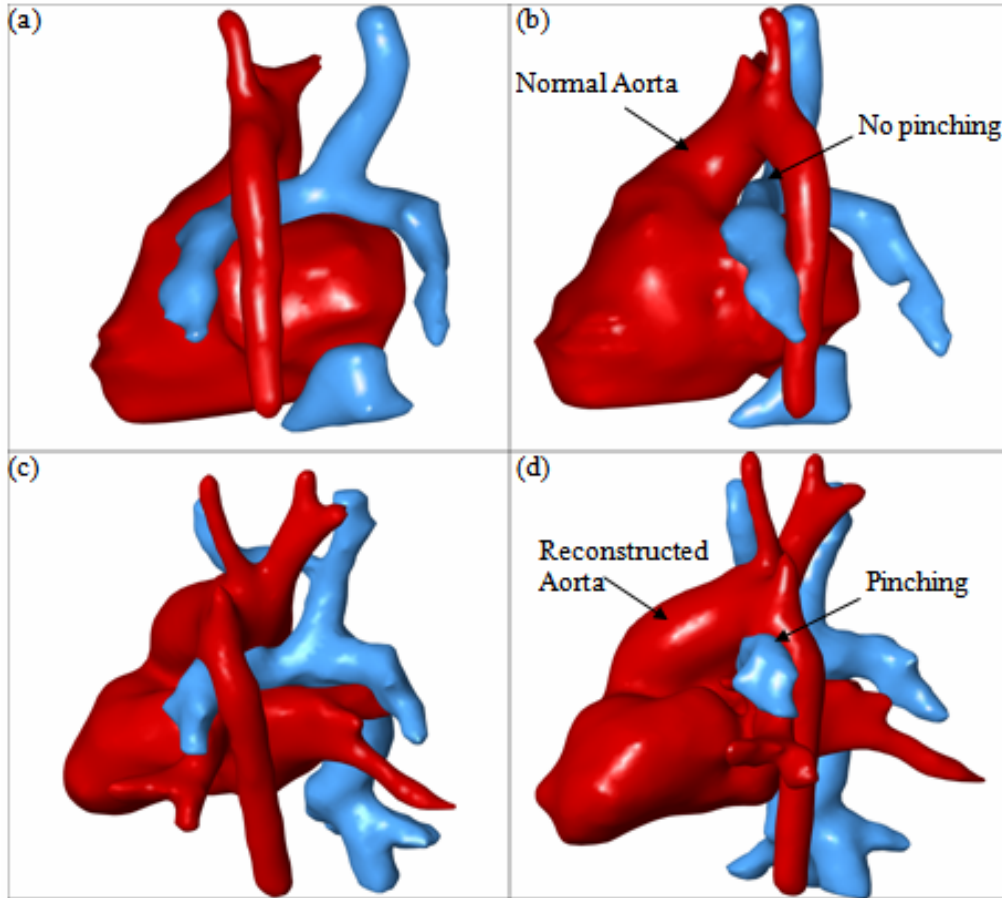
Figure 6.15: Reconstructed anatomy of the heart and TCPC of a non-HLHS patient depicted by (a) coronal perspective and (b) sagittal perspective compared against respective HLHS patient anatomy featuring its reconstructed aorta in (c) and (d).

Another important factor about the aortic reconstruction is that, though all the patients diagnosed with HLHS need aortic reconstruction, not all patients with aortic reconstructions have HLHS. For example, among the patients analyzed in this study, CHOP088 (see Table 6.3) is a patient with no HLHS. But, the clinical data shows that this patient has hypoplasia of the aortic arch, which needs an aortic reconstruction similar to the HLHS patients. The narrowing of the LPA is seen for this patient as in the case of HLHS patients (Figure 5.8). Tables 6.3 and 6.4 shows the list of all the 26

patients (both EC and IA) along with their clinical diagnosis and points out that among

these patients who all needed an aortic reconstruction.

Table 6.3: Extra cardiac Fontans categorized into patients with and without aortic reconstruction.

Patient	Diagnosis	Needed Aortic Reconstruction? (Yes/No)
CHOA007	HLHS	Yes
CHOA008	HRHS,TA	No
CHOP006	HLHS	Yes
CHOP007	HRHS, Ebstein's anomaly	Yes
CHOP013	HLHS, ASD	Yes
CHOP067	SV-DI LV,VPS-TGA	Yes
CHOP085	HLHS	Yes
CHOP088	DX, Juxtaposition of atria appendages,TA, TGA,AA hypoplasia	Yes
CHOP089	TA,VSD	No
CHOP090	PA,IVS, RV-Hypertrophy	No
CHOP091	DO-RV,IVS,MA,PA	No
CHOP095	DI LV,PA	No
CHOP116	Ebstein's Anomaly	No

EC – extra cardiac; Hemi - hemi-Fontan; BDG - bidirectional glenn; HRHS - hypoplastic right heart syndrome; HLHS - hypoplastic left heart syndrome; TA - tricuspid atresia; ASD - atrial septal defect; VSD - ventricular septal defect; SV - single ventricle; LV - left ventricle; RV - right ventricle; DI - double inlet; DO - Double Outlet; TGA - transposition of great arteries; DX – dextrocardia; AA - aortic arch; PA - pulmonary atresia; MA -Mitral Atresia; IVS - intact ventricular septum

Table 6.4: Intra atrial Fontans categorized into patients with and without aortic reconstruction.

Patient	Diagnosis	Needed Aortic Reconstruction? (Yes/No)
CHOA004	HRHS,TA, VSD, PS	No
CHOA009	SV-DI AV connection	No
CHOA011	HLHS	Yes
CHOA027	HRHS, TGA, TA, VSD, LPA hypoplasia	Yes
CHOP008	HLHS	Yes
CHOP018	HLHS, ASD	Yes
CHOP030	TA, VSD	No
CHOP034	HRHS,SV,DX, TA,VSD,PS	No
CHOP037	PA, HRHS	No
CHOP068	HLHS	Yes
CHOP073	HLHS	Yes
CHOP092	HLHS, TGA, Hypoplastic AA, VSD	Yes
CHOP096	PA	No

IA -intra atrial; Hemi - hemi-Fontan; BDG - bidirectional glenn; HRHS - hypoplastic right heart syndrome; HLHS - hypoplastic left heart syndrome; TA - tricuspid atresia; ASD - atrial septal defect; VSD - ventricular septal defect; SV - single ventricleAV - atrioventricular; DI - double inlet; TGA - transposition of great arteries; DX – dextrocardia; AA - aortic arch; PA - pulmonary atresia; PS - pulmonary stenosis; DSK - Damus-Stansel-Kaye procedure

6.4.4 Pulmonary Vascular Resistance:

Systemic and pulmonary vascular resistance (SVR and PVR, respectively), based on catheter measurements was available for five of the twenty-six patients analyzed in this study. Figure 6.16 shows the SVR and PVR for the five patients plotted against their respective power loss. From this figure it is clear that, though the correlation coefficient R^2 was small, when the resistance increase, the power loss also increase for both SVR and PVR.
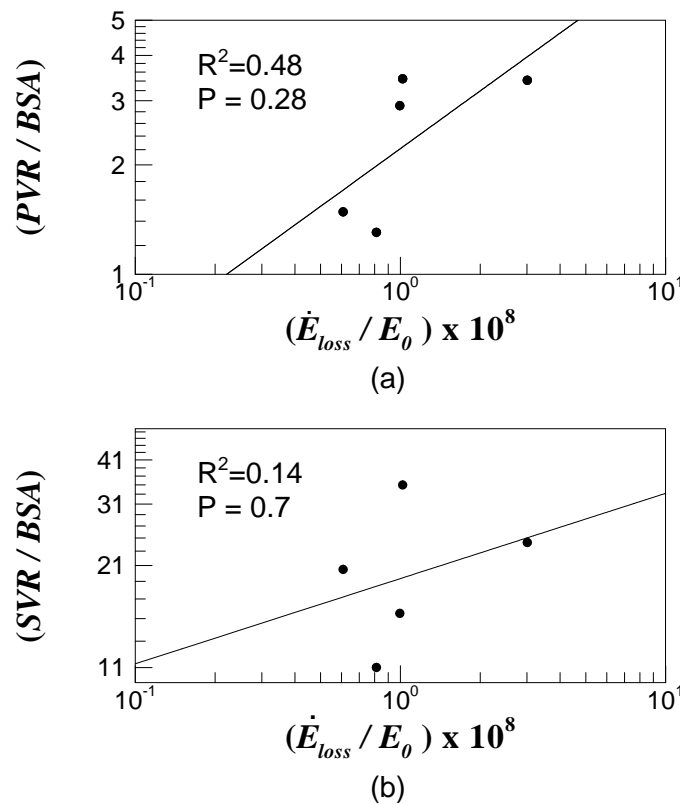
Figure 6.16: Normalized power loss ($\dot{E}_{loss}/E_0$) at the MRI flow split condition plotted against (a) pulmonary vascular resistance, PVR normalized with BSA and (b) systemic vascular resistance, SVR normalized with BSA

6.5 Clinical Significance

In this study, we showed that vessel diameter; especially pulmonary artery diameter, is the most influential among all the TCPC geometric parameters. Among the pulmonary arteries, LPA diameter was observed to have the highest correlation with power loss within the TCPC, while all other geometric characteristics had only secondary effects. The IVC curvature and IVC-SVC offsets did not impact the power loss as much as the PA diameter but are possibly beneficial in reducing the PA vessel narrowing by allowing enough blood flow through these vessels. However, orienting the IVC towards a stenosed PA causes higher power losses and lower the cardiac output from the ventricle. Hence a right balance between the two competing factors is necessary.

The geometrical comparison between the two commonly used TCPC templates, extra cardiac and intra atrial TCPCs, showed that of among all the geometric parameters, it is the minimum PA diameter that impacts the TCPC efficiency significantly. Hence, it is apparent that a critical step for the hemodynamic improvement of the TCPC hemodynamics is to correct the stenosis of pulmonary arteries. Indeed the presence or absence of stenosis was shown to have a much more drastic effect than the type of TCPC template retained. Such observation concurred with previous studies by Ryu et al. [Ryu, 2001] and De Zelicourt et al (De Zelicourt, 2005], which state that most of the power loss measured in the TCPC may be attributed to wall friction (which for a given flow rate will drastically increase with decreasing vessel diameter) rather than to the connection design.

In this study, the majority of the patients had LPA stenosis than RPA stenosis and among them a majority had also been diagnosed with hypoplastic left heart syndrome. As mentioned in the discussion section, the relation between those two symptoms may be attributed to the compression of the LPA by a larger-than-normal reconstructed aorta.

From the clinical data available for the patients in the Fontan database, 29 out of 56 HLHS patients were reported to have significant LPA stenosis (data as of March 2007). Thus surgeons should either optimize the aortic reconstructions providing ample space for LPA growth or use effective and permanent methods to repair the stenosis to make an efficient TCPC.

With respect to the impact of the TCPC on the ventricle, we have shown that the TCPC indeed makes a significant impact on ventricular function. LPA narrowing which only causes a few hundred milliwatts of power loss can in fact reduce the resting cardiac output by 50%. This will have a huge impact on the exercise capacities of these younger patients and thus significantly affect their quality of life. Also, hearts with a single functioning right ventricle (HLHS) need to work harder than hearts with a single functioning left ventricle (non-HLHS). So the impact of the TCPC could be greater in HLHS patients than their non-HLHA counterparts. This could also leads to low exercise tolerance in HLHS patients.

Since the geometrical characteristics of bi-lateral SVC models are similar to the other Fontans, the focus should be on where to connect the IVC with respect to the SVC. Previous findings show that that IVC should be connected in between the two SVC's for better lung perfusion [de Zelicourt 2006].

Breaking down the TCPC into a simpler set of geometrical parameters may be difficult as one could potentially neglect some of the most important factors. Correlation of geometric features and hemodynamic factors is thus a critical safe guard that assesses whether the parameter retained plays a significant role and whether an important parameter has been left out. Such an approach is very valuable to the growing surgical planning field. The basic idea behind the current surgical planning approach is to provide surgeons with a 3D representation of the 2nd stage anatomy and then allow

148

them to envision and test the efficiency of different possible configurations for the 3rd stage. Ideally, the geometric optimization of the 3rd stage could even be completely automated, with the surgeon only checking for the feasibility of the outputted solutions. However, given the complexity of the geometries considered and the range of possible surgical methods, optimization may be a very tedious process. By pinpointing which parameters should be initially optimized, this study may significantly ease the process. The geometrical parameters obtained in the pre and post pairs and their evolution through time, may also be very valuable when trying to model more realistic TCPCs and their evolution with time. Finally, the skeletonization tool described in this study may be used as a diagnostic tool, helping the clinicians quantify variations in the Fontan geometry and evaluate the patient's growth/performance.

CHAPTER 7

LIMITATIONS OF THE STUDY

Though the method of skeletonization proved to be useful in estimating the geometrical characteristics of complex TCPC anatomies, this method has certain limitations. This chapter presents those limitations.

7.1 Skeletonization

The key methodology that has been developed and implemented as a part of this study, "the skeletonization" technique is capable of estimating the centerline of the geometry and extracts its geometric characteristics. However this method has certain limitations that are described below.

7.1.1 Semi automatic Program

In its present form, this method is a semi-automatic program. User intervention is required to do the slicing, which is one of the key steps in performing the centerline calculation. Visualization software Tecplot (Tecplot Inc., Bellevue, WA) has to be used along with the execution of the 'C' program for two purposes: (1) to input the starting and end frames of the vessel for centerline computation; and (2) to make sure that no slice overlapping occurs and only appropriate slices are inputted to the program for iteration.

Another limitation is that batch processing of multiple input files is not feasible at this stage of the program, since user has to type in the input / output file names during

each iteration. Though the processing time of the program is less than a minute, user intervention makes the over all processing time longer.

7.1.2 Vessel Branching

The design of this program is such that a starting frame and an ending frame of the geometry have to be defined by the user for the centerline estimation. For a normal TCPC this is not a problem as we are interested in one vessel at a time for better comparison. However, estimating the centerline at the connecting point is still a problem with this method as it involves at least three vessels at a time. Also, this program is not efficient in estimating the centerlines of branched vessels like coronary arteries due to the same reason. So each vessel centerline has to be computed separately and merge together using Tecplot (or similar visualization software).

7.1.3 Accuracy

Though the accuracy of this method has been validated using idealized TCPC models, it depends heavily on the input slices. Hence it is necessary to make sure that no slice overlapping occurs during the geometric slicing. The overlapping occurs in cases where the vessel is curved or has a sudden change in its curvature. During such situations the user has to manually remove the overlapping slices to obtain a smooth centerline curve.

7.2 Geometric Analysis

The small sample size was an issue during the geometrical analysis, especially when comparing the geometric characteristics of the pre and post Fontan surgical pairs. Since only three dataset were available for this study, no statistical analysis could be

performed. This prevented us from drawing any clinical correlations. Similar was the case of bi-lateral SVC models in which only five models were available for analysis.

7.3 Hemodynamic Efficiency Analysis

Since this work was a retrospective study that uses the existing Fontan data base rather than a prospective study, not all the models selected for the geometrical analysis had all the hemodynamic parameters needed for specific aim 3, which was to correlate Fontan geometry with its hemodynamics. This resulted in uneven sample sizes for comparison of power loss (N = 15), cardiac index (N=26) and ventricular power output (N = 13) with the geometric parameters.

The relatively low sample size of the in-vitro energy loss experiments, ruled out a multivariate statistical analysis. However, we do show that the data are sufficient to show that the LPA size is the dominant variable, while all the other geometric parameters have second order effects. But with nine datasets, the CFD power loss showed that RPA vessel dimension is significantly correlated with the power loss. This points out that it is the minimum PA vessel dimension that is the main bottleneck. Addition of few more experimental data sets may strongly support this conclusion.

CHAPTER 8

CONCLUSIONS

In this study, details about the geometric parameters associated with Fontan anatomies, specifically the vessel cross-sectional areas, vessel offset and curvature are analyzed. These parameters help to us quantify the geometric features of the commonly used Fontan templates – extra cardiac TCPC, intra arial TCPC, pre Fontan anatomies and bi-lateral SVC. Also some of the important anatomic correlates of the TCPC efficiency are extracted out as a part of the analysis.

8.1 Skeletonization Method – Specific Aim 1

A method to compute the geometrical characteristics of complex TCPC anatomies such as vessel dimensions, vessel offset and curvature has been developed and successfully implemented as a part of this study. This technique uses the centerline approximation of geometries for computing the geometrical details. By pre-selecting the vessels that need to be processed, all the different Fontan templates irrespective of the number of vessels can be processed by this technique.

8.2 Characterization of Fontan Geometries – Specific Aim 2

Geometric characteristics of three types of Fontan templates were analyzed in this study. They are:

- o Extra cardiac and intra atrial geometries
  - ▪ HLHS vs. Non HLHS patients

153

- o Pre and post Fontan geometries

- o Bi-lateral SVC geometries

Since two types of TCPC anatomies, extra cardiacs and intra atrials, mainly dominate our database, these anatomies were analyzed in-depth. Comparison between the TCPC geometries of these two models showed that it is not the vessel cross-sectional area of the IVC baffle but the area variation across the vessel length is the significantly different parameter. Interpretation of the collinearity values suggests that the orientation of the IVC and SVC for intra atrials is in a more head on colliding manner than the extra cardiacs. Another major observation is the narrowing of the LPA compared to the RPA irrespective of their TCPC surgical type. Further investigation showed that this difference is more predominant in patients diagnosed with hypoplastic left heart syndrome (HLHS). This suggests that the narrowing of the LPA could be due to the aortic reconstruction performed during the 1st stage of the Fontan surgery in HLHS patients, which causes compression on the LPA.

From the three pre-post surgical pairs studied, a small reduction in the vessel cross sectional areas is noted for SVC and LPA. However, this could be due to the acute surgical trauma as detailed in the discussion section. No narrowing of the pulmonary arteries are observed before and after the TCPC surgery, which confirms the fact that LPA narrowing could be due to the aortic reconstruction performed in the 1st stage of Fontan.

The analysis of vessel cross sectional areas of bi-lateral SVC anatomies showed that the both RSVC and LSVC have same vessel areas. However, LSVC shows larger area variations than RSVC.

154

8.3 TCPC Geometry vs. Hemodynamics – Specific Aim 3

Among the various geometrical parameters analyzed, it was the minimum PA diameter of the TCPC that had the highest impact on TCPC efficiency. Both LPA and RPA when plotted against the experimental and CFD power losses respectively, showed significant correlation values (R^2=0.88 for LPA and R^2=0.78 for RPA). Further investigation using the minimum LPA diameters showed that, in addition to the TCPC efficiency, this vessel narrowing in fact also impacted the patient cardiac index and the ventricular power output. Since the results in this study correspond to resting cardiac output, the effect is expected to be even higher under exercise conditions. Another important observation is that for patients with HLHS the ventricular power out was greater than their non-HLHS counter parts. In conclusion, more attention should be given to the pulmonary artery sizes during the first stage of Fontan surgery so as to ensure better long-term TCPC performance.

CHAPTER 9

RECOMMENDATIONS FOR FUTURE WORK

In this study, we developed and implemented a skeletonization method to extract the geometric characteristics of complex TCPC anatomies. This methodology was applied to 34 Fontan patients selected from our patient database. Breaking down the complex patient-specific anatomies into a set of geometric parameters allowed us to quantitatively compare the different anatomies and pinpoint recurrent geometric features. These parameters were also correlated with a metrics for TCPC efficiency (power losses) thus isolating critical parameters for the improvement of the TCPC procedure. The first application demonstrated the strength and relevance of our approach for the hemodynamic analysis and optimization of the TCPC. This leads the way for future endeavors both technical, in order to improve the program's efficiency, and clinical, to further explore the intricacies of the TCPC anatomy. Both aspects are detailed in this chapter, starting with the technical development and then moving into future studies of the Fontan anatomies.

9.1 Technical Improvements to the Skeletonization Approach

9.1.1 Program Automation

The skeletonization program in its present form needs regular user intervention. The user has to manually enter the input and output file names for all iterations. Also, user intervention is needed to visually inspect the convergence of the centerlines calculated in two subsequent iterations. Although the execution time for the program is

less than 30 seconds, these user interventions increase the overall processing time. In order to further improve the efficiency of the over all procedure, this program can be fully automated using additional coding.

By modifying the existing program, input file names can be automatically plugged in to the code. By automatically updating the file names after each iteration, the need for manual data entry can be fully removed from the skeletonization protocol. Appropriate convergence criteria, like distance between the centroids of two consecutive iterations approaching zero, could be used to test the convergence of the centerline rather than visual inspection.

Thus, by fully automating the entire skeletonization (1) manual data entry can be avoided and (2) overall processing time can be substantially reduced (3) In addition, a fully automated code will enable batch processing applications, which will be a critical feature for large scale analysis of our anatomical database.

9.1.2 Processing multi branch vessels

The algorithm implemented in this study considers the geometry of interest as a stack of contiguous "slices" and computes the centerline as the line going through the center of mass of the vessel cross-section in each one of the "slices". That approach works well in most cases, but problems may arise if the geometry has multiple branches. Indeed, the "slices" required for the computations are obtained by intersecting the 3D anatomy with a plane. In certain cases, this plane may intersect two or more vessels, so that the corresponding "slice" will actually contain two or more vessel cross-sections. In the current implementation, the program does not have the ability to distinguish among these and will retain all cross-sections present for the subsequent centerline computation. Hence, unless the user intervenes, the program will yield an erroneous

centerline, which may even fall outside of the geometry. A potential solution may be to add selection criteria into the program that will allow the code to first detect that there are multiple distinct cross-sections present in the "slice" and then choose which one is the one that corresponds to the vessel of interest. Such procedure should overcome the issue of processing branched vessels thus yielding a more general code formulation and application as well as reducing the processing time by reducing the amount of user intervention and control.

9.2 Future Studies of the Fontan Anatomy

9.2.1 Evaluate Geometric Changes Over Time

The Fontan surgery is usually performed during the patients' early childhood. It will thus be interesting to look at the changes in the vessel dimensions and other related parameters like power loss and flow characteristics over the years as the child grows. In this study, an effort has been made to look into the pre- and post-Fontan stages of the same patient. This gave a first insight into how vessel dimensions evolve with time. However, since there were only 3 patient pairs available for the analysis, no strong conclusion could be made. It would thus be interesting to scan the same patients at multiple points in time so as to perform a detailed study on the evolution of the Fontan geometry. Time-points of interest could be (1) right before and right after the 3rd stage of the TCPC (pre/post pairs), (2) shortly after the surgery and a few month later to try and assess the impact of the magnitude of the acute response to the surgery and its impact on the hemodynamics, and/or (3) two time points after the surgery that would be separated by a few years to measure the growth and deformation of the surgical design

as the patient grows and assess how much control the surgeon truly has over the final TCPC geometry.

This study could be helpful in the development of the surgical planning tool, which is one of the major focuses of Fontan research, so as to make the tool more realistic by including the surgeon's preferences. This data can also be used for validating the surgical planning tool so as to see how the tool predicted a post Fontan using the pre Fontan model and see how well the prediction compared to that of the actual surgery performed by the surgeons.

9.2.2 TCPC Volume estimation

For majority of the geometric parameters of TCPC, especially for vessel dimensions, patient body surface area is used as the normalization factor. Though this parameter has been clinically accepted as the best available normalization quantity, a more appropriate choice will be the TCPC volume. Computational complications of this measurement are the major barrier. Since we are computing the vessel cross sectional areas as a part of the skeletonization process, obtaining the TCPC volume will not be a tedious task. Care should be given to keep uniform vessel length for all the geometries, which will otherwise affect the analysis. By specifying landmarks at fixed distance from the TCPC junction the uniformity in computation can be preserved.

9.2.3 Geometrical Analysis of Glenn vs. Hemi Fontan

One major study population that had to be left out from this analysis is the two surgical groups of 2nd stage Fontan anatomy – Glenn and Hemi Fontan. A major

limitation at the time of our study was the small number of 2nd stage patients that had been scanned and included in our database, and as a consequence the absence of efficiency metrics for these patients. With a database that has grown up to more than 10 patients in each category and the recent availability of experimental and CFD power losses for 2nd stage anatomies, an analysis similar to what was done in this thesis for intra-atrial and extra-cardiac TCPCs could now be conducted focusing on the 2nd stage rather than on the final one. This will be of great value, especially since the long-term objective of Fontan research revolves around surgical optimization and planning at each stage of the surgical procedure.

APPENDIX A

PROTOCOL FOR SKELETONIZATION

Entire process of skeletonization procedure that needs to be performed in order to obtain the centerline of TCPC geometries is described in this section. For clarity the whole process is defined in five separate sections (AA1 through AA5). The protocol for this procedure is described in the same order in which all the data has been processed for this work.

A1. Obtain Tecplot compatible 3D reconstructed anatomy

The method used for this skeletonization process involves slicing the geometry into thin frames. This slicing is performed in Tecplot using a macro. So the first step is to import the 3D TCPC geometry into the Tecplot.

Tecplot 360 is compatible with the .stl file (commonly used format for saving 3D reconstructed data). For all older versions of Tecplot, follow the given steps to create a .dat file, which can be opened in Tecplot. An executable program stl2dat.exe performs the stl to dat conversion.

1. Save the stl2dat.exe program and the input ASCII stl file in the same folder.

2. Go to the command mode of the machine

    a. Go to Run in the Start prompt and type "*cmd* "

    b. Go to the working directory using change directory command "*cd*"

3. Perform the format conversion by typing "*stl2dat   stlfilename.stl*"

4. Output dat file will be saved in the same folder as the input stl file, automatically.

A2. Geometry Slicing

Once the Tecplot compatible input files are ready, open them in the Tecplot to perform the slicing. Given below are the instructions for initial slicing.

1. There is a Tecplot macro written to perform the initial slicing. For convenience there are two separate macros for venae cavae (macro_for_SI_slicing) and pulmonary arteries (macro_for_RL_slicing). The two macros differ only in their slicing direction and their logic is the same.

2. Open the macro using Notepad and type in the input file name

3. The skeletonization program needs the user to input the starting and end frame of the geometry. An easy way to do this with TCPC models is, to find out the min and max ranges of z co-ordinate for the venae cavae, which is roughly parallel to the z axis and x co-ordinate for the pulmonary arteries, which is roughly parallel to the x axis using Tecplot.

4. Enter these minimum and maximum values for the slicing position in the appropriate macro depending on the vessel of interest. An example for slicing the pulmonary artery is shown below:

> VarSet |position| = *"minimum"*
>
> $!GLOBALSLICE SLICESURFACE = XPLANES
>
> $!GLOBALSLICE POSITION1{X = |position|}
>
> $!GLOBALTHREED SLICE{NORMAL{Z = 0}}
>
> $!GLOBALTHREED SLICE{NORMAL{X = 1}}
>
> $!GLOBALTHREED SLICE{NORMAL{y = 0}}
>
> $!While |position| <= *"maximum"*

5. Run the macro in Tecplot. The slices will be automatically saved in the out folder specified by the user. Also user will be able to visualize these slices in Tecplot.

A3. Skeleton and Area Computation - First Iteration

For the sake of clarity and simplicity, two programs are created for initial centroid computation and for further iterations. Please note that the logic of both programs is exactly same and the only   reason for having two separate programs is to avoid any confusion. Also this way it will be easy to keep track of the initial processing and subsequent iterations

1. Open the program for initial computation in Microsoft Visual Studio. The program is written in Microsoft Visual Studio 6.0

2. Enter the input filename, which is the file containing the slices generated in section AA2.

    a. User needs to enter the complete path for the input file

3. Similarly enter the output file names also. Since the program computes vessel cross sectional areas also, user can specify the type of output file (Ex: xls for Excel, txt for text etc) to store the area. An example of the input and output lines from the program is shown below:

    Input Slices: char *path_inputslices =

    {"C:\\Skeltonization\\Model1\\Model1_input_slices_iteration1.dat"};

    Output Centroid: char *path_outputslices =

    {"C:\\Skeltonization\\Model1\\Model1_output_centroid_iteration1.dat"};

    Output Area: char *path_outputslices =

    {"C:\\Skeltonization\\Model1\\Model1_output_area_iteration1.xls"};

A4. Iterative Slicing

Because the vessel axes are not always perpendicular to the co-ordinate axes, re-slicing of the geometry is needed to improve the accuracy of computation. This section explains the steps involved in doing this process.

1. The C program "generate macro for normal slicing" can create another Tecplot macro to improve the accuracy of geometry slicing. These slices will be in directions perpendicular to the centerline obtained from the first iteration.

2. User needs to enter the input file name, which will be the previously computed centerline and output file, which will be the Tecplot macro. An example is shown below:

> **Input Centroid**: char *centroid_in =
>
> {"C:\\Skeltonization\\Model1\\Model1_output_centroid_iteration_n-1.dat"};
>
> **Output Tecplot Macro**: char *macro_out =
>
> {"C:\\Skeltonization\\Model1\\Model1_output_macro_iteration_n.mcr"};

3. Run this program to get the Tecplot macro for normal slicing.

4. In Tecplot run the macro obtained in step 3 of this section AA4.

6. This creates slices that are roughly normal to the vessel of interest. User will be able to visualize these slices in Tecplot. However, in this step user has to save the slices manually. By doing so, user can make sure that any overlapping slices are removed from the list.

A5. Iterative Computation of Skeleton and Area

To improve the accuracy of computed centerline and cross-sectional area repeat the iterations until they converge as described below.

1. Obtain slices normal to the vessel axes as described in section AA4.

2. For centroid computation use the program for iteration.

3. Input the file names as explained in step 3 of section AA3.

4. Once the skeleton is obtained, visually compare it with the skeleton obtained from the previous iteration. If they are on top of each other, the process can be stopped. Other wise repeat section AA4 and AA5 until results from two iterations converge.

5. For further analysis save the final centroid and area files in the analysis folder.

APPENDIX B

RESULTS FOR FONTAN GEOMETRICAL ANALYSIS

The values corresponding to each model, which were used to compute different geometric parameters of the Fontan templates analyzed in this study, are provided in this appendix.

B1. Validation Studies for the Zero Offset Model

Slice Number	Length of centroid from the baffle_Iter1 (mm)	Area_Iteration1 (mm²)	Length of centroid from the baffle_Iter2 (mm)	Area_Iteration2 (mm²)
1.00	0.00	230.54	0.00	223.77
2.00	0.89	212.55	0.93	208.83
3.00	1.85	200.10	1.90	196.30
4.00	2.84	185.89	2.89	182.19
5.00	3.84	170.56	3.89	166.97
6.00	4.83	164.47	4.89	160.93
7.00	5.83	161.63	5.89	158.11
8.00	6.83	158.69	6.89	155.17
9.00	7.83	156.26	7.89	152.78
10.00	8.83	154.98	8.89	151.50
11.00	9.83	154.86	9.89	151.39
12.00	10.83	154.75	10.89	151.28
13.00	11.83	154.64	11.89	151.17
14.00	12.83	154.53	12.89	151.06
15.00	13.83	154.42	13.89	150.95
16.00	14.83	154.31	14.89	150.85
17.00	15.83	154.20	15.89	150.74
18.00	16.83	154.10	16.89	150.63
19.00	17.83	153.99	17.89	150.53
20.00	18.83	153.89	18.89	150.42
21.00	19.83	153.78	19.89	150.32
22.00	20.83	153.68	20.89	150.21
23.00	21.83	153.57	21.89	150.11
24.00	22.83	153.47	22.89	150.01
25.00	23.83	153.37	23.89	149.91
26.00	24.83	153.27	24.89	149.81
27.00	25.83	153.17	25.89	149.71
28.00	26.83	153.07	26.89	149.61

29.00	27.83	152.97	27.89	149.51
30.00	28.83	152.87	28.89	149.41
31.00	29.83	152.78	29.89	149.31
32.00	30.83	152.68	30.89	149.22
33.00	31.83	152.58	31.89	149.12
34.00	32.83	152.49	32.89	149.02
35.00	33.83	152.39	33.89	148.93
36.00	34.83	152.30	34.89	148.83
37.00	35.83	152.21	35.89	148.74
38.00	36.83	152.11	36.89	148.65
39.00	37.83	152.02	37.89	148.55
40.00	38.83	151.93	38.89	148.46
41.00	39.83	151.84	39.89	148.37
42.00	40.83	151.75	40.89	148.28
43.00	41.83	151.66	41.89	148.19
44.00	42.83	151.58	42.89	148.10
45.00	43.83	151.49	43.89	148.01
46.00	44.83	151.40	44.89	147.92
47.00	45.83	151.32	45.89	147.83
48.00	46.83	151.23	46.89	147.74
49.00	47.83	151.15	47.89	147.65
50.00	48.83	151.06	48.89	147.57
51.00	49.83	150.98	49.89	147.48
52.00	50.83	150.90	50.89	147.40
53.00	51.83	150.82	51.89	147.31
54.00	52.83	150.73	52.89	147.23
55.00	53.83	150.65	53.89	147.14
56.00	54.83	150.57	54.89	147.06
57.00	55.83	150.50	55.89	146.98
58.00	56.83	150.42	56.89	146.90
59.00	57.83	150.34	57.89	146.83
60.00	58.83	150.26	58.89	146.75
61.00	59.83	150.19	59.89	146.68
62.00	60.83	150.11	60.89	146.61
63.00	61.83	150.04	61.89	146.54
64.00	62.83	149.97	62.89	146.47
65.00	63.83	149.89	63.89	146.40
66.00	64.83	149.82	64.89	146.33
67.00	65.83	149.75	65.89	146.26
68.00	66.83	149.68	66.89	146.19
69.00	67.83	149.61	67.89	146.12
70.00	68.83	149.54	68.89	146.05
71.00	69.83	149.47	69.89	145.98
72.00	70.83	149.40	70.89	145.91
73.00	71.83	149.34	71.89	145.84
74.00	72.83	149.27	72.89	145.77
75.00	73.83	149.20	73.89	145.70
76.00	74.83	149.14	74.89	145.64
77.00	75.83	149.07	75.89	145.57
78.00	76.83	149.01	76.89	145.50

79.00	77.83	148.95	77.89	145.43
80.00	78.83	148.89	78.89	145.36
81.00	79.83	148.82	79.89	145.29
82.00	80.83	148.76	80.89	145.22
83.00	81.83	148.70	81.89	145.15
84.00	82.83	148.64	82.89	145.08
85.00	83.83	148.59	83.89	145.01
86.00	84.83	148.53	84.89	144.94
87.00	85.83	148.47	85.89	144.88
88.00	86.83	148.41	86.89	144.81
89.00	87.83	148.36	87.89	144.74
90.00	88.83	148.30	88.89	144.67
91.00	89.83	148.25	89.89	144.60
92.00	90.83	148.20	90.89	144.53
93.00	91.83	148.14	91.89	144.47
94.00	92.83	148.09	92.89	144.40
95.00	93.83	148.04	93.89	144.33

B2. Validation Studies for the Rotated Zero Offset Model

Slice Number	Length of centroid from the baffle_Iter1 (mm)	Area_Iteration1 (mm^2)	Length of centroid from the baffle_Iter2 (mm)	Area_Iteration2 (mm^2)
1.00	0.00	518.02	0.00	144.31
2.00	1.15	524.71	1.15	144.47
3.00	2.31	547.27	2.31	144.55
4.00	3.46	302.12	3.46	144.63
5.00	4.62	299.94	4.62	144.71
6.00	5.77	299.59	5.77	144.79
7.00	6.93	299.24	6.93	144.87
8.00	8.08	298.90	8.08	144.95
9.00	9.24	298.56	9.24	145.03
10.00	10.39	298.22	10.39	145.11
11.00	11.55	297.88	11.55	145.19
12.00	12.70	297.54	12.70	145.27
13.00	13.86	297.21	13.86	145.35
14.00	15.01	296.88	15.01	145.43
15.00	16.17	296.55	16.17	145.51
16.00	17.32	296.22	17.32	145.59
17.00	18.48	295.90	18.48	145.67
18.00	19.63	295.57	19.63	145.75
19.00	20.79	295.25	20.79	145.83
20.00	21.94	294.93	21.94	145.91
21.00	23.10	294.62	23.10	145.99
22.00	24.25	294.30	24.25	146.07
23.00	25.41	293.99	25.41	146.15
24.00	26.56	293.68	26.56	146.23

25.00	27.71	293.37	27.71	146.31
26.00	28.87	293.07	28.87	146.39
27.00	30.02	292.76	30.02	146.47
28.00	31.18	292.46	31.18	146.55
29.00	32.33	292.16	32.33	146.63
30.00	33.49	291.86	33.49	146.72
31.00	34.64	291.57	34.64	146.80
32.00	35.80	291.28	35.80	146.88
33.00	36.95	290.99	36.95	146.97
34.00	38.11	290.70	38.11	147.07
35.00	39.26	290.41	39.26	147.16
36.00	40.42	290.13	40.42	147.26
37.00	41.57	289.84	41.57	147.36
38.00	42.73	286.96	42.73	147.46
39.00	43.88	270.26	43.88	147.55
40.00	45.04	247.52	45.04	147.65
41.00	46.19	220.92	46.19	147.76
42.00	47.35	190.72	47.35	147.86
43.00	48.50	159.80	48.50	147.96
44.00	49.66	128.91	49.66	148.06
45.00	50.81	98.06	50.81	148.17
46.00	51.96	67.98	51.96	148.27
47.00	53.12	41.55	53.12	148.38
48.00	54.27	19.04	54.27	148.48
49.00	55.43	2.60	55.43	148.59
51.00	57.74	586.29	56.58	148.70
52.00	58.89	216.09	57.74	148.81
53.00	60.05	168.78	58.89	148.92
54.00	61.20	168.68	60.05	149.03
55.00	62.36	168.58	61.20	149.14
56.00	63.51	168.48	62.36	149.25
57.00	64.67	168.38	63.51	149.36
58.00	65.82	168.29	64.67	149.47
59.00	66.98	168.19	65.82	149.59
60.00	68.13	168.10	66.98	149.70
61.00	69.29	168.01	68.13	149.82
62.00	70.44	167.92	69.29	149.93
63.00	71.60	167.83	70.44	150.05
64.00	72.75	167.74	71.60	150.17
65.00	73.91	167.65	72.75	150.29
66.00	75.06	167.56	73.91	150.41
67.00	76.22	167.48	75.06	150.53
68.00	77.37	167.39	76.22	150.65
69.00	78.52	167.31	77.37	150.77
70.00	79.68	167.23	78.52	150.90
71.00	80.84	167.14	79.68	151.02
72.00	82.02	167.06	80.85	151.27
73.00	83.22	166.98	82.04	151.55
74.00	84.42	166.91	83.25	151.78

B3. IVC Area Characteristics for EC and IA Models

Model	IVC Centroid Length (mm)	IVC Mean Area (mm^2)	IVC Area Standard Deviation	IVC Minimum Area (mm^2)	IVC Maximum Area (mm^2)
Extra Cardiac					
CHOA007	51.13	141.55	12.58	110.69	161.23
CHOA008	42.81	370.99	19.03	296.77	391.81
CHOP006	57.76	202.57	42.03	145.92	281.00
CHOP007	68.82	410.43	16.37	361.61	427.40
CHOP013	54.33	229.92	35.17	166.27	288.58
CHOP067	33.63	182.22	30.90	143.87	251.43
CHOP088	43.94	402.08	35.69	319.98	451.96
CHOP089	34.28	316.91	19.47	284.60	349.58
CHOP090	40.65	314.66	31.45	278.82	399.94
CHOP091	37.56	367.33	78.48	162.49	459.31
CHOP095	48.00	200.99	18.18	176.11	266.77
CHOP116	54.11	435.13	17.70	409.96	459.19
CHOP085	34.62	330.89	24.78	273.26	372.06
Intra Atrial					
CHOA004	57.87	188.36	64.86	70.89	290.82
CHOA009	54.30	349.06	104.13	181.27	520.91
CHOA011	57.04	558.70	130.10	264.64	694.76
CHOP008	87.78	596.06	220.92	280.70	1005.91
CHOP018	58.23	275.38	53.06	186.47	360.62
CHOP030	71.43	335.15	74.13	222.19	430.57
CHOP034	48.77	335.40	132.23	147.29	546.14
CHOP037	60.88	356.33	139.32	163.46	580.43
CHOP068	38.93	337.05	57.08	234.54	419.72
CHOP073	49.93	602.95	74.74	464.73	760.22
CHOP092	46.68	325.66	18.51	299.39	356.55
CHOP096	50.84	258.54	38.32	222.99	365.56
CHOA027	57.75	372.11	92.33	254.79	526.02

B4. SVC Area Characteristics for EC and IA Models

Model	SVC Centroid Length (mm)	SVC Mean Area (mm^2)	SVC Area Standard Deviation	SVC Minimum Area (mm^2)	SVC Maximum Area (mm^2)
Extra Cardiac					
CHOA007	30.75	51.41	26.70	20.44	92.45
CHOA008	21.01	126.05	46.92	46.43	198.16
CHOP006	45.09	81.89	37.43	33.52	169.24
CHOP007	38.01	128.67	33.11	74.94	167.94
CHOP013	33.10	129.49	29.53	97.14	193.34
CHOP067	37.81	169.66	34.40	131.89	272.30
CHOP088	38.49	173.00	32.35	134.97	253.01
CHOP089	38.90	149.91	34.71	99.23	234.63
CHOP090	40.93	231.49	31.23	157.99	284.68
CHOP091	29.61	195.48	35.99	151.92	254.77
CHOP095	22.85	116.20	47.32	67.03	207.39
CHOP116	34.12	183.37	49.30	110.82	247.21
CHOP085	21.32	92.55	24.29	54.47	128.94
Intra Atrial					
CHOA004	27.10	81.56	21.64	47.42	113.04
CHOA009	28.93	119.60	27.56	56.70	145.96
CHOA011	36.77	127.00	49.41	77.07	234.60
CHOP008	49.41	156.28	34.56	100.46	196.95
CHOP018	57.54	111.22	28.42	82.33	168.75
CHOP030	44.62	120.74	29.76	76.14	179.87
CHOP034	41.02	102.10	33.01	54.68	173.25
CHOP037	46.71	118.64	16.78	69.44	139.19
CHOP068	28.68	95.26	24.25	71.01	133.73
CHOP073	41.70	128.27	51.48	54.86	190.40
CHOP092	32.84	118.35	34.63	72.02	175.75
CHOP096	42.36	124.69	28.96	83.83	196.97
CHOA027	16.05	152.39	8.06	129.52	159.89

B5. RPA Area Characteristics for EC and IA Models

Model	RPA Centroid Length (mm)	RPA Mean Area (mm^2)	RPA Area Standard Deviation	RPA Minimum Area (mm^2)	RPA Maximum Area (mm^2)
Extra Cardiac					
CHOA007	23.04	52.35	5.76	44.72	62.47
CHOA008	42.62	25.59	15.27	6.18	59.58
CHOP006	23.70	53.99	17.25	37.25	90.56
CHOP007	66.89	74.64	32.26	31.72	151.12
CHOP013	32.23	80.53	17.04	52.37	108.94
CHOP067	28.66	79.15	21.14	33.51	103.72
CHOP088	21.03	140.13	12.73	121.24	156.54
CHOP089	18.62	138.63	21.63	109.33	168.21
CHOP090	37.28	213.87	72.63	82.59	324.06
CHOP091	26.65	85.54	13.73	72.26	121.72
CHOP095	16.88	68.12	12.12	56.39	95.23
CHOP116	29.27	152.95	26.06	107.40	192.98
CHOP085	22.28	117.58	13.88	82.41	137.50
Intra Atrial					
CHOA004	23.34	52.92	7.45	42.26	65.05
CHOA009	16.11	66.57	29.41	25.78	105.32
CHOA011	35.96	132.40	34.03	72.72	186.22
CHOP008	30.46	82.41	27.82	27.24	133.10
CHOP018	47.31	161.84	58.78	108.24	276.69
CHOP030	37.40	99.99	17.65	62.00	129.20
CHOP034	40.42	92.86	18.66	68.48	137.25
CHOP037	33.58	96.44	30.64	50.20	138.77
CHOP068	26.95	84.59	8.91	68.24	101.77
CHOP073	30.83	155.84	56.41	84.46	263.19
CHOP092	28.57	98.73	14.97	66.65	114.91
CHOP096	20.29	115.46	8.32	100.47	124.83
CHOA027	21.88	159.40	42.57	111.87	243.77

B6. LPA Area Characteristics for EC and IA Models

Model	LPA Centroid Length (mm)	LPA Mean Area (mm^2)	LPA Area Standard Deviation	LPA Minimum Area (mm^2)	LPA Maximum Area (mm^2)
Extra Cardiac					
CHOA007	20.34	33.12	23.37	6.47	85.06
CHOA008	54.77	75.46	20.82	50.56	133.47
CHOP006	47.07	33.70	16.52	9.04	62.88
CHOP007	35.40	145.78	31.52	87.45	219.84
CHOP013	51.62	38.89	25.50	9.20	91.45
CHOP067	48.56	141.93	19.93	98.31	185.20
CHOP088	28.89	66.45	28.48	35.86	128.53
CHOP089	69.97	159.53	88.27	60.68	306.73
CHOP090	59.22	162.69	35.69	113.17	219.12
CHOP091	24.92	150.59	26.49	103.63	201.69
CHOP095	43.56	44.44	18.73	24.32	97.73
CHOP116	51.98	73.61	33.00	40.54	130.21
CHOP085	35.19	130.74	19.57	98.28	161.31
Intra Atrial					
CHOA004	35.06	72.36	37.41	12.59	137.67
CHOA009	34.28	48.92	17.84	19.55	90.40
CHOA011	52.09	80.18	16.91	55.28	134.83
CHOP008	63.72	27.55	25.37	3.73	128.70
CHOP018	51.97	100.26	62.29	28.09	253.79
CHOP030	57.92	166.48	48.04	95.71	280.28
CHOP034	67.82	153.43	67.23	73.05	274.15
CHOP037	45.89	148.24	64.24	85.74	289.20
CHOP068	42.71	80.17	15.32	55.65	137.08
CHOP073	53.94	102.88	49.71	54.82	255.90
CHOP092	44.29	38.39	23.26	14.25	77.94
CHOP096	39.59	57.63	25.10	33.12	132.71
CHOA027	30.15	103.73	32.66	68.47	166.63

B7. Vessel Area Ratios between VC and PA for EC and IA Models

Model	LPA/IVC	LPA/SVC	RPA/IVC	RPA/SVC
Extra Cardiac				
CHOA007	0.23	0.64	0.37	1.02
CHOA008	0.20	0.60	0.07	0.20
CHOP006	0.17	0.41	0.27	0.66
CHOP007	0.36	1.13	0.18	0.58
CHOP013	0.17	0.30	0.35	0.62
CHOP067	0.78	0.84	0.43	0.47
CHOP088	0.17	0.38	0.35	0.81
CHOP089	0.50	1.06	0.44	0.92
CHOP090	0.52	0.70	0.68	0.92
CHOP091	0.41	0.77	0.23	0.44
CHOP095	0.22	0.38	0.34	0.59
CHOP116	0.17	0.40	0.35	0.83
CHOP085	0.40	1.41	0.36	1.27
Intra Atrial				
CHOA004	0.38	0.89	0.28	0.65
CHOA009	0.14	0.41	0.19	0.56
CHOA011	0.14	0.63	0.24	1.04
CHOP008	0.05	0.18	0.14	0.53
CHOP018	0.36	0.90	0.59	1.46
CHOP030	0.50	1.38	0.30	0.83
CHOP034	0.46	1.50	0.28	0.91
CHOP037	0.42	1.25	0.27	0.81
CHOP068	0.24	0.84	0.25	0.89
CHOP073	0.17	0.80	0.26	1.21
CHOP092	0.12	0.32	0.30	0.83
CHOP096	0.22	0.46	0.45	0.93
CHOA027	0.28	0.68	0.43	1.05

B8. Vessel Curvatures and Collinearity for EC and IA Models

Model	IVC Curvature	SVC Curvature	LPA Curvature	RPA Curvature	IVC - SVC Collinearity
Extra Cardiac					
CHOA007	0.27	0.21	0.18	0.10	0.65
CHOA008	0.16	0.10	0.22	0.19	0.68
CHOP006	0.24	0.18	0.44	0.56	0.59
CHOP007	0.37	0.02	0.08	0.41	0.52
CHOP013	0.10	0.52	0.06	1.62	0.31
CHOP067	0.28	0.23	0.56	0.17	0.54
CHOP088	0.12	0.52	0.11	0.38	0.66
CHOP089	0.24	0.43	0.45	0.11	0.61
CHOP090	0.02	0.09	0.04	0.51	0.45
CHOP091	0.06	0.07	0.06	0.02	0.35
CHOP095	0.35	0.42	0.20	0.15	0.63
CHOP085	0.03	0.06	0.18	0.00	0.57
CHOP116	0.11	0.04	0.14	0.16	0.52
Intra Atrial					
CHOA004	0.05	0.31	0.35	0.04	0.73
CHOA009	0.18	0.13	0.19	0.34	0.63
CHOA011	0.06	0.03	0.03	0.13	0.30
CHOP008	0.29	0.09	0.04	0.11	0.55
CHOP018	0.12	0.04	0.11	0.09	0.30
CHOP030	0.19	0.26	0.17	0.21	0.25
CHOP034	0.65	0.62	0.27	0.31	0.34
CHOP037	0.16	0.05	0.12	0.04	0.70
CHOP068	0.58	0.15	0.31	0.30	0.37
CHOP073	0.36	0.23	0.23	0.16	0.31
CHOP092	0.18	0.19	0.06	0.03	0.33
CHOP096	0.32	0.03	0.06	1.03	0.18
CHOA027	0.05	0.24	0.17	0.16	1.21

B9. Vessel Offset for EC and IA Models

Model	AP offset (mm)	RL Offset (mm)	PA-VC Offset (mm)
Extra Cardiac			
CHOA007	2.28	3.35	5.42
CHOA008	10.48	9.70	7.53
CHOP006	2.01	2.50	10.72
CHOP007	4.62	3.49	6.66
CHOP013	1.05	4.33	5.52
CHOP067	3.28	1.76	8.23
CHOP085	1.63	3.81	8.82
CHOP088	5.94	2.72	7.61
CHOP089	1.56	2.56	7.61
CHOP090	1.32	7.39	3.86
CHOP091	0.03	0.65	6.86
CHOP095	2.21	4.72	3.66
CHOP116	3.15	7.88	8.69
Intra Atrial			
CHOA004	0.05	12.64	4.35
CHOA009	0.99	2.50	5.13
CHOA011	4.12	5.10	9.40
CHOA027	4.03	4.57	4.96
CHOP008	0.33	5.41	10.89
CHOP018	5.99	2.44	11.59
CHOP030	0.90	2.11	8.90
CHOP034	1.98	4.44	5.78
CHOP037	3.87	7.76	5.49
CHOP068	1.84	1.49	8.61
CHOP073	1.69	0.26	9.94
CHOP092	0.82	0.16	8.70
CHOP096	4.26	7.23	3.84

Bi-directional Glenn as the 2nd stage

Hemi-Fontan as the 2nd stage

B10. IVC Area Characteristics for Pre and Post Fontan Models

Model	IVC Centroid Length (mm)	IVC Mean Area (mm^2)	IVC Area Standard Deviation	IVC Minimum Area (mm^2)	IVC Maximum Area (mm^2)
Pair 1					
CHOA014	-	-	-	-	-
CHOA027	57.75	372.11	92.33	254.79	526.02
Pair 2					
CHOP053	-	-	-	-	-
CHOP055	53.49	301.65	29.27	209.06	350.42
Pair 3					
CHOP057	-	-	-	-	-
CHOP084	34.62	330.89	24.78	273.26	372.06

B11. SVC Area Characteristics for Pre and Post Fontan Models

Model	SVC Centroid Length (mm)	SVC Mean Area (mm^2)	SVC Area Standard Deviation	SVC Minimum Area (mm^2)	SVC Maximum Area (mm^2)
Pair 1					
CHOA014	19.70	110.66	10.76	86.55	126.64
CHOA027	16.05	152.39	8.06	129.52	159.89
Pair 2					
CHOP053	21.78	73.83	4.83	70.00	89.65
CHOP055	21.33	63.38	6.19	57.49	83.40
Pair 3					
CHOP057	18.97	173.56	17.26	152.83	210.75
CHOP084	21.32	92.55	24.29	54.47	128.94

B11.1 LSVC Area Characteristics for Pair2

Model	SVC Centroid Length (mm)	SVC Mean Area (mm^2)	SVC Area Standard Deviation	SVC Minimum Area (mm^2)	SVC Maximum Area (mm^2)
Pair 2					
CHOP053	21.88	103.59	11.09	88.43	118.69
CHOP055	21.18	96.53	5.02	89.27	104.21

B12. RPA Area Characteristics for Pre and Post Fontan Models

Model	RPA Centroid Length (mm)	RPA Mean Area (mm^2)	RPA Area Standard Deviation	RPA Minimum Area (mm^2)	RPA Maximum Area (mm^2)
Pair 1					
CHOA014	18.06	53.29	11.36	36.49	71.91
CHOA027	21.88	159.40	42.57	111.87	243.77
Pair 2					
CHOP053	21.25	128.61	17.21	91.55	148.72
CHOP055	21.44	126.18	25.35	76.15	183.09
Pair 3					
CHOP057	21.23	158.78	32.70	116.93	224.36
CHOP084	22.28	117.58	13.88	82.41	137.50

B13. LPA Area Characteristics for Pre and Post Fontan Models

Model	LPA Centroid Length (mm)	LPA Mean Area (mm^2)	LPA Area Standard Deviation	LPA Minimum Area (mm^2)	LPA Maximum Area (mm^2)
Pair 1					
CHOA014	33.82	35.05	36.15	6.71	112.54
CHOA027	30.15	103.73	32.66	68.47	166.63
Pair 2					
CHOP053	34.13	114.77	28.11	71.86	158.41
CHOP055	33.60	88.64	29.83	51.60	135.76
Pair 3					
CHOP057	33.38	145.03	29.23	104.96	185.81
CHOP084	35.19	130.74	19.57	98.28	161.31

B14. Vessel Curvatures for Pre and Post Fontans

Model	IVC Curvature	SVC Curvature	LSVC Curvature	LPA Curvature	RPA Curvature
Pair 1					
CHOA014	-	0.16	-	0.18	0.43
CHOA027	0.05	0.03	-	0.06	1.03
Pair 2					
CHOP053	-	0.19	0.03	0.31	0.22
CHOP055	0.21	0.10	0.01	0.57	0.13
Pair 3					
CHOP057	-	0.01	-	0.14	0.13
CHOP084	0.03	0.06	-	0.18	0.0001

B15: Experimental Power loss at Equal Pulmonary resistance and MRI cardiac output along with normalized minimum vessel areas

Model	Minimum Area LPA (mm^2)	Minimum Area RPA (mm^2)	Minimum Area IVC (mm^2)	Minimum Area SVC (mm^2)	BSA (m^2)	LPA min. area/BSA	RPA min. area/BSA	IVC min. area/BSA	SVC min. area/BSA	Q at MRI CO (L/min)	PL at MRI CO_eq.PR (mW)	Power Loss (PL x BSA^2/Q^3)
CHOA007	17.93	44.72	110.69	20.44	0.79	0.00002	0.00006	0.00014	0.00003	2.00	13.80	2.19 x10^8
CHOA008	50.56	6.18	296.77	46.43	0.69	0.00007	0.00001	0.00043	0.00007	2.00	5.44	6.57 x10^7
CHOP013	9.20	52.37	166.27	97.14	0.83	0.00001	0.00006	0.00020	0.00012	2.60	8.65	6.88 x10^7
CHOA009	19.55	25.78	181.27	56.70	0.58	0.00003	0.00004	0.00031	0.00010	2.00	9.70	8.28 x10^7
CHOA011	57.54	72.72	264.64	77.07	1.21	0.00005	0.00006	0.00022	0.00006	4.00	13.76	6.39 x10^7
CHOP034	73.05	68.48	147.29	54.68	1.19	0.00006	0.00006	0.00012	0.00005	4.00	13.24	5.95 x10^7

B16: Experimental Power loss at MRI flow split and MRI cardiac output along with normalized minimum vessel areas

Model	Minimum Area LPA (mm^2)	Minimum Area RPA (mm^2)	Minimum Area IVC (mm^2)	Minimum Area SVC (mm^2)	BSA (m^2)	LPA min. area/BSA	RPA min. area/BSA	IVC min. area/BSA	SVC min. area/BSA	Q at MRI CO (L/min)	PL at MRI CO_MRI flow split (mW)	Power Loss (PL x BSA^2/Q^3)
CHOA007	17.93	44.72	110.69	20.44	0.79	0.00002	0.00006	0.00014	0.00003	2.00	19.03	3.01 x10^8
CHOA008	50.56	6.18	296.77	46.43	0.69	0.00007	0.00001	0.00043	0.00007	2.00	6.72	8.12 x10^7
CHOP013	9.20	52.37	166.27	97.14	0.83	0.00001	0.00006	0.00020	0.00012	2.60	11.50	5.95 x10^7
CHOA009	19.55	25.78	181.27	56.70	0.58	0.00003	0.00004	0.00031	0.00010	2.00	11.94	1.02 x10^8
CHOA011	57.54	72.72	264.64	77.07	1.21	0.00005	0.00006	0.00022	0.00006	4.00	21.42	9.95 x10^7
CHOP034	73.05	68.48	147.29	54.68	1.19	0.00006	0.00006	0.00012	0.00005	4.00	14.59	6.55 x10^7

B17: Experimental Power loss at 50-50 flow split and MRI cardiac output along with normalized minimum vessel areas

Model	Minimum Area LPA (mm^2)	Minimum Area RPA (mm^2)	Minimum Area IVC (mm^2)	Minimum Area SVC (mm^2)	BSA (m^2)	LPA min. area/BSA	RPA min. area/BSA	IVC min. area/BSA	SVC min. area/BSA	Q at MRI CO (L/min)	PL at MRI CO_50% flow split (mW)	Power Loss (PL x BSA^2/Q^3)
CHOA007	17.93	44.72	110.69	20.44	0.79	0.00002	0.00006	0.00014	0.00003	2.00	19.03	3.01 x10^8
CHOA008	50.56	6.18	296.77	46.43	0.69	0.00007	0.00001	0.00043	0.00007	2.00	4.60	5.56 x10^7
CHOP013	9.20	52.37	166.27	97.14	0.83	0.00001	0.00006	0.00020	0.00012	2.60	135.99	7.04 x10^8
CHOA009	19.55	25.78	181.27	56.70	0.58	0.00003	0.00004	0.00031	0.00010	2.00	11.94	1.02 x10^8
CHOA011	57.54	72.72	264.64	77.07	1.21	0.00005	0.00006	0.00022	0.00006	4.00	13.26	6.16 x10^7
CHOP034	73.05	68.48	147.29	54.68	1.19	0.00006	0.00006	0.00012	0.00005	4.00	12.56	5.64 x10^7

B18: CFD Power loss at Equal Pulmonary resistance and MRI cardiac output along with normalized minimum vessel areas

Model	Minimum Area LPA (mm^2)	Minimum Area RPA (mm^2)	Minimum Area IVC (mm^2)	Minimum Area SVC (mm^2)	BSA (m^2)	LPA min. area/BSA	RPA min. area/BSA	IVC min. area/BSA	SVC min. area/BSA	Q at MRI CO (L/min)	PL at MRI CO_eq.PR (mW)	Power Loss (PL x BSA^2/Q^3)
CHOP018	28.09	108.24	186.47	82.33	1.23	0.00002	0.00009	0.00015	0.00007	3.10	7.79	8.00x10^7
CHOP022	55.50	49.35	102.91	49.82	1.01	0.00005	0.00005	0.00010	0.00005	2.95	4.85	3.92 x10^7
CHOP034	73.05	68.48	147.29	54.68	1.19	0.00006	0.00006	0.00012	0.00005	5.24	23.51	4.69 x10^7
CHOP037	85.74	50.20	163.46	69.44	1.49	0.00006	0.00003	0.00011	0.00005	4.10	13.56	8.89 x10^7
CHOP055	51.60	76.15	209.06	57.49	0.63	0.00008	0.00012	0.00033	0.00009	1.49	0.67	1.61 x10^7
CHOP067	98.31	33.51	143.87	131.89	1.06	0.00009	0.00003	0.00014	0.00012	3.75	63.12	2.75 x10^8
CHOP088	35.86	121.24	319.98	134.97	0.54	0.00007	0.00022	0.00059	0.00025	1.47	0.97	1.85 x10^7
CHOP089	60.68	109.33	284.60	99.23	0.87	0.00007	0.00013	0.00033	0.00011	2.64	2.84	2.39 x10^7
CHOP090	113.17	82.59	278.82	157.99	1.15	0.00010	0.00007	0.00024	0.00014	3.44	1.21	8.00 x10^6

B19: CFD Power loss at MRI flow split and MRI cardiac output along with normalized minimum vessel areas

Model	Minimum Area LPA (mm^2)	Minimum Area RPA (mm^2)	Minimum Area IVC (mm^2)	Minimum Area SVC (mm^2)	BSA (m^2)	LPA min. area/BSA	RPA min. area/BSA	IVC min. area/BSA	SVC min. area/BSA	Q at MRI CO (L/min)	PL at MRI CO_MRI flow split (mW))	Power Loss (PL x BSA^2 /Q^3)
CHOP018	28.09	108.24	186.47	82.33	1.23	0.00002	0.00009	0.00015	0.00007	3.10	18.56	1.91×10^8
CHOP022	55.50	49.35	102.91	49.82	1.01	0.00005	0.00005	0.00010	0.00005	2.95	7.53	6.08×10^7
CHOP034	73.05	68.48	147.29	54.68	1.19	0.00006	0.00006	0.00012	0.00005	5.24	43.57	8.70×10^7
CHOP037	85.74	50.20	163.46	69.44	1.49	0.00006	0.00003	0.00011	0.00005	4.10	18.83	1.24×10^8
CHOP055	51.60	76.15	209.06	57.49	0.63	0.00008	0.00012	0.00033	0.00009	1.49	0.9368	2.26×10^7
CHOP067	98.31	33.51	143.87	131.89	1.06	0.00009	0.00003	0.00014	0.00012	3.75	61.53	2.68×10^8
CHOP088	35.86	121.24	319.98	134.97	0.54	0.00007	0.00022	0.00059	0.00025	1.47	1.77	3.37×10^7
CHOP089	60.68	109.33	284.60	99.23	0.87	0.00007	0.00013	0.00033	0.00011	2.64	2.84	2.39×10^7
CHOP090	113.17	82.59	278.82	157.99	1.15	0.00010	0.00007	0.00024	0.00014	3.44	3.467	2.29×10^7

B20: CFD Power loss at 50-50 flow split and MRI cardiac output along with normalized minimum vessel areas

Model	Minimum Area LPA (mm^2)	Minimum Area RPA (mm^2)	Minimum Area IVC (mm^2)	Minimum Area SVC (mm^2)	BSA (m^2)	LPA min. area/BSA	RPA min. area/BSA	IVC min. area/BSA	SVC min. area/BSA	Q at MRI CO (L/min)	PL at MRI CO_50% flow split (mW)	Power Loss (PL x BSA^2/Q^3)
CHOP018	28.09	108.24	186.47	82.33	1.23	0.00002	0.00009	0.00015	0.00007	3.10	31.56	3.24 x10^8
CHOP022	55.50	49.35	102.91	49.82	1.01	0.00005	0.00005	0.00010	0.00005	2.95	5.83	4.71 x10^7
CHOP034	73.05	68.48	147.29	54.68	1.19	0.00006	0.00006	0.00012	0.00005	5.24	34.53	6.90 x10^7
CHOP037	85.74	50.20	163.46	69.44	1.49	0.00006	0.00003	0.00011	0.00005	4.10	25.61	1.68 x10^8
CHOP055	51.60	76.15	209.06	57.49	0.63	0.00008	0.00012	0.00033	0.00009	1.49	0.6819	1.65 x10^7
CHOP067	98.31	33.51	143.87	131.89	1.06	0.00009	0.00003	0.00014	0.00012	3.75	61.87	2.69 x10^8
CHOP088	35.86	121.24	319.98	134.97	0.54	0.00007	0.00022	0.00059	0.00025	1.47	0.83	1.58 x10^7
CHOP089	60.68	109.33	284.60	99.23	0.87	0.00007	0.00013	0.00033	0.00011	2.64	2.84	2.39 x10^7
CHOP090	113.17	82.59	278.82	157.99	1.15	0.00010	0.00007	0.00024	0.00014	3.44	1.3742	9.09 x10^6

B21: Vascular Resistance vs. Power Loss from CFD and Experimental Studies

Model	PVR	SVR	BSA (m²)	PVR/BSA	SVR/BSA	min.PA/BSA	PL at MRI CO_eq.PR flow split (mW)	PL at MRI CO_MRI flow split (mW)	PL at MRI CO_50% flow split (mW)
CHOP022	1.50	20.70	1.01	1.49	20.50	4.89×10^{-05}	$3.92 \times 10^{+07}$	$6.08 \times 10^{+07}$	$4.71 \times 10^{+07}$
CHOA007	2.7	19.2	0.79	3.42	24.30	2.27×10^{-05}	$2.19 \times 10^{+08}$	$3.01 \times 10^{+08}$	$9.41 \times 10^{+07}$
CHOA008	0.9	7.6	0.69	1.30	11.01	8.96×10^{-06}	$6.57 \times 10^{+07}$	$8.12 \times 10^{+07}$	$1.74 \times 10^{+07}$
CHOA009	2.0	20.3	0.58	3.45	35.00	3.37×10^{-05}	$6.88 \times 10^{+07}$	$1.02 \times 10^{+08}$	$3.18 \times 10^{+07}$
CHOA011	3.52	18.77	1.21	2.91	15.51	4.76×10^{-05}	$8.28 \times 10^{+07}$	$9.95 \times 10^{+07}$	$1.54 \times 10^{+08}$

B22: Inter-Personal Error Computed for the Point Where Vessel Meets the TCPC

Person	IVC			SVC			LPA			RPA		
	X	Y	Z	X	Y	Z	X	Y	Z	X	Y	Z
1	109.22	-101.60	-97.81	108.15	-98.57	-70.59	132.03	-102.19	-80.69	105.54	-87.22	-81.67
2	108.58	-102.14	-100.36	108.09	-98.34	-71.59	127.47	-99.25	-83.54	105.54	-87.22	-81.67
3	109.22	-101.60	-97.81	107.94	-98.19	-75.62	127.47	-99.25	-83.54	107.38	-87.75	-80.80
4	111.95	-99.60	-94.37	107.51	-97.62	-74.51	126.75	-98.44	-83.29	105.54	-87.22	-81.67
5	109.22	-101.60	-97.81	108.12	-98.76	-69.56	126.12	-97.60	-82.69	107.38	-87.75	-80.80
Mean	109.64	-101.31	-97.63	107.96	-98.29	-72.37	127.97	-99.34	-82.75	106.28	-87.43	-81.32
Difference	2.31	1.71	3.26	0.45	0.68	2.13	1.22	0.91	0.54	0.74	0.21	0.34
Error %	2.07	-1.72	-3.45	0.42	-0.69	-2.86	0.96	-0.92	-0.65	0.70	-0.24	-0.42

APPENDIX C

C PROGRAMS AND TECPLOT MACRO

All the programs and the macro files used to generate skeletals of the Fontan models area provided in this appendix. The macro files are given first followed by the C programs.

C1: Tecplot Macro for geometry slicing

This Tecplot macro is used to generate slices of a given geometry

```
#!MC 1000
# Macro for geometry slicing
# AUTHOR: RESMI KRISHNAN
# DATE; JUNE 2006

$!VarSet |MFBD| = "C:\skeletonization\Input\Model1"    Enter Input file name
$!VarSet |position| =-88   Enter initial slice position
$!GLOBALSLICE SLICESURFACE = XPLANES
$!GLOBALSLICE POSITION1{X = |position|}
$!GLOBALTHREED SLICE{NORMAL{Z = 0}}
$!GLOBALTHREED SLICE{NORMAL{X = 1}}
$!GLOBALTHREED SLICE{NORMAL{y = 0}}
$!While |position| <=-11 Enter final slice position
$!GLOBALSLICE POSITION1{X = |position|}
$!GLOBALTHREED SLICE{ORIGIN{X = |position|}}
$!CREATESLICEZONEFROMPLANE
  SLICESOURCE = SURFACEZONES
#!SLICESOURCE = VOLUMEZONES
```

```
 FORCEEXTRACTIONTOSINGLEZONE = YES


$!WRITEDATASET  " C:\skeletonization\Model1\slices_1.dat" Enter Output file name
  INCLUDETEXT = NO
  INCLUDEGEOM = NO
  INCLUDECUSTOMLABELS = NO
  ASSOCIATELAYOUTWITHDATAFILE = NO
  ZONELIST =  [2-|NUMZONES|]
  BINARY = NO
  USEPOINTFORMAT = YES
  PRECISION = 9
$!VarSet |position| += 1
 $!EndWhile
$!RemoveVar |position|
$!RemoveVar |MFBD|
```

C2: C Program for centroid and area computation

This C program computes the centroid and area of the slices from the initial slicing

```
//TITLE: PROGRAM TO CALCULATE THE CENTROID OF A FONTAN //GEOMETRY
//AUTHOR: RESMI KRISHNAN
//DATE; JUNE 2006


#include <stdio.h>
#include <conio.h>
#include <stdlib.h>
#include <string.h>
#include <math.h>

/* Input files to the program are the slices of the geometry and output is the centroid file.
   Resolution of the slices has been fixed as one tenth of the vessel radius */

char *path_RL_slices = {"C:\\Documents and Settings\\resmi\\Desktop\\Resmi\\CFD
Velocity Registration\\0doffset\\V1slices_0doffset_rotate.dat"};
```

188

```
//char *path_SI_slices = {"C:\\Documents and Settings\\resmi\\Desktop\\Resmi\\CFD
Velocity Registration\\0doffset\\V3slices_0doffset_rotate.dat"};
char *path_LR = {"C:\\Documents and Settings\\resmi\\Desktop\\Resmi\\CFD Velocity
Registration\\0doffset\\V1_centroid_0doffset_rotate.dat"};
char *path_RL = {"C:\\Documents and Settings\\resmi\\Desktop\\Resmi\\CFD Velocity
Registration\\0doffset\\V1_centroid_other_0doffset_rotate.dat"};
//char *path_SI = {"C:\\Documents and Settings\\resmi\\Desktop\\Resmi\\CFD Velocity
Registration\\0doffset\\V3_centroid_0doffset_rotate.dat"};
//char *path_IS = {"C:\\Documents and Settings\\resmi\\Desktop\\Resmi\\CFD Velocity
Registration\\0doffset\\V3_centroid_other_0doffset_roatate.dat"};




//char *path_SI_slices = {"C:\\Documents and Settings\\resmi\\Desktop\\Resmi\\CFD
Velocity Registration\\Hemi Vs Glenn\\chop036\\SVCslices_p36.dat"};
//char *path_IS = {"C:\\Documents and Settings\\resmi\\Desktop\\Resmi\\CFD Velocity
Registration\\Hemi Vs Glenn\\chop036\\SVC_centroid_p36.dat"};
//char *path_SI = {"C:\\Documents and Settings\\resmi\\Desktop\\Resmi\\CFD Velocity
Registration\\Hemi Vs Glenn\\chop036\\SVC_centroid_other_p36.dat"};


const int DEBUG=1;
int  num_slice=0,elements[2000];

typedef struct Point{
     double x,y,z;
                 Point *P1,*P2;
} Point;

typedef struct Slice{
         int NUM;
    Point *points;
         Point avg_point;

} Slice;



//functions
void load_slicepoints(char *path);
void initialize_slices(char *path);
double get_centroid(Slice *S, Point *C);   //function that take slices and returns centroid
Point * find_closest_point(Point *C,Slice *S);
double distance(Point *X, Point *Y);
double get_triangle_center(Point *A, Point *B, Point *C, Point *center);
void skelitalize(char *path,char *outfile1, char *outfile2);
void release_slices();



Slice *slices;
```

```c
/* Main program starts here
   -----------------------
*/

void main() {

        skelitalize(path_RL_slices,path_LR,path_RL);
        //getch();
        //skelitalize(path_SI_slices,path_SI,path_IS);
        exit(0);
}



void skelitalize(char *path, char *outfile1, char *outfile2){
    Point center;
        int i,FLAG;
        FILE *out;
        double area=0.0;

        initialize_slices(path);
        load_slicepoints(path);
        printf("Number of slices: %d\n",num_slice);

        if(slices[0].points[0].x != slices[0].points[1].x) FLAG = 1; else FLAG = 0;

        out = fopen(outfile1,"w");
        //from last slice to first slice
        for(i=1;i<=num_slice;i++) {
                if(i==1 && FLAG == 0) {
                        center.y = slices[num_slice-1].avg_point.y;
                        center.z = slices[num_slice-1].avg_point.z;

                }
                if(i==1 && FLAG == 1) {
                        center.y = slices[num_slice-1].avg_point.y;
                        center.x = slices[num_slice-1].avg_point.x;

                }
                if(FLAG==0) center.x = slices[num_slice-i].points[0].x;
                if(FLAG==1) center.z = slices[num_slice-i].points[0].z;
                area = get_centroid(&(slices[num_slice-i]),&center);
                fprintf(out,"%lf %lf %lf\n",center.x,center.y,center.z);
        }
        fclose(out);

        out = fopen(outfile2,"w");
        //from first slice to last slice
        for(i=0;i<num_slice;i++) {
                if(i==0 && FLAG == 0) {
                        center.y = slices[0].avg_point.y;
```

```c
                center.z = slices[0].avg_point.z;

            }
            if(i==0 && FLAG == 1) {
                    center.y = slices[0].avg_point.y;
                    center.x = slices[0].avg_point.x;

            }
            if(FLAG == 0) center.x = slices[i].points[0].x;
            if(FLAG == 1) center.z = slices[i].points[0].z;
            area = get_centroid(&(slices[i]),&center);
            fprintf(out,"%lf %lf %lf\n",center.x,center.y,center.z);
    }
    fclose(out);


    release_slices(); //To save memory
}


// Centroid calculation is done here

double get_centroid(Slice *S, Point *C){
    double triangle_area,sum_area;
    Point *closest_point,*current_point,*next_point;
    Point *triangle_centroid,*temp;  /*triangle_centers*/
    Point slice_centroid;
    int count,first_time;

    closest_point = find_closest_point(C,S);
    current_point = closest_point;
    next_point = current_point->P1;
    count = 0;

    triangle_centroid = (Point *)malloc(sizeof(Point));

    slice_centroid.x = 0.0;
    slice_centroid.y = 0.0;
    slice_centroid.z = 0.0;
    sum_area = 0.0;
    first_time = 1;

    while((current_point != closest_point) || (first_time == 1)) {
            triangle_area =
get_triangle_center(C,current_point,next_point,triangle_centroid);
            slice_centroid.x += triangle_area*triangle_centroid->x;
            slice_centroid.y += triangle_area*triangle_centroid->y;
            slice_centroid.z += triangle_area*triangle_centroid->z;
            sum_area += triangle_area;
            temp = current_point;
            current_point= next_point;
```

```c
            if(next_point->P1 != temp) { next_point = next_point->P1;}
            else {next_point = next_point->P2;}
            first_time = 0;
    }

    slice_centroid.x /= sum_area;
    slice_centroid.y /= sum_area;
    slice_centroid.z /= sum_area;

    C->x = slice_centroid.x;
    C->y = slice_centroid.y;
    C->z = slice_centroid.z;
    printf("Centroid: %lf %lf %lf\nSlice Area: %lf\n",C->x,C->y,C->z,sum_area);
    return sum_area;
}


// Next 3 functions calculate the centroid of each triangles in the specific slices, its
closest points and distance b/w 2 points

double get_triangle_center(Point *A, Point *B, Point *C, Point *center) {
    double a,b,c,s,area;
    a = distance(A,B);
    b = distance(B,C);
    c = distance(A,C);
    s = (a+b+c)/2;
    area = sqrt(s*(s-a)*(s-b)*(s-c));
    center->x = (A->x+B->x+C->x)/3.0;
    center->y = (A->y+B->y+C->y)/3.0;
    center->z = (A->z+B->z+C->z)/3.0;

    return area;
}

Point *find_closest_point(Point *C,Slice *S) {
    int i;
    double temp,dist = 1.0E100;
    Point *closest_point;
    for(i=0;i<elements[(S->NUM)-1];i++) {
            if((temp=distance(C,&(S->points[i]))) <= dist ) {
                    dist = temp;
                    closest_point = &(S->points[i]);
                    printf("%lf %lf %lf %lf\n",closest_point->x,closest_point-
>y,closest_point->z,dist);
            }
    }
    return closest_point;
}


double distance(Point *X, Point *Y)
```

```c
{
        double out;
        out = sqrt(pow((X->x-Y->x),2)+pow((X->y-Y->y),2)+pow((X->z-Y->z),2));
        return out;
}

// Initialise the slices for the program

void initialize_slices(char *path){
     FILE *in;
        char word[200];
        int  i=0,j=0;
        in = fopen(path,"r");
        while(!feof(in)){
                        fscanf(in,"%s",word);
                        if(strcmp(word,"ZONE") == 0){
                          num_slice++;
                        }
                        else if(word[0]=='N' && word[1]=='=') {
            sscanf(&(word[2]),"%d",&(elements[num_slice-1]));
                        }
        }
        fclose(in);

        for(i = 0;i<num_slice;i++)
                        printf("Slice =%d \tELEMENTS =%d \n",i+1,elements[i]);
        slices = (Slice*)malloc(num_slice*sizeof(Slice));
        for(i = 0;i<num_slice;i++){
                slices[i].points = (Point*)malloc(elements[i]*sizeof(Point));
                for(j=0;j<elements[i];j++) {
                        slices[i].points[j].P1 = NULL;
                        slices[i].points[j].P2 = NULL;
                }
        }


}

void release_slices() {
        int i;
         for(i = 0;i<num_slice;i++)  free(slices[i].points);
        free(slices);
        num_slice = 0;
}

// Load each slice points to the memory along with the information on its neighboring
points

void load_slicepoints(char *path){
    FILE *in;
        Point avg;
```

```
        int p,c1,c2,j,i;
        int count = 0, count1 = 0;
        double x,y,z;
        char word[200];
        in=fopen(path,"r");
  if(DEBUG==1) printf("%s\n",path);
        while(!feof(in)) {
                p=fscanf(in,"%lf%lf%lf\n",&x,&y,&z);
                if(p=3){
                        count1++;
                        if(count1<=elements[count-1]){
                                slices[count-1].points[count1-1].x = x;
                                slices[count-1].points[count1-1].y = y;
                                slices[count-1].points[count1-1].z = z;
                                if(count1 == elements[count-1]) {
                                        for(i=0;i<elements[count-1];i++) {
                                                fscanf(in,"%d%d\n",&c1,&c2);
                                                if(slices[count-1].points[c1-1].P1 == NULL)
slices[count-1].points[c1-1].P1 = &(slices[count-1].points[c2-1]);
                                                else slices[count-1].points[c1-1].P2 =
&(slices[count-1].points[c2-1]);
                                                if(slices[count-1].points[c2-1].P1 == NULL)
        slices[count-1].points[c2-1].P1 = &(slices[count-1].points[c1-1]);
                                                else slices[count-1].points[c2-1].P2 =
&(slices[count-1].points[c1-1]);
                                        }
                                }
                        }

                }
                else {
                        fscanf(in,"%s",word); printf("%s\n",word);
                        if(strcmp(word,"ZONE") == 0){
                          count++; count1=0;
                          slices[count-1].NUM = count;
                        }
                }
        }
        fclose(in);

        for(i=0;i<num_slice;i++) {
                avg.x = 0;
                avg.y = 0;
                avg.z = 0;
                for(j=0;j<elements[slices[i].NUM-1];j++) {
                        avg.x += slices[i].points[j].x;
                        avg.y += slices[i].points[j].y;
                        avg.z += slices[i].points[j].z;
                }
                slices[i].avg_point.x = avg.x/elements[slices[i].NUM-1];
                slices[i].avg_point.y = avg.y/elements[slices[i].NUM-1];
```

```
                    slices[i].avg_point.z = avg.z/elements[slices[i].NUM-1];
        }

}
```

/***END***/

C3: C Program for generating macro for normal slicing

This C program re-slices the geometry in directions perpendicular to the geometry axes.

```
//TITLE: PROGRAM TO GENERATE TECPLOT MACRO TO DO SLICING OF FONTAN
GEOMETRYBASED ON THE NORMAL VECTORS OF CENTROID POINTS WE GET
FROM 1ST ITERATION
//AUTHOR: RESMI kRISHNAN
//DATE; SEPTEMBER 2006


#include <stdio.h>
#include <math.h>
#include <conio.h>
#include <stdlib.h>

/* Input files to the program are the geometry centroid we got from 1st iteration and
output is the macro for getting slices for next iterations.
   Resolution of the slices has been fixed as one tenth of the vessel radius */

char *centroid_in = {"C:\\Documents and Settings\\resmi\\Desktop\\Resmi\\CFD Velocity
Registration\\0doffset\\V1_centroid_other_0doffset_rotate.dat"};
char *macro_out = {"C:\\Documents and Settings\\resmi\\Desktop\\Resmi\\CFD Velocity
Registration\\0doffset\\V1_0doffset_rotate_normalslice_macro1.mcr"};

//char *centroid_in = {"C:\\Documents and Settings\\resmi\\Desktop\\Resmi\\CFD
Velocity Registration\\Hemi Vs Glenn\\chop036\\SVC_centroid_other_p36_iter2.dat"};
//char *macro_out = {"C:\\Documents and Settings\\resmi\\Desktop\\Resmi\\CFD Velocity
Registration\\Hemi Vs Glenn\\chop036\\SVC_p36_normalslice_macro2.mcr"};
```

```c
int slice_num=0;

typedef struct Point{
        double x,y,z;
} Point;

Point *centroid;

//Functions

void write_macro(char *outfile);
void load_initial_centroid(char *filein);


/* Main program starts here
   -----------------------
*/

void main(){

        load_initial_centroid(centroid_in);
        getch();
        write_macro(macro_out);
}


// Tecplot macro has been written here

void write_macro(char *outfile){

        FILE *macro;
    double vector_mag;

        macro = fopen(outfile,"a");

        //To get the slicing correctly go till N-2, N is the number of slices
        for(int i=0; i<=slice_num-2; i++){

                vector_mag = sqrt(pow((centroid[i+1].x -
centroid[i].x),2)+pow((centroid[i+1].y - centroid[i].y),2)+pow((centroid[i+1].z -
centroid[i].z),2));

/*              fprintf(macro,"#!MC 1000\n");
                fprintf(macro,"$!VarSet |MFBD| = 'C:\\Program Files\\TEC100'\n");
                fprintf(macro,"$!GLOBALTHREED SLICE{ORIGIN{X =
%lf}}\n",centroid[i].x);
                fprintf(macro,"$!GLOBALTHREED SLICE{ORIGIN{Y =
%lf}}\n",centroid[i].y);
                fprintf(macro,"$!GLOBALTHREED SLICE{ORIGIN{Z =
%lf}}\n",centroid[i].z);
```

```c
            fprintf(macro,"$!GLOBALTHREED SLICE{NORMAL{X =
%lf}}\n",(centroid[i+1].x - centroid[i].x)/vector_mag);
            fprintf(macro,"$!GLOBALTHREED SLICE{NORMAL{Y =
%lf}}\n",(centroid[i+1].y - centroid[i].y)/vector_mag);
            fprintf(macro,"$!GLOBALTHREED SLICE{NORMAL{Z =
%lf}}\n",(centroid[i+1].z - centroid[i].z)/vector_mag);
            fprintf(macro,"$!CREATESLICEZONEFROMPLANE \n");
            fprintf(macro,"  SLICESOURCE = SURFACEZONES\n");
            fprintf(macro,"  FORCEEXTRACTIONTOSINGLEZONE = YES\n");
            fprintf(macro,"$!RemoveVar |MFBD|\n\n\n");

*/


            // Taking the average of 2 centroid points to get the slice, which will give a
2nd order accuracy for slicing

            fprintf(macro,"#!MC 1000\n");
            fprintf(macro,"$!VarSet |MFBD| = 'C:\\Program Files\\TEC100'\n");
            fprintf(macro,"$!GLOBALTHREED SLICE{ORIGIN{X =
%lf}}\n",(centroid[i].x + centroid[i+1].x) /2);
            fprintf(macro,"$!GLOBALTHREED SLICE{ORIGIN{Y =
%lf}}\n",(centroid[i].y + centroid[i+1].y) /2);
            fprintf(macro,"$!GLOBALTHREED SLICE{ORIGIN{Z =
%lf}}\n",(centroid[i].z + centroid[i+1].z) /2);

            fprintf(macro,"$!GLOBALTHREED SLICE{NORMAL{X =
%lf}}\n",centroid[i+1].x - centroid[i].x);
            fprintf(macro,"$!GLOBALTHREED SLICE{NORMAL{Y =
%lf}}\n",centroid[i+1].y - centroid[i].y);
            fprintf(macro,"$!GLOBALTHREED SLICE{NORMAL{Z =
%lf}}\n",centroid[i+1].z - centroid[i].z);
            fprintf(macro,"$!CREATESLICEZONEFROMPLANE \n");
            fprintf(macro,"  SLICESOURCE = SURFACEZONES\n");
            fprintf(macro,"  FORCEEXTRACTIONTOSINGLEZONE = YES\n");
            fprintf(macro,"$!RemoveVar |MFBD|\n\n\n");


        }
fclose (macro);
}



// Centroid from first iteration is loaded to memory here

void load_initial_centroid(char *filein){
        FILE *in;
        int test=0;
        double x,y,z;
```

197

```c
        centroid = (Point*)malloc(2000*sizeof(Point));

        in = fopen(filein,"r");
        while(!feof(in)){
                test = fscanf(in,"%lf %lf %lf\n",&x,&y,&z);
                if (test == 3){
                        centroid[slice_num].x = x;
                        centroid[slice_num].y = y;
                        centroid[slice_num].z = z;
                        slice_num++;
                        printf("%lf %lf %lf \n", x,y,z);
                }
        }
                printf("Count : %d \n",slice_num);
}


/******************************************************END****************************************************/
```

APPENDIX D

EQUAL PULMONARY RESISTANCE CALCULATION

For experimental and CFD study cases, an important test condition to be analyzed is the situation where both the right and left lungs have equal pulmonary resistance (eq.PR). The method that we use to compute eq.PR for the TCPC in our laboratory is detailed in this section.
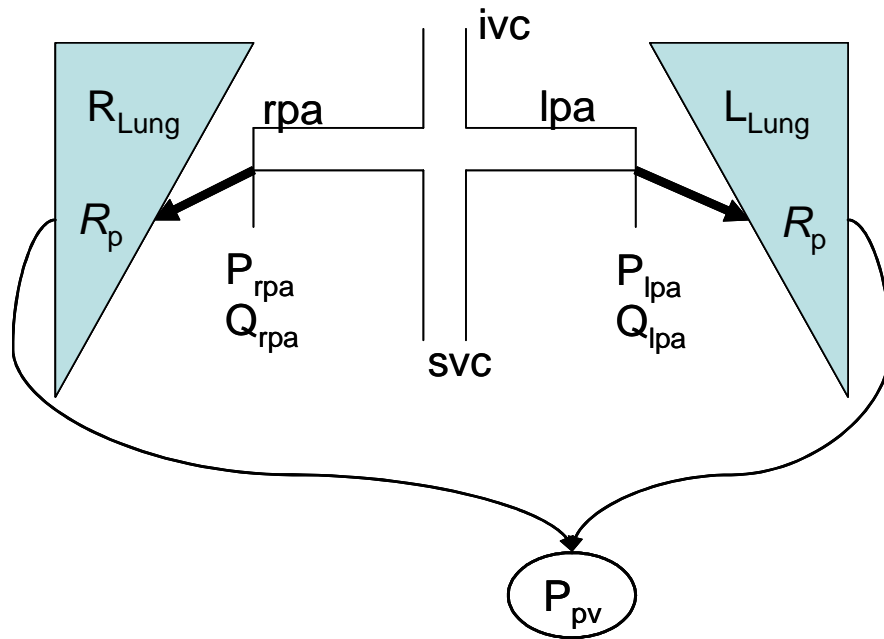

Figure D1: Schematic showing the set up to compute equal pulmonary resistance along with the notations used in this document. P is the pressure in mm HG, Q is the flow rate in L/min, and Rp is the pulmonary resistance.

D.1 Equal Pulmonary Resistance Calculation

As mentioned above, an uncontrolled, steady-state circulation with equal left and right lung properties is assumed in this case. For our studies, we assume both lungs to have a similar resistance: pulmonary resistance R_p is set to be 1.8mmHg/(L/min) [DeZelicourt, 2005]. Arterial and pulmonary compliances are neglected.

Then the pressure in each lung can be written using Darci's relation as:

$$P_{rpa} = P_{pv} + R_p \cdot Q_{rpa} \tag{D.1}$$

$$P_{lpa} = P_{pv} + R_p \cdot Q_{lpa} \tag{D.2}$$

where, P_{rpa} and P_{lpa} are the pressures in the right and left lungs, Q_{lpa} and Q_{rpa} are the flow rates of the left and right pulmonary arteries, R_p is the pulmonary resistance and P_{pv} is the pressure in the pulmonary venous return.

Pressure difference between the two pulmonary artery branches can then be found by subtracting equation (D.2) from (D.1). The resulting equation is a function of right pulmonary flow rate for a given total cardiac output Q_T.

$$P_{lpa} - P_{rpa} = R_p \cdot \left(Q_T - 2 \cdot Q_{rpa} \right) \tag{D.3}$$

From power loss experiments or CFD calculations we can also obtain the pressure difference between left and right pulmonary arteries and plot it as a function of Q_{rpa}. This experimental curve, which is a characteristic of the TCPC and Equation (D.3) are both linear. When plotted together, they intersect at a single point which gives the Q_{rpa} for the same lung resistances. A sample graph obtained by plotting Q_{rpa} vs. the pressure difference between left and right pulmonary arteries is shown in Figure D.2.
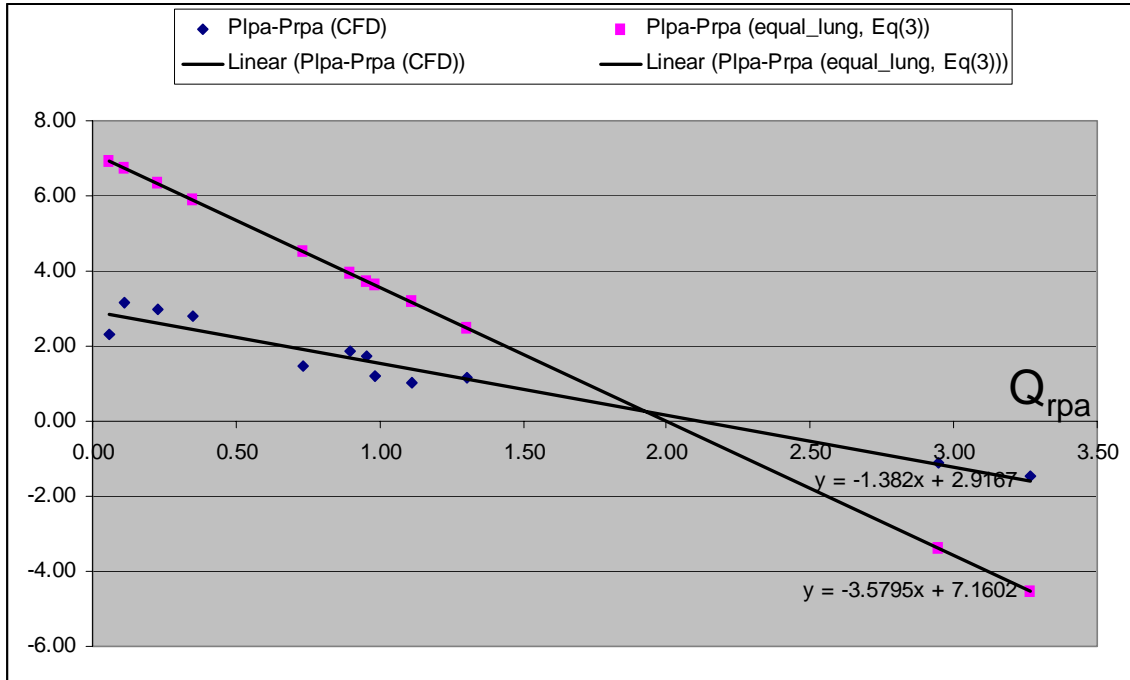
Figure D.2: Plot used to calculate eq.PR for the standard one-diameter offset model using CFD results. Here the Equal Lung Resistance condition is found to be at 48% (Q_{rpa}/Q_T). This operation point varies little with different lung resistance.

As seen in the figure AD.2 the linear regression should have a negative slope; i.e, more

flow to the LPA, which means the difference will be more negative.

From this plot you get the equation $P_{lpa} - P_{rpa} = B + A(Q_{lpa} / Q_T)$

where A and B are the slope and the intercept of the regression line seen in figure AD2.

Solving for Q_{lpa}, we get:

$$Q_{lpa} = (B + Rp\ Q_T) / (2Rp + (A/ Q_T))$$

Then Q_{rpa} is just Q_T - Q_{lpa}

Make sure that all dimensions are in the same unit system.

Though this above detailed method is commonly used to compute eq.PR, there could be

some confusion about the whole eq.PR calculations. (1) Darcy's law (P=QR) assumes

porous material structure for the left atrium and lungs. However, this assumption could be questioned as there is still some large veins and arteries involved in the model. Since the nonlinearity brought by the large vessels on the linear pressure drop term (P=QR) is negligible compared to the huge Darcy resistance there is no problem in assuming this linear relationship. This brings up another question as to why not use the total pressure (static pressure + kinetic pressure) for computation instead of using just the static pressure? The answer is that we compute the resistance in terms of Wood's unit, and the pressure calibrations for this unit are based on the static pressure measurements. Hence there is no need to include the kinetic component.

REFERENCES

Amodeo, A., L. Galletti, S. Marianeschi, S. Picardo, S. Giannico, P. Di Renzi, and C. Marcelletti, Extracardiac Fontan operation for complex cardiac anomalies: seven years' experience: J Thorac Cardiovasc Surg, 1997; 114 (6): 1020-30.

Anderson, R. N., and B. L. Smith, Deaths: leading causes for 2001: Natl Vital Stat Rep, 2003; 52 (9): 1-85.

Antiga L and Steinman DA. Robust and Objective Decomposition and Mapping of Bifurcating Vessels. IEEE Trans on medical imaging, 2004;23(6):704-13.

Be'eri E, Maier SE, Landzberg MJ, Chung T, Geva T. In vivo evaluation of Fontan pathway flow dynamics by multidimensional phase-velocity magnetic resonance imaging. Circulation. 1998;98(25):2873-82.

Blalock, A., and H. B. Taussig, The surgical treatment of malformations of the heart in which there is pulmonary stenosis or pulmonary atresia: J. Amer. Med. Assoc., 1945; 128: 189-202.

Blum, H., 1967. A transformation for extracting new descriptors of shape. In: Models for the Perception of Speech and Visual Form. MIT Press, Cambridge, MA, pp. 362–380.

Buckingham E. On physically similar systems, illustrations of the use of dimensional equations. Physical Review. 1914;4:345-76.

de Leval, M. R., G. Dubini, F. Migliavacca, H. Jalali, G. Camporini, A. Redington, and R. Pietrabissa, Use of computational fluid dynamics in the design of surgical procedures: application to the study of competitive flows in cavo-pulmonary connections: J Thorac Cardiovasc Surg, 1996; 111 (3): 502-13.

de Leval, M. R., P. Kilner, M. Gewillig, and C. Bull, Total cavopulmonary connection: a logical alternative to atriopulmonary connection for complex Fontan operations. Experimental studies and early clinical experience: J Thorac Cardiovasc Surg, 1988; 96 (5): 682-95.

de Zélicourt, D.A., Pekkan, K., Wills, E., Kanter, K., Forbess, J., Sharma, S., Fogel, M., and A. P. Yoganathan, In Vitro Flow Analysis of a Patient Specific Intra-Atrial TCPC: Ann Thorac Surg , 2005;79(6):2094-102.

de Zelicourt DA, Pekkan K, Parks J, Kanter K, Fogel M, Yoganathan AP. Flow study of an extracardiac connection with persistent left superior vena cava. J Thorac Cardiovasc Surg. 2006;131(4):785-91.

DeGroff, C. G., J. D. Carlton, C. E. Weinberg, M. C. Ellison, R. Shandas, and L. Valdes-Cruz, Effect of vessel size on the flow efficiency of the total cavopulmonary connection: in vitro studies: Pediatr Cardiol, 2002; 23 (2): 171-7.

Dobell, A. R., G. A. Trusler, J. F. Smallhorn, and W. G. Williams, Atrial thrombi after the Fontan operation: Ann Thorac Surg, 1986; 42 (6): 664-7.

Driscoll, D. J., K. P. Offord, R. H. Feldt, H. V. Schaff, F. J. Puga, and G. K. Danielson, Five- to fifteen-year follow-up after Fontan operation: Circulation, 1992; 85 (2): 469-96.

Ensley, A. E., P. Lynch, G. P. Chatzimavroudis, C. Lucas, S. Sharma, and A. P. Yoganathan, Toward designing the optimal total cavopulmonary connection: an in vitro study: Ann Thorac Surg, 1999; 68 (4): 1384-90.

Fogel, M. A., P. M. Weinberg, A. J. Chin, K. E. Fellows, and E. A. Hoffman, Late ventricular geometry and performance changes of functional single ventricle throughout staged Fontan reconstruction assessed by magnetic resonance imaging: J Am Coll Cardiol, 1996; 28 (1): 212-21.

Fogel, M. A., P. M. Weinberg, J. Rychik, A. Hubbard, M. Jacobs, T. L. Spray, and J. Haselgrove, Caval contribution to flow in the branch pulmonary arteries of Fontan patients with a novel application of magnetic resonance presaturation pulse: Circulation, 1999; 99 (9): 1215-21.

Fontan, F., and E. Baudet, Surgical repair of tricuspid atresia: Thorax, 1971; 26: 240-248.

Fontan, F., J. W. Kirklin, G. Fernandez, F. Costa, D. C. Naftel, F. Tritto, and E. H. Blackstone, Outcome after a "perfect" Fontan operation: Circulation, 1990; 81 (5): 1520-36.

Frakes, D. H., C. P. Conrad, T. M. Healy, J. W. Monaco, M. Fogel, S. Sharma, M. J. Smith, and A. P. Yoganathan, Application of an adaptive control grid interpolation technique to morphological vascular reconstruction: IEEE Trans Biomed Eng, 2003; 50 (2): 197-206.

Frakes, D. H., Pekkan, K., Smith, M.J.T., Yoganathan, A. Three-Dimensional Velocity Field Reconstruction. J. of Biomechanical Eng. 2004; 126:727-735.

Gerdes, A., J. Kunze, G. Pfister, and H. H. Sievers, Addition of a small curvature reduces power losses across total cavopulmonary connections: Ann Thorac Surg, 1999; 67 (6): 1760-4.

Glenn, W. W. L., Circulatory bypass of the right side of the heart: N. Engl. J. Med., 1958; 259: 117-120.

Grigioni, M., A. Amodeo, C. Daniele, G. D'Avenio, R. Formigari, and R. M. Di Donato, Particle image velocimetry analysis of the flow field in the total cavopulmonary connection: Artif Organs, 2000; 24 (12): 946-52.

Guadagni, G., E. L. Bove, F. Migliavacca, and G. Dubini, Effects of pulmonary afterload on the hemodynamics after the hemi-Fontan procedure: Med Eng Phys, 2001; 23 (5): 293-8.

Haas, G. S., H. Hess, M. Black, J. Onnasch, F. W. Mohr, and J. A. van Son, Extracardiac conduit fontan procedure: early and intermediate results: Eur J Cardiothorac Surg, 2000; 17 (6): 648-54.

Healy, T. M., C. Lucas, and A. P. Yoganathan, Noninvasive fluid dynamic power loss assessments for total cavopulmonary connections using the viscous dissipation function: a feasibility study: J Biomech Eng, 2001; 123 (4): 317-24.

Hong L. 3D virtual colonoscopy. Proceedings IEEE Biomedical Visualization, 1995, pp. 26–32.

Hosein RB, Clarke AJ, McGuirk SP, Griselli M, Stumper O, De Giovanni JV, Barron DJ, Brawn WJ. Factors influencing early and late outcome following the Fontan procedure in the current era-The 'Two Commandments'?. Eur J Cardiothorac Surg. 2007;31:344-52.

Hsia, T. Y., F. Migliavacca, S. Pittaccio, A. Radaelli, G. Dubini, G. Pennati, and M. de Leval, Computational fluid dynamic study of flow optimization in realistic models of the total cavopulmonary connections: J Surg Res, 2004; 116 (2): 305-13.

Justino, H., L. N. Benson, and R. M. Freedom, Development of unilateral pulmonary arteriovenous malformations due to unequal distribution of hepatic venous flow: Circulation, 2001; 103 (8): E39-40.

Kaufman A, Sobierajski. L, Avila R, and He T. Navigation and animation in a volume visualization system. Models and Techniques in Computer Animation, Berlin, 1993, pp. 64–74.

Kiesler K, Gugatschka M, Sorantin E, Friedrich G. Laryngo-tracheal profile: a new method for assessing laryngo-tracheal stenoses. Eur Arch Otorhinolaryngol. 2007;264(3):251-6.

Khairy P, Poirier N, Mercier LA. Univentricular heart. Circulation. 2007;115(6):800-812.

Khunatorn, Y., R. Shandas, C. DeGroff, and S. Mahalingam, Comparison of in vitro velocity measurements in a scaled total cavopulmonary connection with computational predictions: Ann Biomed Eng, 2003; 31 (7): 810-22.

Kong, T.Y., Rosenfeld, A. Digital topology: Introduction and survey. Comput. Vision Graphics Image Process. 1989;48: 357–393.

Kyger ER III, Reul GJ Jr, Sandiford FM, Wukasch DC, Hallman GL, Cooley DA. Surgical palliation of tricuspid atresia, Circulation. 1975;52(4):685-90.

Kreutzer, G., E. Galindez, H. Bono, C. De Palma, and J. P. Laura, An operation for the correction of tricuspid atresia: J Thorac Cardiovasc Surg, 1973; 66 (4): 613-21.

Lardo, A. C., P. J. del Nido, S. A. Webber, I. Friehs, and E. G. Cape, Hemodynamic effect of progressive right atrial dilatation in atriopulmonary connections: J Thorac Cardiovasc Surg, 1997; 114 (1): 2-8.

Lardo, A. C., S. A. Webber, I. Friehs, P. J. del Nido, and E. G. Cape, Fluid dynamic comparison of intra-atrial and extracardiac total cavopulmonary connections: J Thorac Cardiovasc Surg, 1999; 117 (4): 697-704.

Laschinger JC, Ringel RE, Brenner JI, McLaughlin JS. The Extracardiac Total Cavopulmonary Connection for Definitive Conversion to the Fontan Circulation: Summary of Early Exp rience and Results. J Cardiac Surg, 1993;8:524-533,

Laschinger JC, Redmond JM, Cameron DE, Kan JS, Ringel RE. Intermediate Results of the Extracardiac Fontan Procedure. Annals of Thoracic Surgery, 1996;62:1261-1267,

Lorensen W. E, Jolesz. F.A, and Kikinis. R. The exploration of cross sectional data with a virtual endoscope. Interactive Technology and the New Medical Paradigm for Health Care, Editors.: K. Morgan, R.M. Satava, H.B. Sieburg, R. Mattheus, J.P. Christensen, IOS Press, 1995; pp.221-230.

Mair, D. D., F. J. Puga, and G. K. Danielson, Late functional status of survivors of the Fontan procedure performed during the 1970s: Circulation, 1992; 86 (5 Suppl): II106-9.

Marcelletti C, Corno A, Giannico S, Marino B. Inferior Vena-cava-pulmonary Artery Extracardiac Conduit. J Thorac Cardiovasc Surg, 1990;100:228-232,.

Marcelletti, C. F., F. L. Hanley, C. Mavroudis, D. B. McElhinney, R. F. Abella, S. M. Marianeschi, F. Seddio, V. M. Reddy, E. Petrossian, T. de la Torre, L. Colagrande, C. L. Backer, A. Cipriani, F. S. Iorio, and F. Fontan, Revision of previous Fontan connections to total extracardiac cavopulmonary anastomosis: A multicenter experience: J Thorac Cardiovasc Surg, 2000; 119 (2): 340-6.

Mavroudis, C., V. R. Zales, C. L. Backer, A. J. Muster, and L. A. Latson, Fenestrated Fontan with delayed catheter closure. Effects of volume loading and baffle fenestration on cardiac index and oxygen delivery: Circulation, 1992; 86 (5 Suppl): II85-92.

206

Migliavacca, F., G. Dubini, E. L. Bove, and M. R. de Leval, Computational fluid dynamics simulations in realistic 3-D geometries of the total cavopulmonary anastomosis: the influence of the inferior caval anastomosis: J Biomech Eng, 2003; 125 (6): 805-13.

Migliavacca, F., M. R. de Leval, G. Dubini, R. Pietrabissa, and R. Fumero, Computational fluid dynamic simulations of cavopulmonary connections with an extracardiac lateral conduit: Med Eng Phys, 1999; 21 (3): 187-93.

Morgan VL, Graham TP Jr, Roselli RJ, Lorenz CH. Alterations in pulmonary artery flow patterns and shear stress determined with three-dimensional phase-contrast magnetic resonance imaging in Fontan patients. J Thorac Cardiovasc Surg. 1998 116(2):294-304.

Morgenthaler, D.G., 1981. Three-dimensional simple points: Serial erosion, parallel thinning and skeletonization. Tech. Rept. TR-1005,. Computer Vision Laboratory, Computer Science Center, University of Maryland, College Park, MD.

Norwood, W. I., and M. L. Jacobs, Fontan's procedure in two stages: Am J Surg, 1993; 166 (5): 548-51.

Ordovas KG, Tan C, Reddy GP, Weber OM, Lu Y, Higgins CB. Disparity between ratios of diameters and blood flows in central pulmonary arteries in postoperative congenital heart disease using MRI. J Magn Reson Imaging. 2007;25(4):721-6.

Paik DS, Beaulieu CF, Jeffrey RB, Rubin GD, Napel S. Automated flight path planning for virtual endoscopy. Med Phys. 1998;25(5):629-37.

Palagyi K, Kuba A. 3D 6-subiteration thinning algorithm for extracting medial lines. Pattern Recognition Letters. 1998; 19: 613–627

Pearl, J. M., H. Laks, D. G. Stein, D. C. Drinkwater, B. L. George, and R. G. Williams, Total cavopulmonary anastomosis versus conventional modified Fontan procedure: Ann Thorac Surg, 1991; 52 (2): 189-96.

Pekkan, K., D. de Zélicourt, L. Ge, F. Sotiropoulos, D. H. Frakes, M. A. Fogel, and A. P. Yoganathan, Physics-driven CFD modeling of complex anatomical cardiovascular flows-a TCPC case study: Ann. Biomed. Eng., 2004; 33(3):284-300.

Pekkan K, Kitajima HD, de Zelicourt D, Forbess JM, Parks WJ, Fogel MA, Sharma S, Kanter KR, Frakes D, Yoganathan AP. Total cavopulmonary connection flow with functional left pulmonary artery stenosis: angioplasty and fenestration in vitro. Circulation. 2005;112:3264-3271.

Petrossian, E., V. M. Reddy, D. B. McElhinney, G. P. Akkersdijk, P. Moore, A. J. Parry, L. D. Thompson, and F. L. Hanley, Early results of the extracardiac conduit Fontan operation: J Thorac Cardiovasc Surg, 1999; 117 (4): 688-96.

Pike, N. A., L. A. Vricella, J. A. Feinstein, M. D. Black, and B. A. Reitz, Regression of severe pulmonary arteriovenous malformations after Fontan revision and "hepatic factor" rerouting: Ann Thorac Surg, 2004; 78 (2): 697-9.

Podzolkov, V. P., S. B. Zaets, M. R. Chiaureli, B. G. Alekyan, L. M. Zotova, and I. G. Chernikh, Comparative assessment of Fontan operation in modifications of atriopulmonary and total cavopulmonary anastomoses: Eur J Cardiothorac Surg, 1997; 11 (3): 458-65.

Potts, W. J., S. Smith, and S. Gibson, Anastomosis of the aorta to a pulmonary artery: J. Amer. Med. Assoc., 1946; 132: 627-631.

Quinones, J. A., S. Y. Deleon, T. J. Bell, F. Cetta, S. M. Moffa, J. E. Freeman, D. A. Vitullo, and E. A. Fisher, Fenestrated fontan procedure: evolution of technique and occurrence of paradoxical embolism: Pediatr Cardiol, 1997; 18 (3): 218-21.

Rodbard S, Wagner D. Bypassing the Right Ventricle. Proc Soc Exp Biol Med, 1949; 69.

Rosano, A., L. D. Botto, B. Botting, and P. Mastroiacovo, Infant mortality and congenital anomalies from 1950 to 1994: an international perspective: J Epidemiol Community Health, 2000; 54 (9): 660-6.

Rosenfeld, A. A characterization of parallel thinning algorithms. Inform. and Control . 1975;29: 286–291.

Ryu, K., T. M. Healy, A. E. Ensley, S. Sharma, C. Lucas, and A. P. Yoganathan, Importance of accurate geometry in the study of the total cavopulmonary connection: computational simulations and in vitro experiments: Ann Biomed Eng, 2001; 29 (10): 844-53.

Salim, M. A., T. G. DiSessa, K. L. Arheart, and B. S. Alpert, Contribution of superior vena caval flow to total cardiac output in children. A Doppler echocardiographic study: Circulation, 1995; 92 (7): 1860-5.

Sharma, S., A. E. Ensley, K. Hopkins, G. P. Chatzimavroudis, T. M. Healy, V. K. Tam, K. R. Kanter, and A. P. Yoganathan, In vivo flow dynamics of the total cavopulmonary connection from three-dimensional multislice magnetic resonance imaging: Ann Thorac Surg, 2001; 71 (3): 889-98.

Sharma, S., S. Goudy, P. Walker, S. Panchal, A. Ensley, K. Kanter, V. Tam, D. Fyfe, and A. Yoganathan, In vitro flow experiments for determination of optimal geometry of total cavopulmonary connection for surgical repair of children with functional single ventricle: J Am Coll Cardiol, 1996; 27 (5): 1264-9.

Shemin, R. J., W. H. Merrill, J. S. Pfeifer, D. M. Conkle, and A. G. Morrow, Evaluation of right atrial-pulmonary artery conduits for tricuspid atresia. Experimental study: J Thorac Cardiovasc Surg, 1979; 77 (5): 685-90.

Shiota, T., R. Lewandowski, J. E. Piel, L. S. Smith, C. Lancee, K. Djoa, N. Bom, A. Cobanoglu, M. J. Rice, and D. J. Sahn, Micromultiplane transesophageal echocardiographic probe for intraoperative study of congenital heart disease repair in neonates, infants, children, and adults: Am J Cardiol, 1999; 83 (2): 292-5, A7.

Soerensen DD, Pekkan K, de Zelicourt D, Sharma S, Kanter K, Fogel M, Yoganathan AP. Introduction of a new optimized total cavopulmonary connection. Ann Thorac Surg. 2007;83(6):2182-90.

Srivastava, D., T. Preminger, J. E. Lock, V. Mandell, J. F. Keane, J. E. Mayer, Jr., H. Kozakewich, and P. J. Spevak, Hepatic venous blood and the development of pulmonary arteriovenous malformations in congenital heart disease: Circulation, 1995; 92 (5): 1217-22.

Steele BN, Draney MT, Ku JP and Taylor CA. Internet-Based System for Simulation-Based Medical Planning for Cardiovascular Disease. IEEE transactions on information technology in biomedicine, 2003;7(2):123-9.

Sundareswaran KS, Kanter KR, Kitajima HD, Krishnankutty R, Sabatier JF, Parks WJ, Sharma S, Yoganathan AP, Fogel M. Impaired power output and cardiac index with hypoplastic left heart syndrome: a magnetic resonance imaging study. Ann Thorac Surg. 2006;82:1267-75

Tam, V. K., B. E. Miller, and K. Murphy, Modified Fontan without use of cardiopulmonary bypass: Ann Thorac Surg, 1999; 68 (5): 1698-703; discussion 1703-4.

Tanoue, Y., A. Sese, Y. Ueno, K. Joh, and T. Hijii, Bidirectional Glenn procedure improves the mechanical efficiency of a total cavopulmonary connection in high-risk fontan candidates: Circulation, 2001; 103 (17): 2176-80.

Vining DJ. Virtual colonoscopy. Semin Ultrasound CT MR. 1999 ;20(1):56-60.

Walker PG, Oweis GF and Watterson KG. Distribution of hepatic venous blood in the total cavo pulmonary connection: an in vitro study into the effects of connection geometry. J Biomech Eng. 2001;123(6):558-64.

Wang KC, Dutton RW and Taylor CA. Improving geometric model construction for blood flow modeling. IEEE Eng Med Biol Mag. 1999;18(6):33-9.

Yang Y, Zhu L, Tannenbaum A, Giddens D. Harmonic skeleton guided evaluation of stenoses in human coronary arteries. Medical Image computing and computer assisted intervention, 2005;8(Pt 1):490-7.

Yushkevich PA, Zhang H, and Gee JC. Continuous Medial Representation for Anatomical Structures. IEEE Trans on medical imaging, 2006;25(12):1547-64.

Zhu L, Haker S, and Tannenbaum A. Flattening Maps for the Visualization of Multibranched Vessels. IEEE Trans medical imaging, 2005; 24 (2): 191-198.